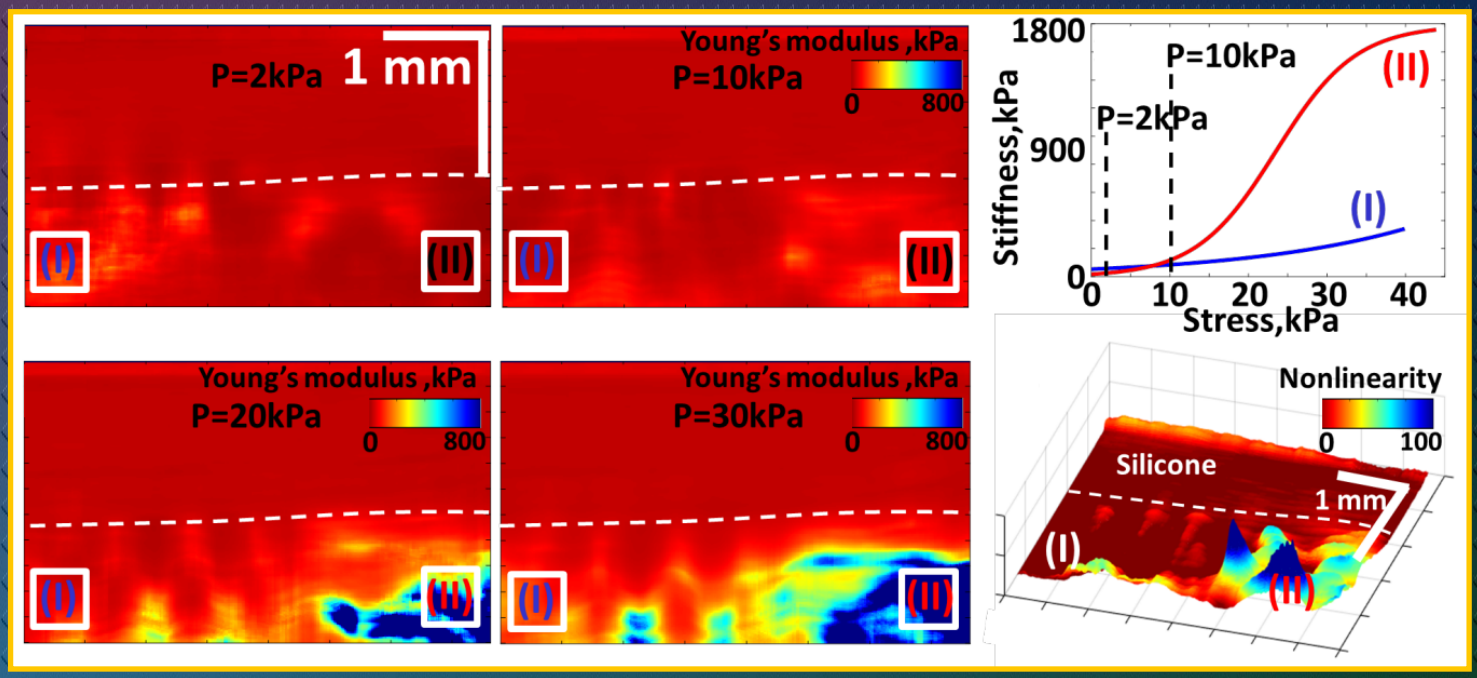
Volume 8, Issue 3, 2022

Journal of Biomedical Photonics & Engineering



Editor-in-Chief:
Valery V. Tuchin

© 2022 J-BPE

Journal of Biomedical Photonics & Engineering

by Samara National Research University

Volume 8, Issue 3 (September 2022)

Editor-In-Chief

Valery V. Tuchin - Saratov National Research State University, Russian Federation;
Institute of Precision Mechanics and Control RAS, Russian Federation; a corr.-member of RAS

Deputy Editor-In-Chief

Valery P. Zakharov - Samara National Research University, Russian Federation

Postal address:
39B Lukacheva st., room #301
Samara 443086, Russian Federation

Used Figure from this issue on the Cover

Alexander A. Sovetsky et al., *Mapping Large Strains in Phase-Sensitive OCT: Key Role of Supra-Pixel Displacement Tracking in Incremental Strain Evaluation*, 030304, Fig. 9.

© 2022 J-BPE

Contents

Articles

Method for Designing and Characterizing Phototherapy Shields 030301
Tyler W. Iorizzo, Javed Mannan, and Anna N. Yaroslavsky

An Analytical Solution of the Hyperbolic Bioheat Model of the Cornea Subjected to Laser Irradiation 030302
Ram Autar and Anuj Kumar

Study of the Diffusion of Tetracycline in the Dentin of the Human Tooth Ex Vivo 030303
Alexey A. Selifonov, Tatyana Yu. Rusanova, Ekaterina I. Selifonova, and Valery V. Tuchin

Mapping Large Strains in Phase-Sensitive OCT: Key Role of Supra-Pixel Displacement Tracking in Incremental Strain Evaluation 030304
Alexander A. Sovetsky, Alexander L. Matveyev, Lev A. Matveev, Grigory V. Gelikonov, and Vladimir Y. Zaitsev

Novel UV-Releaser of Arachidonic Acid Based on Nitrophenyl-type Photoremovable Protecting Group 030305
Darya N. Litunenko, Tatyana Yu. Karogodina, Alexey Yu. Vorob'ev, and Alexander E. Moskalensky

Justification of the Photoplethysmography Sensor Configuration by Monte Carlo Modeling of the Pulse Waveform 030306
Denis G. Lapitan, Andrey P. Tarasov, and Dmitry A. Rogatkin

Examining the Validity of Input Lung CT Images Submitted to the AI-Based Computerized Diagnosis 030307
Aleksandra A. Kosareva, Dzmitry A. Paulenka, Eduard V. Snezhko, Ivan A. Bratchenko, and Vassili A. Kovalev

 © 2022 J-BPE

Method for Designing and Characterizing Phototherapy Shields

Tyler W. Iorizzo[1], Javed Mannan[2], and Anna N. Yaroslavsky[1*]
[1] Advanced Biophotonics Laboratory, University of Massachusetts Lowell, MA, USA
[2] University of Massachusetts Medical School, Worcester, MA, USA

*** e-mail:** anna_yaroslavsky@uml.edu

Abstract. Optimal shield properties and design are of vital importance for preventing adverse effects of light-based clinical procedures. The goal of this study was to select the most appropriate materials for a two-layer phototherapy shield. Four biocompatible fabrics, to be utilized as the layer contacting patients' skin, and two reflective materials, to be utilized as the layer facing the light source, were investigated. The optical properties of the four biocompatible fabrics and transmittance of the two reflective materials were determined in the 400–500 nm range. Absorption coefficient, scattering coefficient, and anisotropy factors of biocompatible fabrics were determined using integrating sphere spectrophotometry and an inverse Monte Carlo method. Fabric and reflective materials that exhibited highest attenuation of the blue light were selected to assemble a two-layer composite prototype. Prototypes were exposed to blue light emitted from a clinical source to ensure negligible temperature increase under clinically relevant exposure conditions. A protype blue-light phototherapy shield was made from two test materials, both of which provide sufficient light attenuation to provide patient protection. The testing method employed in this study may prove valuable for designing protective gear for a range of clinical procedures. © 2022 Journal of Biomedical Photonics & Engineering.

Keywords: phototherapy; integrating sphere spectrophotometry; phototherapy shielding.

Paper #3472 received 24 Jan 2022; revised manuscript received 09 May 2022; accepted for publication 22 Jun 2022; published online 5 Jul 2022. doi: 10.18287/JBPE22.08.030301.

1 Introduction

Side effects from various phototherapy procedures have been well documented. Blue light phototherapy for treating jaundice in neonates has been shown to cause retinal damage as well as damage to red blood cells, which may lead to bronchopulmonary dysplasia, retinopathy, and necrotizing enterocolitis [1]. Blue light phototherapy has also been associated with the formation of patent ductus arteriosus [1] and may increase the chance of melanocytic nevus development [2]. Exposure to blue light can lead to free radical generation in skin which can cause further tissue damage [3–6]. UV phototherapy for psoriasis, vitiligo, and polymorphic light eruption may lead to carcinogenesis, cataracts, lentigines, photoaging [7]. Keratitis with facial erythema has also been reported forming after UV treatments [8]. Atrophy of the superonasal iris, iris transillumination defects, pigmentation on the anterior capsule, anisocoria, and dyscoria have all been reported developing in patients receiving Intense Pulsed Light (IPL) therapy [9, 10]. Therefore, it is important to use phototherapy shields to reduce side effects from light treatments [1, 11, 12]. Shielding must protect photosensitive tissues by blocking the treatment light, while allowing the efficacious dose to be delivered over unshielded areas of the patient's body.

In this study, materials for a two-layered, blue light phototherapy shield were tested and compared. Reflective foils were considered for the top layer, facing the light source, while biocompatible fabrics were examined for the bottom layer, facing the patient.

Biocompatible fabrics were evaluated using integrating sphere spectrophotometry. Reflective materials were characterized by transmittance measurements

2 Materials and Methods

2.1 Biocompatible Fabrics

The optical properties of Spunbond Polypropylene 100 gsm, K160082 60 gsm, K170081 35 gsm, and K170087 50 gsm biocompatible fabrics (Uniquetex Engineered Nonwovens, Grover, NC, USA) were investigated using integrating sphere spectrophotometry. Seven samples were prepared for each material type. Lateral dimensions of the samples were at most 42 × 50 mm. Sample thicknesses ranged from 0.172 ± 0.004 mm to 0.306 ± 0.002 mm. Sample thickness was measured using a digital micrometer (293–340 Digital Micrometer, Mitutoyo, Japan).

2.2 Reflective Foils

Reflective foils DM146 and DE 050 (Dunmore, Bristol, PA, USA) were compared using transmittance spectrophotometry. Seven samples with lateral dimensions 45 × 12 mm were prepared for each foil. Average thicknesses of DM146 and DE 050 samples were 0.021 ± 0.001 mm and 0.082 ± 0.001 mm, respectively. Thicknesses were measured using a micrometer (293–340 Digital Micrometer, Mitutoyo, Japan).

2.3 Integrating Sphere Spectrophotometry

A single integrating sphere system that was used to measure the total transmittance, diffuse transmittance, and diffuse reflectance of the biocompatible fabrics in the spectral range of 400–500 nm is shown in Fig. 1. Samples were placed at the entrance and exit ports of the integrating sphere (4P-GPS-033-SL, Labsphere, North Sutton, NH, USA) for transmittance and reflectance measurements, respectively. Light from a halogen lamp (HL-2000, 360–2000 nm, Ocean Optics, Dunedin, FL, USA) was focused onto the samples. The focal spot had a diameter of 3 mm. Sample and exit ports of the integrating sphere had a diameter of 14 mm and 25.4 mm, respectively. Transmittance through air, and reflectance from Spectralon (> 99% reflectance) were used as a reference. The exit port of the integrating sphere was opened during diffuse transmittance measurements to allow collimated light to escape. Collimated transmittance was calculated by subtracting diffuse transmittance from total transmittance at each wavelength investigated. An HR2000 spectrometer (Ocean Optics, Dunedin, FL, USA) was coupled to the auxiliary port of the integrating sphere via an optical fiber (P600-2-SR, Ocean Optics, Dunedin, FL, USA) to measure the spectral response in the 400–500 nm range.

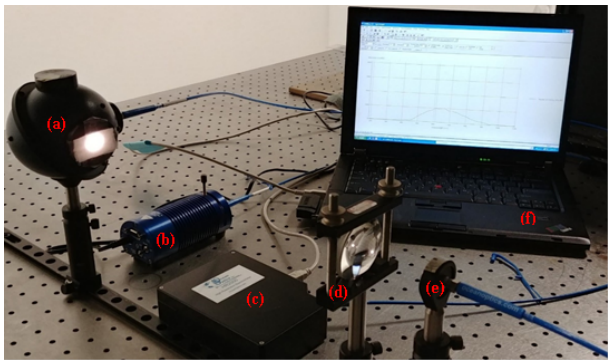


Fig. 1 Integrating sphere set-up. Halogen lamp light (b) was coupled into an optical fiber (e) and focused onto the sample by a lens (d). Light transmitted and reflected from the sample was collected by the integrating sphere (a) and detected by a grating spectrometer (c). Data acquisition was controlled by external PC (f).

2.4 Inverse Monte Carlo Technique

Absorption coefficients, scattering coefficients, and anisotropy factors of the biocompatible fabric materials were calculated from measured quantities under an assumption of Henyey-Greenstein scattering phase function [13] using an inverse hybrid Monte Carlo algorithm [14]. This method employed a forward Monte Carlo technique that accounted for the exact geometrical and optical properties of the integrating sphere walls and light losses at the edges of the samples. The forward Monte Carlo method was integrated into a Quasi-Newton inverse algorithm [15], optimized to reduce the number of forward Monte Carlo calls.

2.5 Transmittance Measurements

Transmittance through reflective materials in the spectral range of 400–500 nm was measured using a spectrophotometer (Lambda 1050, PerkinElmer Inc., Waltham, MA, USA). The spectrophotometer slit width was set to 5 nm, and the wavelength step size was set to 2 nm. The illumination beam had a diameter of 4.5 mm. Transmittance through air was used as a reference. Transmittance of each reflective sample were measured twice, then averaged.

2.6 Temperature Monitoring

After determining the optical properties and selecting appropriate biocompatible and reflective materials, a two-layer shield prototype was assembled. The temperature of the composite shield exposed to 450–470 nm light was monitored over a 48-hour time interval. The experimental arrangement used for monitoring the temperature of the shield is shown in Fig. 2. A Natus neoBLUE mini LED phototherapy lamp (Natus Medical Incorporated, San Carlos, CA, USA) was used as a light source. Shield samples were suspended above the optical table to provide thermal isolation. The lamp was placed 30.5 cm above the samples. At this height, samples were exposed to a peak central intensity of 30 $\mu W/cm^2/nm$. A

temperature sensor was attached to the biocompatible surface of the composite shield, where the shield would be in contact with patient skin. The sensor was connected to an external temperature monitor (CT16A2080-948, Minco, Minneapolis, MN, USA). The geometry and duration of temperature monitoring experiments were exactly as those during the clinical phototherapy procedure.

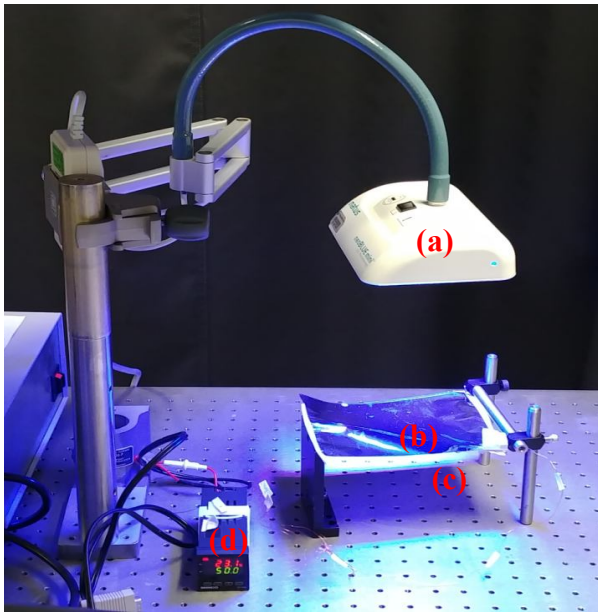


Fig. 2 Experimental setup used for shield material temperature monitoring. Light from the phototherapy lamp (a) was incident onto the shield material (b). A temperature sensor (c) underneath the sample allowed the temperature monitor (d) to measure the temperature of the sample.

3 Results

3.1 Optical Properties of Biocompatible Fabric Materials

Absorption coefficients, scattering coefficients, and anisotropy factors of biocompatible fabric materials, determined in the spectral range of 400–500 nm, are shown in Fig. 3. Absorption coefficients are presented in Fig. 3(a). Absorption of Spunbond Polypropylene 100 gsm, K170081 35 gsm, and K170087 50 gsm monotonously increase with increasing wavelength. The absorption spectrum of K160082 60 gsm decreases with increasing wavelength between 400–420 nm, then increases with wavelength in the 420–500 nm range. K160082 60 gsm exhibited the greatest absorption out of all biocompatible fabrics investigated, ranging between 0.4 and 0.1 mm^{-1} over the entire spectral range. The absorption of all other fabrics was less than 0.09 mm^{-1}.

Scattering coefficients are shown in Fig. 3(b). Scattering of all fabrics decreased with increasing wavelength. K160082 60 gsm has the greatest scattering over the entire spectral region, with coefficients greater than 7.3 mm^{-1}. All other fabrics have scattering less than 4.6 mm^{-1}.

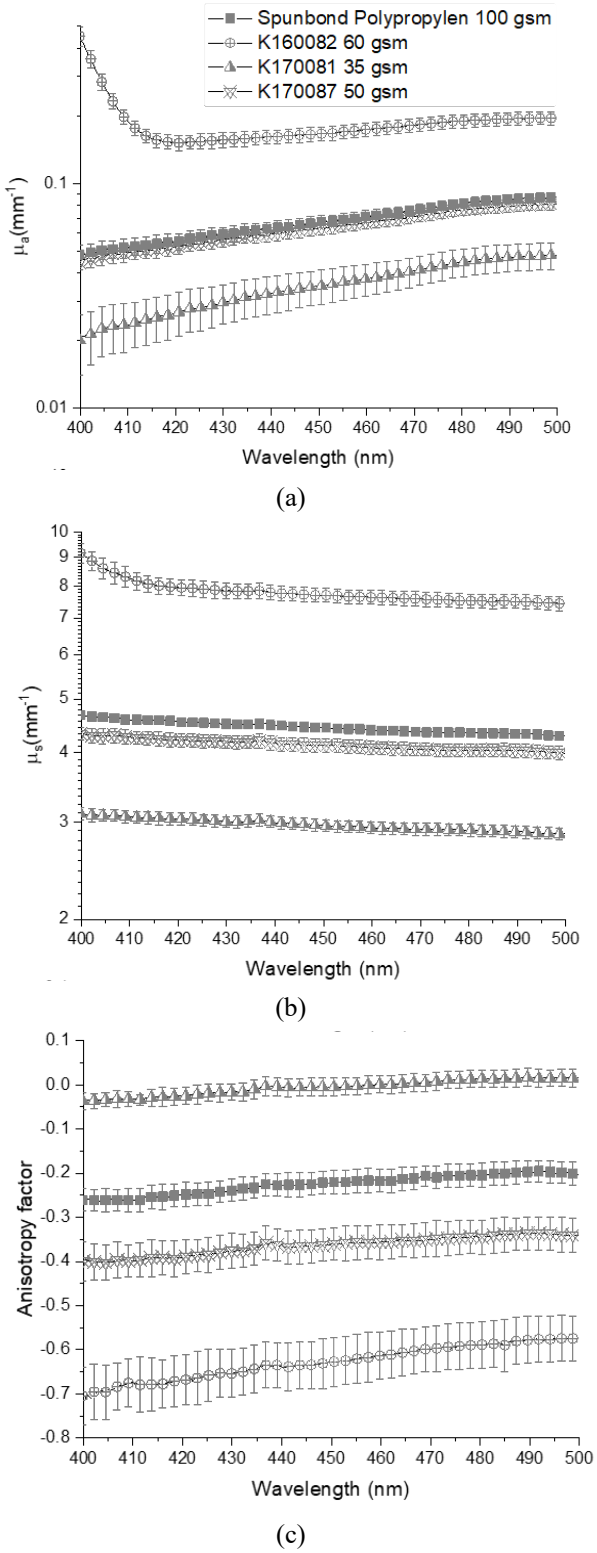


Fig. 3 Absorption coefficients (a), scattering coefficients (b), and anisotropy factors (c) of biocompatible fabric materials between 400–500 nm. Squares – Spunbond Polypropylene 100 gsm. Circles with a Cross – K160082 60 gsm. Half-filled Upright Triangle – K170081 35 gsm. Upside-down Triangle with an X – K170087 50 gsm. Bars – standard deviations.

Anisotropy of Spunbond Polypropylene 100 gsm, K160082 60 gsm, and K170087 50 gsm are negative over the entire spectral range, whereas K170081 35 gsm has positive values between 458-500 nm. K160082 60 gsm has the greatest negative anisotropy factors ranging between –0.7 and –0.65 over the investigated spectral region.

Of the four biocompatible fabrics investigated, K160082 60 gsm has the greatest absorption and scattering in the 400–500 nm spectral range. The results show that scattering is the dominant attenuation process. Calculated absorption coefficients are an order of magnitude lower than the scattering coefficients. Due to the low absorption, a low temperature increase in the fabric during treatment can be expected. Moreover, K160082 60 gsm has the largest negative anisotropy factors out of the four fabrics tested. Thus, light has the highest probability of exhibiting backscattering when incident on K160082 60 gsm. Due to predominant backscattering properties of the K160082 60 gsm, more light will propagate towards the light source as compared to towards the patient. These results indicate that out of the four biocompatible fabrics tested, K160082 60 gsm is the most appropriate material for the bottom layer of the blue light phototherapy shield.

3.2 Transmittance Measurements of Reflective Materials

Transmittance of the two reflective materials were below 0.1% over the entire 400–500 nm range. Average transmittance measurements ranged between 0.039–0.071%, and 0.024–0.045% for Dm146 and DE 050, respectively. Lower transmittance points to higher attenuation of 400–500 nm light by DE 050 as compared to Dm146. Therefore, DE 050 was selected for the top layer of the blue light phototherapy shield.

3.3 Temperature Monitoring of Selected Shielding Materials

Based on the results of the optical experiments, composite shields were prepared with DE 050 as the top layer facing the light and K160082 60 gsm as the bottom layer facing patient's skin. Recorded shield temperatures ranged between 16.3 °C and 23.3 °C when exposed to blue treatment light. Temperatures of the shields followed the same temperature trends as room temperature. Thus, the phototherapy lamp did not have a significant effect on the shield temperature.

4 Discussion

Many studies have been made to characterize and compare shielding materials. The most common approach is to measure optical transmission of the shields in the spectral range of interest. Chin et al. [16] had investigated the transmission of 250–800 nm light through 12 potential eye shields using a spectrophotometer system. Robinson et al. [17] measured the transmission of 300–750 nm light through three eye shield materials while placed in phototherapy units, to account for reflection from the therapy unit walls. Otman et al. [18] determined the UV transmission of commercial sunglasses and contact lenses that were allowed to be worn by patients during treatments using a spectrophotometry system. Abdulla et al. [19] measured UV transmission through potential shielding materials for genital protection from UVA, broad band UVB, and narrow band UVB illumination. In this paper we explored a more general approach that can be utilized not only for testing and comparing prospective shields, but also to inform their selection, optimization, and design. Since attenuation of light is governed by the optical properties of the medium, we started with determining the absorption coefficients, scattering coefficients, and anisotropy factors of the materials from diffuse reflectance and transmittance measurements using integrating sphere spectrophotometry [20–23] and inverse Monte Carlo technique. This approach enables comparison of the shield attenuation properties irrespectively of the material thickness and allows for its optimization without exhaustive repetitive transmission measurements.

Each layer of the designed shield provides sufficient protection from therapeutic blue light. While the reflective top layer exhibits low transmittance in this spectral range, it may increase in temperature when illuminated and may have sharp edges which may injure the patient. The biocompatible fabric bottom layer protects the patient from any harm caused by the foil and allows the shield to conform to the patient's body to provide a secure fit. Total attenuation per mm thickness of the fabric can be found from the characterized optical properties. Fabric thickness can then be optimized to provide adequate protection from the treatment light in case the top layer fails. The top layer of this shield will reflect treatment light away from the patient, which may be harmful for other individuals in the treatment room [3–6]. Reflection can be reduced by adding another fabric layer on top of the reflective material, thus resulting in a three-layered shield.

5 Conclusion

Selecting shielding materials based on its optical and thermal properties enables straightforward optimization of shield design and ensures proper patient protection during phototherapy. While this study focused on shielding for blue light phototherapy, this method for characterizing shield materials can be utilized for any desired wavelength range and phototherapy procedure.

Disclosures

The authors have stated explicitly that there are no conflicts of interest in connection with this article.

Acknowledgments

We would like to thank Cheryl Gomes from the Fabric Discovery Center at the University of Massachusetts

Lowell for providing the test materials for this study and Androniki Mitrou from the Advanced Biophotonics Laboratory for assistance with temperature measurements. Funding provided by the Office of Technology Commercialization is greatly appreciated.

References

1. L. A. Stokowski, "Fundamentals of Phototherapy for Neonatal Jaundice," Advances in Neonatal Care 11(5S), S10–S21 (2013).
2. Z. Csoma, E. Tóth-Molnár, K. Balogh, H. Polyánka, H. Orvos, H. Ócsai, L. Kemény, M. Széll, and J. Oláh, "Neonatal Blue Light Phototehrapy and Melanocytic Nevi: A Twin Study," Pediatrics 128(4), e856–e864 (2011).
3. B. F. Godley, F. Shamsi, F.-Q. Liang, S. G. Jarrett, S. Davies, and M. Boulton, "Blue Light Induces Mitochondrial DNA Damage and Free Radical Production in Epithelial Cells," Journal of Biological Chemistry 280(22), 21061–21066 (2005).
4. S. Vandersee, M. Beyer, J. Lademann, and M. E. Darvin, "Blue-Violet Light Irradiation Dose Dependently Decreases Carotenoids in Human Skin, Which Indicates the Generation of Free Radicals," Oxidative Medicine and Cellular Longevity 2015, 579675 (2015).
5. Y. Nakashima, S. Ohta, and A. M.Wolf, "Blue light-induced oxidative stress in live skin," Free Radical Biology and Medicine 108, 300–310 (2017).
6. J. G. Coats, B. Maktabi, M. S. Abou-Dahech, and G. Baki, "Blue Light Protection, Part 1 – Effects of blue light on the skin," Journal of Cosmetic Dermatology 20(3), 714–717 (2021).
7. S. A. Holme, A. V. Anstey, "Phototherapy and PUVA photochemotherapy in children," Photodermatology Photoimmunology and Photomedicine 20(2), 69–75 (2004).
8. P. Komericki, P. Fellner, Y. El-Shabrawi, and N. Ardjomand, "Keratopathy after ultraviolet B phototherapy," Wiener Klinische Wochenschrift 117(7–8), 300–302 (2005).
9. G. Javey, S. G. Schwartz, and T. A. Albini, "Ocular Complication of Intense Pulsed Light Therapy: Iris Photoablation," Dermatologic Surgery 36(9), 1446–1468 (2010).
10. M. Crabb, W. O. Chan, D. Taranath, and S. C. Huilgol, "Intense pulsed light therapy (IPL) induced iritis following treatment for a medial canthal capillary malformation," Australasian Journal of Dermatology 55(4), 289–291 (2014).
11. W. Rosenfield, S. Sadhev, V. Brunot, R. Jhaveri, I. Zabaleta, and H. E. Evans, "Phototherapy Effect on the Incidence of Patent Ductus Arteriosus in Premature Infants: Prevention With Chest Shielding," Pediatrics 78(1), 10–14 (1986).
12. H. S. Kim, E.-K. Kim, H.-E. Lee, Y.-K. Lee, C.-H. Park, K.-R. Park, J.-D. Park, B.-I. Kim, W.-H. Kim, J.-H. Choi, Y.-S. Yun, C.-K. Yun, and J.-M. Lee, "Influence of Phototherapy on Incidence of Patent Ductus Arteriosus in Very Low Birth Weight Infants," Journal of the Korean Pediatric Society 40(10), 1410–1418 (1997).
13. L. G. Henyey, J. L. Greenstein, "Diffuse radiation in the Galaxy," Astrophysical Journal 93, 70–83 (1941).
14. I. V. Yaroslavsky, A. N. Yaroslavsky, T. Goldbach, and H.-J. Schwarzmaier, "Inverse hybrid technique for determining the optical properties of turbid media from integrating-sphere measurements," Applied Optics 35(34), 6797–6809 (1996).
15. J. E. Dennis, R. B. Schnabel, Numerical Methods for Unconstrained Optimization and Nonlinear Equations, Prentice-Hall, Upper Saddle River (1983).
16. K. C. Chin, M. J. Moseley, and S. C. Bayliss, "Light transmission of phototherapy eyeshields," Archives of Disease in Childhood 62, 970–971 (1987).
17. J. Robinson, M. J. Moseley, A. R. Fielder, and S. C. Bayliss, "Light transmission measurements and phototherapy eyepatches," Archives of Disease in Childhood 66, 59–61 (1991).
18. S. G. H. Otman, L. D. El-Dars, C. Edwards, E. Ansari, D. Taylor, B. Gambles, I. Chalmers, and A. V. Anstey, "Eye protection for ultraviolet B phototherapy and psoralen ultraviolet A patients," Photodermatology Photoimmunology and Photomedicine 26(3), 143–150 (2010).
19. F. R. Abdulla, C. Breneman, B. Adams, and D. Breneman, "Standards for genital protection in phototherapy units," Journal of the American Academy of Dermatology 62(2), 223–226 (2010).
20. S. L. Jacques, M. O. Gaeeni, "Thermically induced changes in optical properties of heart," Images of the Twenty-First Century. Proceedings of the Annual International Engineering in Medicine and Biology Society 4, 1199–1200 (1989).
21. A. N. Yaroslavsky, P. C. Schulze, I. V. Yaroslavsky, R. Schober, F. Ulrich, and H.-J. Schwarzmaier, "Optical properties of selected native and coagulated human brain tissues in vitro in the visible and near infrared spectral range," Physics in Medicine & Biology 47(12), 2059–2073 (2002).
22. A. N. Bashkatov, E. A. Genina, V. I. Kochubey, and V. V. Tuchin, "Optical properties of human skin, subcutaneous and mucous tissues in the wavelength range from 400 to 2000 nm," Journal of Physics D: Applied Physics 38, 2543 (2005).
23. E. Salomatina, B. Jiang, J. Novak, and A. N. Yaroslavsky, "Optical properties of normal and cancerous human skin in the visible and near-infrared spectral range," Journal of Biomedical Optics 11(6), 064026 (2006).

An Analytical Solution of the Hyperbolic Bioheat Model of the Cornea Subjected to Laser Irradiation

Ram Autar and Anuj Kumar*
Department of Mathematics, Harcourt Butler Technical University, Kanpur 208002, India

* **e-mail:** kumaranuj979588@gmail.com

Abstract. The thermal effects occurring in a cornea subjected to short-pulsed laser irradiation during laser thermokeratoplasty (LTK) are investigated. The transient bioheat transfer is described by the hyperbolic model and solved analytically using the finite Fourier transform technique and the method of variation of parameters. The computational results predicted by the hyperbolic model show that the degree of damage in the corneal tissue induced by Ho: YAG laser irradiation under LTK surgery increases linearly with time. An increase in the convection coefficient of the anterior corneal surface causes an insignificant reduction in the corneal temperature, whereas an increase in the value of phase lag in the heat flux vector causes a rise in the corneal temperature. © 2022 Journal of Biomedical Photonics & Engineering.

Keywords: temperature; laser; cornea; refractive error; LTK; Finite Fourier transform technique; hyperbolic model.

Paper #3463 received 10 Nov 2021; revised manuscript received 11 Jul 2022; accepted for publication 12 Jul 2022; published online 6 Aug 2022. doi: 10.18287/JBPE22.08.030302.

1 Introduction

The estimation of the temperature in biological tissues is under the focus of researchers in recent years. This fact is important in some clinical surgery such as radiofrequency heating of tissues, laser heating of tissues, tumour therapy or some skin treatment such as tattoos [1]. In ophthalmology, laser thermal shrinkage of collagenous tissue has been used clinically and experimentally for several procedures, including laser thermokeratoplasty (LTK). The surgical outcome of many of these procedures suffers from limited predictability and uncertain long-term stability, mainly because of a poor understanding of the fundamental thermodynamic and biomechanical processes of laser-induced thermal shrinkage of collagenous tissue. A better understanding of the thermo-optical response of the cornea and the kinetics of thermal shrinkage could help to optimize the laser treatment parameters for LTK and other procedures relying on thermal shrinkage [2], and perhaps improve the stability and predictability of the outcome.

In recent years, several bioheat transfer models for temperature rise in biological tissues have been developed and simulated. Hobiny and Abbas [3], Alzahrani and Abbas [4]; and Abbas, Hobiny, and Alzaharani [5] have used the Laplace transformation technique to obtain analytical solutions to their hyperbolic bioheat transfer models under different conditions, while Hobiny and Abbas [6] have used the finite element approach to solve their bioheat model. Ghanami and Abbas [7], Hobiny and Abbas [8]; and Hobiny et al. [9] developed Fractional bioheat transfer models to determine the temperature and the thermal damage in the tissue and obtained analytical solutions to the models using the Laplace transform. In 2020, Hobiny and Abbas [10] used the finite element approach to find a numerical solution to their nonlinear dual phase lag bioheat model for the temperature changes and evaluated the thermal damage using the Arrhenius equation. In these works, it has been concluded that mathematical models are efficient tools to evaluate the bioheat transfer in living tissues.

In 2008, Ooi et al. [11] developed a boundary element model of the human eye under LTK surgery using classical heat diffusion equation for heat transfer and the Beer-Lambert law for energy absorption inside the cornea. The eye was modeled as comprising five distinct homogeneous thermally isotropic regions. The numerical solution to the model was obtained and the computational results for the corneal temperature field were presented through the graphs and discussed. Singh et al. [12] introduced a validated 3D finite volume model of the human eye to study laser

keratoplasty surgery. They considered the Pennes bio-heat equation for heat transfer and incorporated fluid convection in the model. The eye was treated as a region consisting of six homogeneous isotropic subdomains.

According to the review of literature, it is seen that the Pennes bio-heat equation is the most widely applied model for temperature distribution in living biological tissues. Fourier law assumes that heat flux and temperature change at any point appear at the same time instant. This implies that thermal signals propagate at an infinite speed [13]. Heat is always found to propagate at a finite speed. On the other hand, biological tissue has an inhomogeneous inner structure and found a phase lag time value. Mitra et al. [14] have shown experimental evidence of hyperbolic heat transfer in processed meat. They have used meat at different temperatures and brought them into contact suddenly and used thermocouples to measure the instantaneous temperature distributions. They have estimated a thermal phase lag time value to be around 16 sec. Kaminski [15] has also conducted some experiments with material with non-homogeneous inner structure and has found a phase lag time value of 20 sec. From the temperature distributions obtained, it can be inferred that parabolic and hyperbolic models produce similar results for smaller phase lag times, while they predict significantly different results when the lag times are large, suggesting that hyperbolic models are suitable to be used for biological systems with very complex internal structure. Gheitaghy et al. [16] proposed parabolic and hyperbolic models for heat transfer in the cornea under LTK surgery by considering the semi-infinite model of the cornea and solved the models using the mathematical analogy between thermal and electrical systems. The evaporation of heat at the anterior corneal surface was not considered. The computational results were presented by graphs and discussed.

In view of the importance and necessity of considering the thermal wave effects in bioheat transfer problems involving high heat flux incident on the tissue surface with a short duration, there is a need to formulate a hyperbolic model for the heat transfer in the corneal tissue subjected to short-pulsed Ho: YAG LTK irradiation. In the present study, a hyperbolic heat conduction model for the corneal temperature during LTK treatment to correct the refractive error in hyperopia is proposed by treating the cornea as a finite domain. Also, the evaporation of heat at the anterior corneal surface is incorporated into the model. The analytical solution to the model is derived using the finite cosine Fourier transform and the method of variation of parameters. The computational results for the temperature distribution and the temperature variation with time are presented by graphs and the influence of some model parameters on the distribution and variation are illustrated. Also, the degree of thermal damage in the cornea is evaluated and discussed.

2 Physical Model and Mathematical Formulation

The cornea subjected to short-pulsed laser irradiation at its anterior surface under LTK treatment is treated as a homogeneous finite domain of thickness L with constant thermal properties and thermally insulated bottom (endothelium surface) boundary. The Beer-Lambert Law, which experimentally asserts that the intensity of radiation drops exponentially with penetration depth, is used to describe the laser heat source.

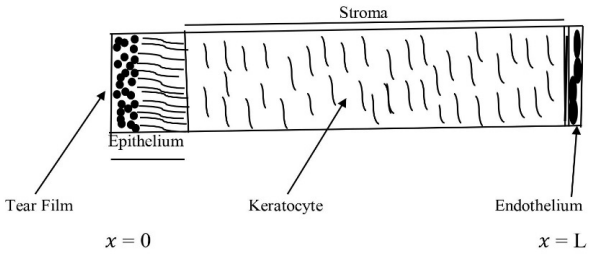


Fig. 1 Schematic diagram of the cornea modeled as a finite domain.

The heat transfer in living biological tissues is governed by Pennes model [17]:

$$\rho c \frac{\partial T(x,t)}{\partial t} = -\Delta \cdot q(x,t) + \\ +\rho_b c_b \omega_b (T_b - T(x,t)) + q_{mb} + Q(x,t), \quad (1)$$

where $\rho(\mathrm{kg}\cdot\mathrm{m}^{-3})$ is the tissue density, $c(\mathrm{J}\cdot\mathrm{kg}^{-1}\cdot{}^{\circ}\mathrm{C}^{-1})$ is the tissue-specific heat, $q(\mathrm{W}\cdot\mathrm{m}^{-2})$ is the heat flux, $\rho_b(\mathrm{kg}\cdot\mathrm{m}^{-3})$ is the blood density, $c_b(\mathrm{J}\cdot\mathrm{kg}^{-1}\cdot{}^{\circ}\mathrm{C}^{-1})$ is the blood specific heat, $\omega_b(\mathrm{s}^{-1})$ is the volumetric blood perfusion rate per unit volume, $T_b(^{\circ}\mathrm{C})$ is the blood temperature, $T(^{\circ}\mathrm{C})$ is the tissue temperature, $q_{mb}(\mathrm{W}\cdot\mathrm{m}^{-3})$ is the heat generation due to metabolism heat and $Q(\mathrm{W}\cdot\mathrm{m}^{-3})$ is the heat generated by laser energy and x,t are the space and time coordinates, respectively. The laser heat source $Q(x,t)$ is described as follows:

$$Q(x,t) = (1-f)\cdot I(t)\cdot \mu e^{-\mu x},$$

where f is the Fresnel surface reflectance, $I(t)(\mathrm{W}\cdot\mathrm{m}^{-2})$ is the laser intensity and $\mu(\mathrm{m}^{-1})$ is the absorption coefficient.

It could be overlooked due to the relatively small amount of metabolic heat compared to the heat generated by laser accidents [16]. Moreover, since corneal tissue is avascular, the blood perfusion rate at the targeted location is nearly zero. Therefore, $q_{mb} = 0, w_b = 0$. Now, Eq. (1) reduces to the following form:

$$\rho c \frac{\partial T(x,t)}{\partial t} = -\Delta \cdot q(x,t) + Q(x,t). \quad (2)$$

The Fourier law of heat conduction, which is a simple linear empirical relation between the heat flux vector and the temperature gradient is given by

$$q(x,t) = -k \frac{\partial T(x,t)}{\partial x}, \quad (3)$$

where $k(\mathrm{W \cdot m^{-1} \cdot °C^{-1}})$ is the corneal tissue thermal conductivity.

The hyperbolic model is obtained by adding the parameter τ_q to time-variable t in $q(x,t)$ of Fourier law Eq. (4), is given by

$$q(x,t+\tau_q) = -k \frac{\partial T(x,t)}{\partial x}, \quad (4)$$

where τ_q is the relaxation time of heat flux. Taylor series expansion of first-order approximation of Eq. (4) with respect to time t is given by

$$q(x,t) + \tau_q \frac{\partial q(x,t)}{\partial t} = -k \frac{\partial T(x,t)}{\partial x}. \quad (5)$$

On solving Eqs. (2) and (5), we get a hyperbolic model of the bioheat transfer equation:

$$\tau_q \frac{\partial^2 T(x,t)}{\partial t^2} + \frac{\partial T(x,t)}{\partial t} = \alpha \frac{\partial^2 T(x,t)}{\partial x^2} + \\ + \frac{1}{\rho c}[Q(x,t) + \tau_q \frac{\partial Q(x,t)}{\partial t}], \quad (6)$$

where $\alpha = \frac{k}{\rho c}(\mathrm{cm^2 \cdot sec^{-1}})$ the thermal diffusivity of the corneal tissue.

To solve the hyperbolic bioheat conduction Eq. (6) the following physically realistic and mathematically consistent conditions are prescribed.

Initial conditions:

$$T(x,t) = T_0, \text{ at } t = 0, \quad (7)$$

$$\frac{\partial T(x,t)}{\partial t} = 0, \text{ at } t = 0. \quad (8)$$

Boundary conditions:

$$-k \frac{\partial T(x,t)}{\partial x} = h_0(T(x,t) - T_0) + \\ + \sigma\varepsilon(T^4(x,t) - T_0^4) + E, \quad (9)$$

at $x = 0$,

$$\frac{\partial T(x,t)}{\partial x} = 0, \text{ at } x = L, \quad (10)$$

where $h_0(\mathrm{W \cdot m^{-2} \cdot K^{-1}})$ the convection coefficient, T_0 (℃) initial tissue temperature, $\sigma(\mathrm{W \cdot m^{-2} \cdot K^{-4}})$ the Stefan Boltzmann constant, ε the emissivity of the corneal surface, $E(\mathrm{W \cdot m^{-2}})$ the evaporative heat loss.

The heat loss at the anterior surface of the cornea is caused by convection, emission, and evaporation, as per the boundary condition (10). The posterior surface of the cornea is thermally insulated, according to boundary condition (11).

To non-dimensionalize the governing equation, the following scheme is introduced:

$$X = \frac{\omega x}{2\alpha}, \tau = \frac{t}{2\tau_q}, \psi = \frac{Q\tau_q}{\rho c T_0}, \theta = \frac{T}{T_0}.$$

The dimensionless form of Eq. (7) is

$$\frac{\partial^2 \theta}{\partial \tau^2} + 2\frac{\partial \theta}{\partial \tau} = \frac{\partial^2 \theta}{\partial X^2} + 2\psi_0 \left[2\eta(\tau) + \frac{\partial \eta(\tau)}{\partial \tau} \right], \quad (11)$$

where $\Psi(X,\tau) = \psi_0 \eta(\tau) e^{-\beta X}$, $\psi_0 = \frac{\beta I_r (1-f)}{2\omega\rho c T_0}$, $\beta = 2\omega\tau_q\mu$ and $\eta(\tau)$ is the dimensionless rate of energy absorbed in the tissue. The laser heat source term is expressed in terms of arbitrary reference laser intensity I_r as $I(\tau) = I_r\, \eta(\tau)$.

The dimensionless forms of the initial and boundary conditions are

$$\theta(X,\tau) = 1, \text{ at } \tau = 0, \quad (12)$$

$$\frac{\partial \theta(X,\tau)}{\partial \tau} = 0, \text{ at } \tau = 0, \quad (13)$$

$$-B\frac{\partial \theta}{\partial X} = F(\theta - 1) + H(\tilde{\theta}^2 + 1)(\tilde{\theta} + 1)(\theta - 1) + G, \\ \text{at } X = 0, \quad (14)$$

$$\frac{\partial \theta}{\partial X} = 0, \text{ at } X = \frac{\omega L}{2\alpha}, \quad (15)$$

where $F = \frac{hT_0}{I_r}, H = \frac{\sigma\varepsilon T_0^4}{I_r}, G = \frac{E}{I_r}, B = \frac{\omega\rho c T_0}{2I_r}$.

3 Solution to the Mathematical Model

Taking the Finite cosine transform of Eq. (11) and using boundary conditions (14) and (15) yields:

$$\frac{\partial^2\overline{\theta(n,\tau)}}{\partial\tau^2}+2\frac{\partial\overline{\theta(n,\tau)}}{\partial\tau}+\lambda_n^2\overline{\theta(n,\tau)}=$$
$$=\frac{1}{B}\left[\begin{array}{l}F(\theta(0,\tau)-1)+H(\tilde{\theta}^2+1)(\tilde{\theta}+1)\times\\ \times(\theta(0,\tau)-1)+G\end{array}\right]+$$
$$+\frac{2\psi_0\beta}{\lambda_n^2+\beta^2}\left[1-(-1)^n\exp(-\beta L)\right]\times$$
$$\times\left[2\eta(\tau)+\frac{\partial\eta(\tau)}{\partial\tau}\right], \qquad (16)$$

where $\lambda_n=\dfrac{n\pi}{L}$ ($n=0,\ 1,\ 2,\ 3...$ is the finite Fourier discrete variable) are the eigenvalues and $\overline{\theta(n,\tau)}=\int_0^L\theta(X,\tau)\cos(\lambda_n X)\mathrm{d}X$ is the finite cosine transformation of dimensionless temperature.

Moreover, the transformed initial conditions (12) and (13) are $\overline{\theta(n,0)}=0,\dfrac{\mathrm{d}\overline{\theta(n,0)}}{\mathrm{d}\tau}=0$.

The complementary solution of Eq. (16) is

$$\overline{\theta(n,\tau)_c}=C_1\exp(\sigma_n\tau)+C_2\exp(\delta_n\tau),$$

where C_1 and C_2 are constants to be determined, $\sigma_n=-1-\sqrt{1-\lambda_n^2}$ and $\delta_n=-1+\sqrt{1-\lambda_n^2}$.

Wronskian $W=(\delta_n-\sigma_n)\exp(\delta_n+\sigma_n)\tau=2\sqrt{1-\lambda_n^2}\exp(-2\tau)$.

Using the method of variation of parameters, the Particular solution of Eq. (16) is

$$\overline{\theta(n,\tau)_p}=$$
$$=\frac{1}{\sqrt{1-\lambda_n^2}}\left[\int_0^\tau\left\{\begin{array}{l}\dfrac{1}{B}(F(\theta(0,r)-1+H(\tilde{\theta}^2+1)\times\\ \times(\tilde{\theta}+1)(\theta(0,r)-1+G)+\\ +\dfrac{2\psi_0\beta}{\lambda_n^2+\beta^2}\left[1-(-1)^n\exp(-\beta L)\right]\times\\ \times\left(2\eta(\tau)+\dfrac{\partial\eta(\tau)}{\partial\tau}\right)\end{array}\right\}\times\right.$$
$$\left.\times\exp(-(\tau-r))\sinh\left(\sqrt{1-\lambda_n^2}(\tau-r)\right)\mathrm{d}r\right].$$

Using the transformed initial conditions of Eqs. (12) and (13) the arbitrary constants C_1 and C_2 can be determined as:

$$C_1=\frac{1}{2(1-\lambda_n^2)}\frac{\mathrm{d}S}{\mathrm{d}\tau}\bigg|_{\tau=0},C_2=-\frac{1}{2(1-\lambda_n^2)}\frac{\mathrm{d}S}{\mathrm{d}\tau}\bigg|_{\tau=0},$$

where

$$S=\left[\int_0^\tau\left\{\begin{array}{l}\dfrac{1}{B}(F(\theta(0,r)-1)+H(\tilde{\theta}^2+1)\times\\ \times(\theta+1)(\theta(0,r)-1+G)+\\ +\dfrac{2\psi_0\beta}{\lambda_n^2+\beta^2}\left[1-(-1)^n\exp(-\beta L)\right]\times\\ \times\left(2\eta(\tau)+\dfrac{\partial\eta(r)}{\partial\tau}\right)\end{array}\right\}\times\right.$$
$$\left.\times\exp(-(\tau-r))\sinh\left(\sqrt{1-\lambda_n^2}(\tau-r)\right)\mathrm{d}r\right].$$

The general solution of Eq. (16) is

$$\overline{\theta(n,\tau)}=\frac{1}{2(1-\lambda_n^2)}\frac{\mathrm{d}S}{\mathrm{d}\tau}\bigg|_{\tau=0}\exp(\sigma_n\tau)-$$
$$-\frac{1}{2(1-\lambda_n^2)}\frac{\mathrm{d}S}{\mathrm{d}\tau}\bigg|_{\tau=0}\exp(\delta_n\tau)+\frac{S}{\sqrt{1-\lambda_n^2}}. \qquad (17)$$

Taking the inverse finite Fourier transform of Eq. (17) using Eq. (18) to get the temperature distribution during LTK surgery

$$\theta(X,\tau)=\frac{\overline{\theta(0,\tau)}}{L}+\frac{2}{L}\sum_{n=1}^{\infty}\overline{\theta(n,\tau)}\cos(\lambda_n X). \qquad (18)$$

3.1 Thermal Damage

The smooth epithelial surface of the cornea blocks the passage of foreign materials such as dust, water and bacteria in the eye and absorbs oxygen and nutrients from the tears to supply to the rest of the cornea. To keep corneal hydration at its natural physiologic state, the endothelium actively pumps fluids into the anterior chamber. Maintaining adequate hydration is necessary for corneal opacity. During the LTK treatment procedure for hyperopia, the corneal temperature may rise to levels that cause significant epithelium surface vaporisation and endothelium thermal damage. The monitoring of temperature rise and maintaining optimal temperature during the treatment is required to avoid epithelium vaporisation and endothelium thermal damage. A numerical measure of the degree of damage in the corneal tissue may be a useful measure in the understanding and monitoring of corneal temperature.

According to Fyodorov et al. [18], the minimum corneal temperature should be 55 °C, Haw and Manche [19], the maximum temperature allowed is 75 °C, and Asbell et al. [20], the best temperature for optimal cornea collagen shrinking is 65 °C. Additionally, Aksan and McGrath [21] demonstrated the need of avoiding high temperatures and extensive denaturation to prevent tissue stiffness. As a result, the safe shrinking temperature range is 55–75 °C. Shrinkage occurs primarily during laser pulses and ceases immediately after the cooling phase between laser pulses begins. When the temperature of the corneal surface (epithelium) rises above 100 °C during treatment, thermal damage

begins, indicating that the epithelium is at risk of superficial vaporisation. The following well-known Arrhenius equation has been widely utilised to assess thermal damage in biological tissue. The damage integral given by

$$\Omega(\tau,\theta)=\int_0^{\tau} A\exp(-\frac{E_a}{R\theta})d\tau,$$

where $A(\sec^{-1})$ is a rate constant, $E_a(\mathrm{J}\cdot\mathrm{mol}^{-1})$ activation energy and $R(\mathrm{J}\cdot\mathrm{mol}^{-1}\cdot\mathrm{K}^{-1})$ the universal gas constant. The upper limit of the integral is usually taken to be the time at which the tissue returns to its initial temperature.

4 Results and Discussion

The computational results for the temperature profile and temperature variation with time in corneal tissue irradiated by Ho: YAG laser under LTK treatment are obtained using the values of typical parameters listed in the table below and displayed as graphs.

The variation of the degree of damage in the corneal tissue with time caused by laser irradiation during LTK surgery is portrayed in Fig. 2. It is evident from the graph that the highest degree of damage ($\Omega = 0.18$) is detected at $\tau = 0.7$ in the central stroma of the cornea, which is consistent with the literature [22]. In view of the observations [22, 23] that $\Omega = 0.1$ corresponds to the commencement of collagen denaturation and $\Omega > 1$ implies irreversible thermal damage in the tissue, it is discovered that collagen denaturation occurs during the time interval [0.36, 0.7] of the treatment. As a result, proper measures should be taken during LTK surgery to avoid the severity of thermal damage. By restricting the duration of laser heat, $\tau < 0.36$, the collagen denaturation in the corneal stroma may be avoided.

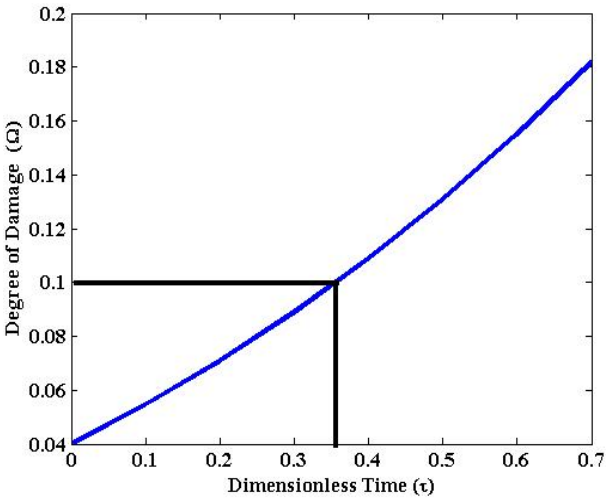


Fig. 2 Time-dependent degree of damage in the corneal tissue during Ho:YAG LTK.

Table 1 Parameters used in Computations.

Parameter	Symbol	Magnitude	Dimension
Corneal density	P	1062	$\mathrm{kg}\cdot\mathrm{m}^{-3}$
Corneal thermal conductivity	k	0.556	$\mathrm{W}\cdot\mathrm{m}^{-1}\cdot{}^{\circ}\mathrm{C}^{-1}$
Fresnel surface reflectance	f	2.4%	–
Absorption coefficient	M	2000	m^{-1}
Thermal diffusivity	α	0.001452	$\mathrm{cm}^2\cdot\mathrm{sec}^{-1}$
Emissivity of cornea	ε	0.975	–
Universal gas constant	R	8.32	$\mathrm{J}\cdot\mathrm{mol}^{-1}\cdot\mathrm{K}^{-1}$
Activation energy	E_a	402.688	$\mathrm{J}\cdot\mathrm{mol}^{-1}$
Rate constant	A	$3.13\cdot10^{61}$	$\sec^{-1}$
Stefan Boltzmann constant	σ	$5.67\cdot10^{-8}$	$\mathrm{W}\cdot\mathrm{m}^{-2}\cdot\mathrm{K}^{-4}$
Wavelength	Λ	2.1	μm
Specific heat	C	3830	$\mathrm{J}\cdot k\mathrm{g}^{-1}\cdot\mathrm{K}^{-1}$
Initial temperature	T_0	35	℃
Evaporative heat loss	E	40	$\mathrm{W}\cdot\mathrm{m}^{-2}$
Phase lag in heat flux	τ_q	1	sec
Thickness of cornea	L	0.55	Mm
Reference laser intensity	I_r	$2\cdot10^4$	$\mathrm{W}\cdot\mathrm{m}^{-2}$
Convection coefficient	H	20	$\mathrm{W}\cdot\mathrm{m}^{-2}\cdot\mathrm{K}^{-1}$
Pulse duration	t_i	200	$\mu\cdot\sec$

A comparison of the corneal temperature variations with time predicted by the parabolic model and the hyperbolic model is illustrated in Fig. 3. The temperature response predicted by Fourier's model (parabolic model) decreases with time rapidly, whereas the temperature predicted by the hyperbolic model decreases with time slowly. Most of the time, the temperature predicted by the hyperbolic model is higher than that predicted by the parabolic model. Similar comparisons of the theoretical results have been presented by H. Moosavi et al. [24] and Gheitaghy et al. [16].

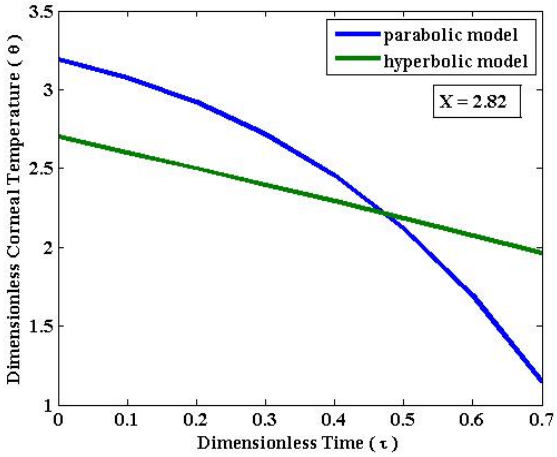


Fig. 3 A comparison of Fourier's model and the hyperbolic model anticipated dimensionless temperature variations over time during irradiation with a pulsed Ho: YAG laser.

The corneal temperature profiles at three different time durations have been shown in Fig. 4. It is observed from the curves that the temperature decreases along the length of the cornea. This behaviour occurs because the heat absorbed by the cornea decreases with the depth of the cornea. If the value of time duration is increased, the temperature rises throughout the cornea.

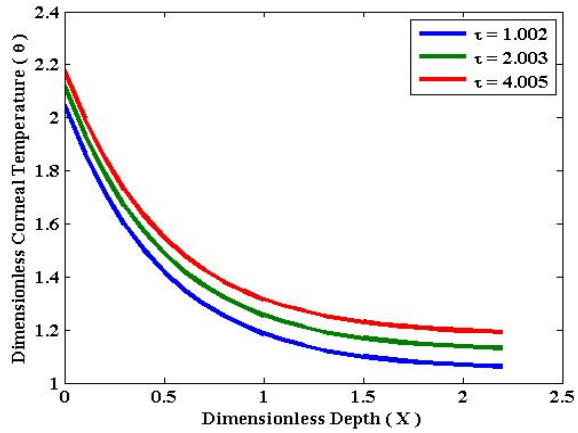


Fig. 4 Corneal temperature distribution at different times during pulsed Ho:YAG laser irradiation.

Fig. 5 depicts the influence of the convection coefficient on the temperature variations with time at the anterior corneal surface. The convection coefficient appears to have an insignificant impact on the temperature changes. During the time under discussion, the temperature at the anterior surface decreases with time. A similar result was predicted by the model of A. M. Gheitaghy et al. [16].

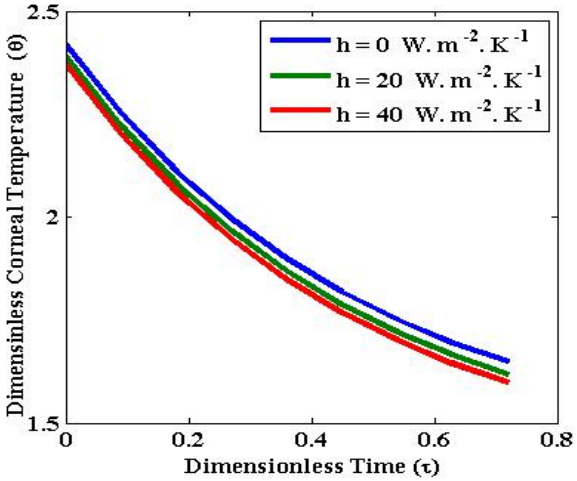


Fig. 5 The effect of the convection coefficient on the temperature variation with time predicted by the hyperbolic model.

Fig. 6 depicts the effect of the relaxation time on the dimensionless corneal temperature profile. It is observed from the figure that with an increase in the relaxation time of heat flux, the temperature rises and that the wavefront is more observable in the case of larger τ_q. Since τ_q is normally interpreted as the non-zero time that accounts for the effect of "thermal inertia", τ_q is responsible for the delay in establishing heat flux and associated conduction through the medium. This agrees qualitatively with the theoretical results of A. M. Gheitaghy et al. [16].

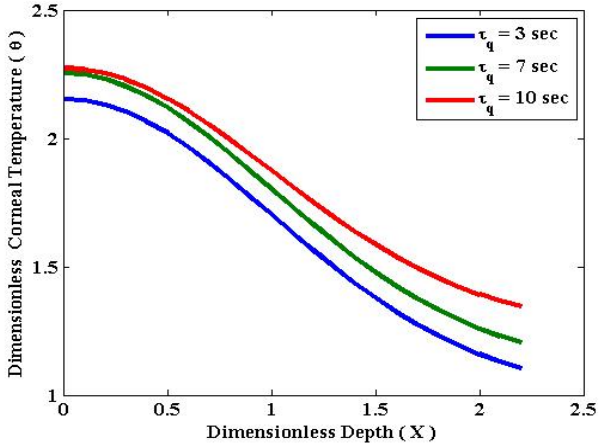


Fig. 6 The Temperature profile at various τ_q values in the corneal tissue at $\tau = 0$.

5 Conclusion

In this study, the hyperbolic heat conduction model is used to describe temperature changes in the human cornea exposed to short-pulsed Ho:YAG laser heating during LTK surgery, as well as to investigate the effect of phase-lags in the heat-flux on the corneal temperature distribution and temperature variation over time. It is observed that the temperature response anticipated by Fourier's model (Parabolic model) falls rapidly with time, whereas the temperature reduction predicted by the hyperbolic slows down with time. The temperature of the cornea rises as the heat flux phase-lag increases. It is necessary to verify the accuracy of the current findings by comparing the analytical results to the experimental data. Once, if the model is validated in near future, it may be utilised to improve the design of laser surgery for hyperopia treatment.

Disclosures

All authors declare that there is no conflict of interests in this paper.

Acknowledgments

The financial assistance for this work, received through award no. 09/1230 (0001)/2018-EMR-I from the Council of Scientific and Industrial Research, New Delhi is gratefully acknowledged. The authors express their sincere thanks to the reviewers for their constructive comments, valuable suggestions and contribution to the improvement of the article.

References

1. P. Hooshmand, A. Moradi, and B. Khezry, "Bioheat transfer analysis of biological tissues induced by laser irradiation," International Journal of Thermal Sciences 90, 214–223 (2015).
2. J. E. Fulton, T. Barnes, "Collagen shrinkage (selective dermatoplasty) with the high-energy pulsed carbon dioxide laser," Dermatologic Surgery 24, 37–41 (1998).
3. A. D. Hobiny, I. A. Abbas, "Theoretical analysis of thermal damages in skin tissue induced by an intense moving heat source," International Journal of Heat and Mass Transfer 124, 1011–1014(2018).
4. F. S. Alzahrani, I. A. Abbas, "Analytical estimations of temperature in a living tissue generated by laser irradiation using experimental data," Journal of Thermal Biology 85, 10241(2019).
5. I. Abbas, A.Hobiny, and F. Alzahrani, "An analytical solution of the bioheat model in a spherical tissue due to laser irradiation," Indian Journal of Physics 94, 1329–1334 (2019).
6. A.Hobiny, I. Abbas, "Thermal response of cylindrical tissue induced by laser irradiation with experimental study," International Journal of Numerical Methods for Heat & Fluid flow 22(8), 4013–4023 (2019).
7. A. Ghanmi, I. A. Abbas, "An analytical study on the fractional transient heating within the skin tissue during the thermal therapy," Journal of Thermal Biology 82, 229–233(2019).
8. A. Hobiny, I. Abbas, "Analytical solutions of fractional bioheat model in a spherical Tissue," An International Journal of Mechanics Based Design of Structures and Machines 49(3), 430–439 (2019).
9. A. Hobiny, F. Alzahrani, I. Abbas, and M. Marin, "The effect of fractional time derivative of bioheat model in skin tissue induced to laser irradiation," Symmetry 12(4), 602 (2020).
10. A. D. Hobiny, I. A. Abbas, "Nonlinear analysis of dual-phase lag bio-heat model in living tissues induced by laser irradiation," Journal of Thermal Stresses 43(4), 503–511(2020).
11. E. H. Ooi, W.-T. Ang, and E. Y. K Ng, "A boundary element model of the human eye undergoing laser thermoKeratoplasty," Computers in Biology and Medicine 38(6), 727–737 (2008).
12. D. Singh, K. Firouzbakhsh, and M. T. Ahmadian, "Laser Keratoplasty in Human Eye Considering the Fluid Aqueous Humor and Vitreous Humor Fluid Flow," International Journal of Me-chanical and Mechatronics Engineering 11(4), 776–786 (2017).
13. N. A. Peppers, "Corneal damage threshold for CO2 laser irradiation," Applied Optics 8(2), 377–381(1969).
14. K. Mitra, S. Kumar, A. Vedevarz, and M. K. Moallemi, "Experimental evidence of hyperbolic heat conduction in processed meat," Journal of Heat Transfer 117(3), 568–573(1995).
15. W. Kaminski, "Hyperbolic heat conduction equation for materials with a nonhomogeneous inner structure," Journal of Heat Transfer 112(3), 555–560 (1990).
16. A. M. Gheitaghy, B. Takabi, and M. Alizadeh, "Modeling of ultrashort pulsed laser irradiation in the cornea based on parabolic and hyperbolic heat equations using an electrical analogy," International Journal of Modern Physics C 25(9), 1450039 (2014).
17. A. Narasimhan, S. Sadasivam, "Non-Fourier bioheat transfer modelling of thermal damage during retinal laser irradiation," International Journal of Heat and Mass Transfer 60, 591–597(2013).
18. S. N. Fyodorov, V. V. Durnev, "Operation of dosages dissection of the corneal circular ligament in cases of myopia of mild degree," Annals of Ophthalmology 11(12), 1885–1890 (1979).
19. W. W. Haw, E. E. Manche, "Conductive keratoplasty and laser thermal keratoplasty," International Ophthalmology Clinics 42(4), 99–106 (2002).

20. P. A. Asbell, R. K. Maloney, J. M. Davidorf, P. S. Hersh, M. B. Mcdonald, and E. E. Manche, "Conductive keratoplasty for the correction of hyperopia," Transactions of the American Ophthalmological Society 99, 79–87 (2001).
21. A. Aksan, J. J. McGrath, "Thermomechanical analysis of soft tissue thermo-therapy," Journal of Biomechanical Engineering 125(5), 700–708 (2003).
22. T. L. Naoumidi, I. G. Pallikaris, I. Naoumidi, and N. I. Astyrakakis, "Conductive Keratoplasty: Histological Study of Human Corneas," American Journal of Ophthalmology 140(6), 984–992 (2005).
23. B. Jo, A. Aksan, "Prediction of the extent of thermal damage in the cornea during conductive keratoplasty," Journal of Thermal Biology 35(4), 167–174 (2010).
24. H. Moosavi, A. Moradi, and M. Parastarfeizabadi, "Investigation on the dual-phase lag effects in biological tissues during laser irradiation," International Journal of Mechanic Systems Engineering 4(4), 33–46 (2014).

Study of the Diffusion of Tetracycline in the Dentin of the Human Tooth *Ex Vivo*

Alexey A. Selifonov[1*], Tatyana Yu. Rusanova[2], Ekaterina I. Selifonova[1], and Valery V. Tuchin[3]

[1] Education and Research Institute of Nanostructures and Biosystems, Saratov State University, 83 Astrakhanskaya str., Saratov 410012, Russian Federation

[2] Institute of Chemistry, Saratov State University, 83 Astrakhanskaya str., Saratov 410012, Russian Federation

[3] Science Medical Center, Saratov State University, 83 Astrakhanskaya str., Saratov 410012, Russian Federation

*** e-mail:** peshka029@gmail.com

Abstract. Currently, manufacturers of tetracycline and tetracycline antibiotics necessarily warn about possible side effects when using tetracycline in children under 8 years of age and pregnant women. When tetracycline is used in utero or after birth, before the teeth erupt through the gum during mineralization or calcification, the antibiotic binds to calcium ions, which causes persistent gray or brown stains or often streaks on the teeth. In the present study, the diffuse reflectance spectroscopy with an integrating sphere was used to determine the molecular diffusion coefficient of tetracycline in the dentin of a human tooth *ex vivo*, which was found as $D = (6.49 \pm 1.12) \cdot 10^{-6}$ cm^2/s. The dependences following from Fick's second law and the modified Bouguer-Lambert-Beer law, as well as restrictions for the free diffusion model, were used in the calculations. It was found that when dentinal samples are saturated with tetracycline hydrochloride, the total transmittance decreases over the entire studied wavelength range from 200 to 800 nm. These studies are important for clinical practice. © 2022 Journal of Biomedical Photonics & Engineering.

Keywords: tetracycline hydrochloride; human dentin; molecular diffusion; diffuse reflectance spectroscopy; integrating sphere; free diffusion model.

Paper #3493 received 10 May 2022; revised manuscript received 11 Jul 2022; accepted for publication 18 Jul 2022; published online 15 Aug 2022. doi: 10.18287/JBPE22.08.030303.

1 Introduction

Tetracycline is a broad-spectrum antibiotic. It is produced in the form of a base and hydrochloric acid salt. It has a bacteriostatic effect due to the suppression of protein synthesis of pathogens caused by a violation of the formation of a complex between the transport ribonucleic acid and the ribosome [1]. Until the 1980s and 1990s, tetracycline was actively prescribed to patients suffering from such diseases as pneumonia and respiratory tract infections caused by Mycoplasma pneumoniae, respiratory tract infections caused by Haemophilus influenzae and Klebsiella spp., bacterial infections of the urinary and reproductive system, skin infections and soft tissues, ulcerative necrotic gingivitis, stomatitis, conjunctivitis, acne, actinomycosis, intestinal amoebiasis, anthrax, brucellosis and many others [2]. The maximum concentration of the antibiotic in the human body is reached within about 3 hours and over the next 8 hours the concentration gradually decreases. It is distributed unevenly in the body, the maximum concentration is found in the liver, kidneys, lungs, and in the spleen, lymph nodes [2]. It accumulates in large quantities in bone tissue, tumor tissues, in dentin and enamel of primary teeth [3].

Patients taking tetracycline-based antibiotics have included pregnant women and young children. At the same time, medical science had not yet fully deciphered the side effects of this drug which include permanent staining or discoloration of teeth that are not fully formed (i.e., in children under eight years of age) [4]. When using tetracycline in childhood, as well as with intrauterine or ectopic exposure before teething through the gums during mineralization or calcification of the teeth, the antibiotic binds to calcium ions in the teeth. This results in persistent permanent staining in the teeth. In dentistry, the term "tetracycline teeth" even arose. The first case of discoloration of teeth in children was reported in 1956,

followed by many others [5, 6]. The warning about this effect also extends to a number of tetracycline derivatives including doxycycline and minocycline, and others [7]. Staining and discoloration of teeth with tetracycline depends on the dosage used, the duration of treatment or exposure, the stage of mineralization (or calcification) of the teeth, and the degree of the mineralization process activity. The spots can be gray or brown in color and often appear in stripes around the teeth. During teething and exposure to light, calcium-bound tetracycline oxidizes causing enamel discoloration from fluorescent yellow to brown.

The location of the discoloration directly correlates with the stage of tooth development during tetracycline exposure. The age range for the development of pathology begins from the 2nd trimester of intrauterine development and up to 8–9 years of growing up. During this period, calcification of the teeth occurs. Calcification of primary teeth may occur before the age of 10–14 months, anterior permanent teeth between 6 months and 6 years of age, and posterior permanent teeth before the age of 8 years [8, 9]. Therefore, exposure to tetracycline during any of these periods of calcification may result in irreversible staining. Cases of discoloration in adults have been reported, minocycline causes tooth discoloration in 3–6% of adults who take a daily dose of more than 100 mg for more than one month [10, 11]. The discoloration is less noticeable in adults due to the lack of free calcium in tooth enamel.

Does tetracycline cause cavities? There is information from dental experts who believe that the drug can sometimes bind to calcium phosphate in the teeth of young children and lead to its absorption by the tissues of the teeth and form tiny pits in the enamel which contributes to the development of caries [12]. However, most dentists tend to believe that the worst thing that tetracycline can do is permanently stain children teeth, and many other factors can provoke caries [13]. Can tetracycline teeth be whitened effectively? Not always. Tetracycline stains are different from coffee, tea, or wine stains. Unlike the latter, which exist only on the surface of the teeth, tetracycline staining is found inside the teeth. This means that "tetracycline teeth" cannot be whitened with toothpaste, strips, and home whitening kits. However, this does not mean that it is impossible to get rid of tetracycline stains on teeth with whitening. Internal professional teeth whitening can improve the appearance of teeth that are not too discolored [14]. In cases of severe tetracycline damage, the dentist may suggest the use of veneers and crowns to address the aesthetic problem in order to change your confidence in your smile.

Currently, manufacturers of tetracycline and tetracycline antibiotics necessarily warn about possible side effects when using tetracycline in children under 8 years of age. Structure-activity-relationship (SAR) of tetracycline family, which shows the bioactivity, strength and selectivity to the biological target, makes it valuable for labeling with radioisotopes. Up till now there are a few numbers of analogues of tetracycline which are labeled with radioisotopes and clinically used for treatment of bacterial and non-bacterial diseases [15].

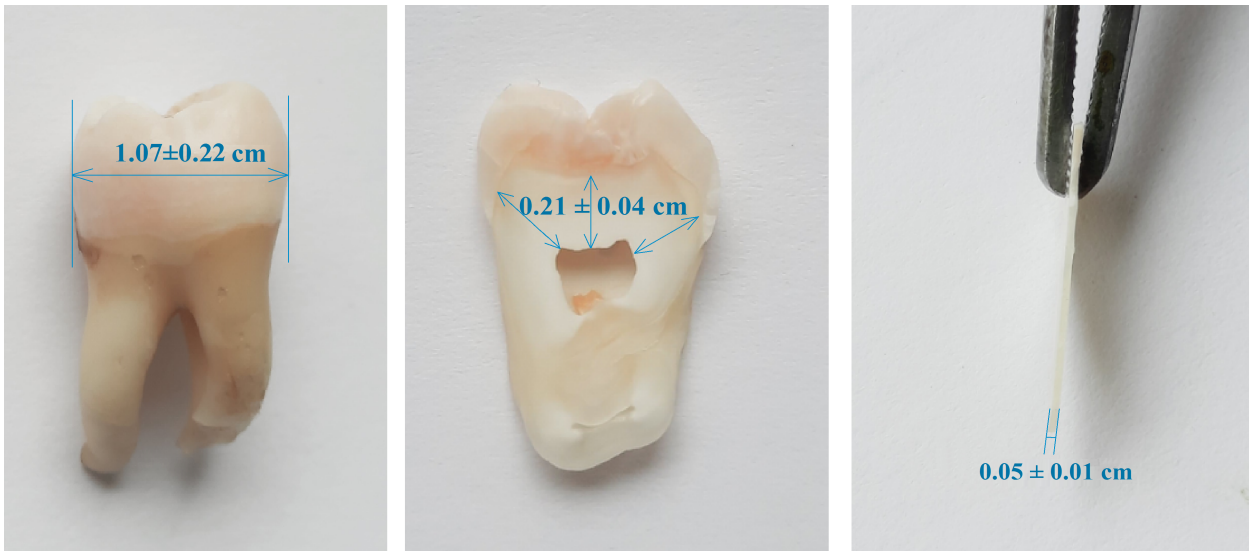
One of the effective methods of treating bacterial infections of the oral cavity, including teeth, is photodynamic therapy in which tissues are stained with a photosensitizer that mediates the generation of singlet oxygen and other reactive oxygen species (ROS) when irradiated with light of a certain wavelength. Tetracyclines are able both to kill bacteria due to the formation of ROS during staining of bacteria and exposure to light, and to prevent the growth of bacteria due to inhibition of ribosomes [16]. For example, doxycycline is effectively excited by light at a wavelength of 365 nm, and demeclocycline by UV and blue light (415 nm). The time and efficiency of staining are critical issues in the application of phototherapy in the clinic, so the measurement of the diffusion rate of a photosensitizer, in particular tetracycline, in the tooth tissue is of great importance. Quantitative parameters characterizing the penetration of a photosensitizer into tissues are necessary to determine the optimal concentration that provides safe and effective treatment. The method described in this study is also applicable to other tissues and photosensitizers [17].

So far, there are no quantitative data on the relative concentration of tetracyclines in tissues compared with blood serum, although such data are important for predicting treatment. New studies on the pharmacokinetics of tetracyclines are needed to understand the entire chain of oral tetracycline delivery from the stomach to the dentin at per oral administration. It is known that in the blood plasma tetracyclines find the maximum concentration after their administration in 2–3 hours [18]. Evidently, it is necessary to determine the entire path of molecules delivery from stomach to dentin. In this study, we offer investigation of only one important pathway in the entire chain and determine how long the tetracycline molecules will go from pulp (blood supply) to dentin and stain it.

The aim of this study was to determine the kinetic parameters of the penetration of a solution of tetracycline hydrochloride into the dentin of a human tooth. Namely, to quantify the diffusion coefficient of an antibiotic in dentin by diffuse reflectance spectroscopy using a free diffusion model.

2 Methods and Materials

The material for the *ex vivo* study was the saw cuts of human teeth, which were extracted from patients in a dental clinic for orthodontic indications. Sections were taken from three different teeth (molars) belonging to different patients aged 18, 37, 45 years (Fig. 1(a, b)). The extracted teeth were stored in saline at 5 °C in a dark place. Wet teeth were cut with a diamond disc into



(a) (b) (c)

Fig. 1 Photo of the studied samples of human teeth (molars): (a) a whole tooth; (b) the investigated saw cut with the distance from the pulp to the enamel; (c) 0.05 cm thick saw cut to study ASTH diffusion.

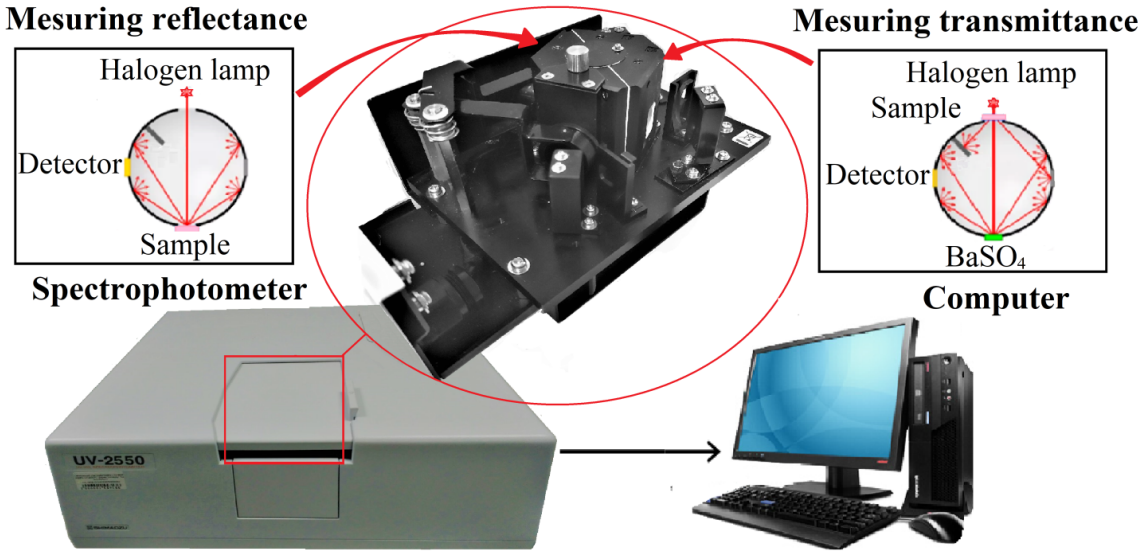


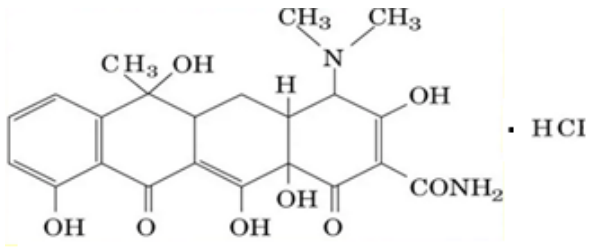
Fig. 2 Experimental scheme for measuring the spectra of total reflection and total transmittance.

longitudinal sections about 0.5 mm thick. Sections were placed for 20 sec in 35% phosphoric acid. To clean the surface from sawing products, the samples were placed in a Techsonic UD100 SH-45 L ultrasonic bath with water for 10 min and then wiped with a brush dipped in alcohol. The samples were dried in air for several days. The thickness of cuts (samples) of biological tissue was measured with a micrometer, the measurements were carried out at several points of the sample and averaged. The accuracy of each measurement is ±10 μm. In total, three cuts (samples) of different teeth were studied. The thickness of the dentin saw cut averaged 0.05 ± 0.01 cm (for $n = 3$, n is the number of samples) (Fig. 1(c)).

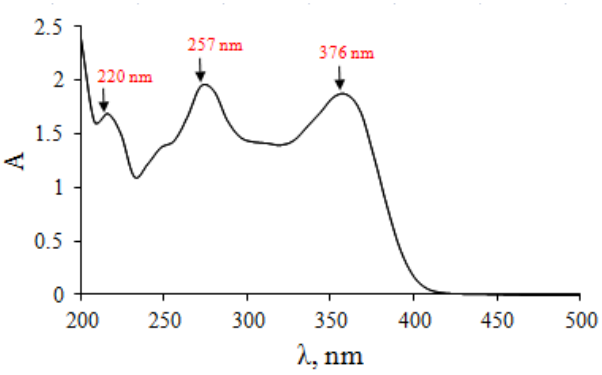
To measure the total transmittance and diffuse reflectance of tissue samples in the spectral range of 200–800 nm, a Shimadzu UV-2550 double-beam spectrophotometer (Japan) with an integrating sphere was used (Fig. 2). The radiation source was a halogen lamp with radiation filtering in the investigated spectral range. The limiting resolution of the spectrometer was 0.1 nm. The spectra were normalized before measurements using the $BaSO_4$ reference reflector, which has suitable UV properties. All measurements were carried out at room temperature (~25 °C) and normal atmospheric pressure. Each sample of the tissue under study was fixed in a special frame with a 0.5×0.5 cm window in a quartz cuvette so that the tissue sample was pressed against the wall of the cuvette and subjected to optical measurement. To measure the total transmission spectra (TTS), a quartz cuvette with a tissue sample was placed directly in front of the integrating sphere, collecting all radiation that passed

through the tissue sample. The diameter of the light beam incident on the sample was 3 mm.

The structural formula of tetracycline is shown in Fig. 3(a). Tetracycline hydrochloride in powder form retains its properties for more than two years. Tetracycline solutions are unstable, an alkaline solution at pH = 8.85 under normal conditions loses its effectiveness by 50% within 12 hours, in acidic solutions at pH = 3–5 it does not change slowly up to 6 days [19]. Working solutions of tetracycline hydrochloride were acidified by adding 1 drop of hydrochloric acid to pH=5. ASTH with concentration of tetracycline hydrochloride $C = 1.1 \cdot 10^{-4}$ mol/l was used.



(a)



(b)

Fig. 3 Structural formula of tetracycline hydrochloride (a); absorption spectrum of an ASTH (b).

The absorption spectrum of tetracycline hydrochloride was recorded on the same spectrophotometer only in the absorption mode (without an integrating sphere).

The absorption spectrum of tetracycline hydrochloride has the form shown in Fig. 3(b). It has characteristic maxima in the ultraviolet region of the spectrum at the corresponding wavelengths: 217 nm, 257 nm, 376 nm.

The determination of the diffusion coefficient of tetracycline hydrochloride in biological tissue is based on measuring the kinetics of the optical diffuse reflectance spectra (DRS). For these measurements, each sample of dentin was fixed using a double-sided tape in a special clip in the form of a frame with a window of 0.5×0.5 cm, pressed against the wall of the quartz cuvette at the beam entrance to the spectrophotometer, so that there was free space between the surface of the sample and the cuvette wall filled with an aqueous solution of tetracycline hydrochloride (ASTH). Before measurements, the cuvette was filled with saline to wet the test sample (i.e., simulate the physiological state of the dentin). After 5 min, saline was removed using a syringe, after which the cuvette was filled with ASTH and measurements were performed during 200 min until saturated of the temporal dependence due to completion of the ASTH diffusion process (Fig. 4). The process of ASTH transport in a sample can be described in terms of the model of free diffusion [20].

3 Calculations

Geometrically, a sample of tissue can be represented as a plane-parallel plate of a finite thickness. It is also necessary to take into account some of the limitations inherent for the free diffusion model:

1) at the beginning of the experiment, we assume that the ASTH is absent at all points of the sample;

2) the volume of the ASTH is significantly larger than the volume of the dentin sample;

3) only concentration diffusion occurs;

4) we assume that the diffusion coefficient is constant at all points inside the studied dentin sample.

Using the second Fick law and performing transformations based on the use of the modified Bouguer-Lambert-Beer law, described in detail in Ref. [21], we obtain an expression for the difference between the effective optical density at the current time $A(t, \lambda)$ and at the initial time $A(t = 0, \lambda)$

$$\begin{aligned} &\Delta A(t,\lambda) = A(t,\lambda) - A(t=0,\lambda) = \\ &= \Delta\mu_{eff}(t,\lambda)L \sim C_0\left\{1-\exp\left(-\frac{\pi^2 Dt}{4l^2}\right)\right\}L, \\ &I = I_0 \exp\left[-\mu_{eff}L\right], \\ &\mu_{eff}(t,\lambda) = \sqrt{3\mu_a(\mu_a+\mu'_s)} \rightarrow \Delta\mu_{eff}(t,\lambda), \end{aligned} \quad (1)$$

where the effective optical density is determined from the measurements of DRS.

$$A = -\log R_d, \quad (2)$$

t is the time in sec during which the diffusion occurs, λ is the wavelength in nm, $\Delta\mu_{eff}$ (t, λ) is the difference between the effective coefficient of attenuation of light in biological tissue at the current time and at the initial time, 1/cm; L is the average path length of photons, which in the backscattering mode is $L \cong 2l_d$, $l_d^{-1} = \mu_{eff}$, $\mu'_s = \mu_s(1 - g)$, cm^{-1}, g is the scattering anisotropy factor (varies from 0 to 1, for dentin, $g \cong 0.93$) [18]; and for transmission $L \cong l$, l is the thickness of the sample, cm; D is the diffusion coefficient of the tetracycline hydrochloride molecules, cm^2/s; C_0 is the initial concentration of the tetracycline hydrochloride, mol/l.

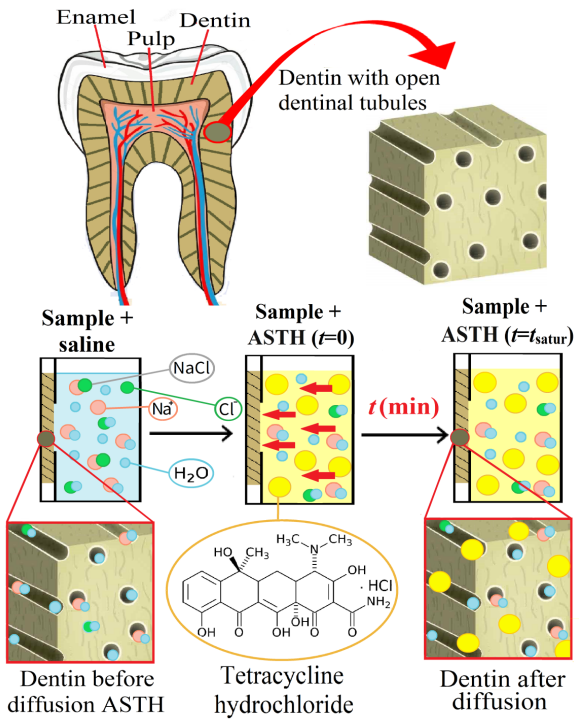


Fig. 4 Dentin samples during impregnation with an aqueous solution of tetracycline hydrochloride (ASTH).

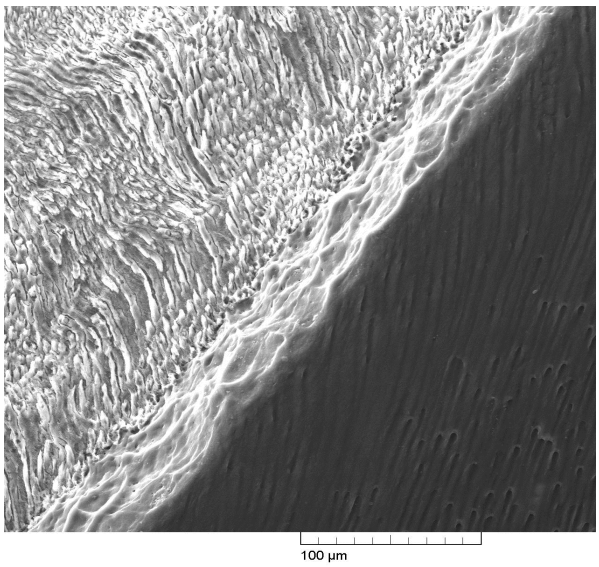
The recorded DRS ($R(\lambda)$, %) were converted using the standard Kubelka-Munk algorithm to extinction spectra $A(\lambda)$ using Shimadzu UV-2550 spectrophotometer software. An analysis of the kinetics of the difference in effective optical attenuation (ΔA) using Eq. (1) and taking into account the coefficients of approximation of experimental data made it possible to calculate the diffusion coefficient of the tetracycline hydrochloride (D).

4 Results and Discussion

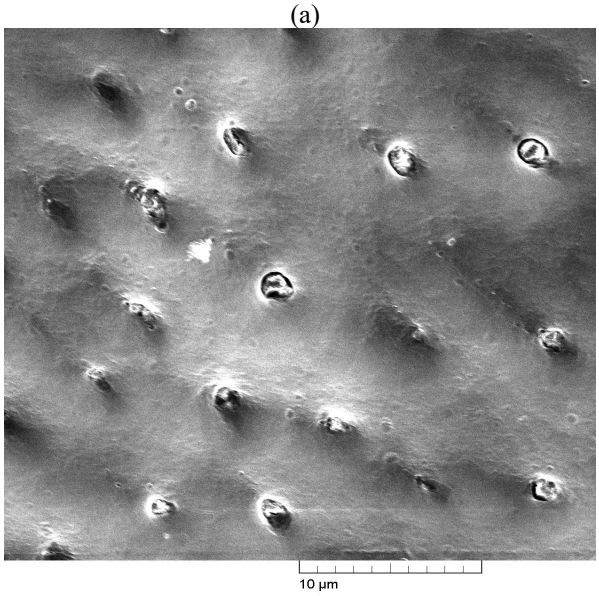
4.1 Structure of Human Dentin

The crown of a human tooth is covered with enamel, the hardest tissue in the tooth (Fig. 5(a)). Dentin is the main mass inside the tooth, has a light yellow color and some elasticity; it is stronger than bone and cement, but 4–5 times softer than enamel. It consists of an intercellular substance penetrated by dentinal tubules (tubules), which determine its trophism (Fig. 5(b)) and which make a significant contribution to the diffusion of substances inside the tooth.

Using scanning electron microscopy (SEM), the number of dentinal tubules in the studied samples (n=3) was determined, which amounted to (20550 ± 800) units per mm^2. They have an inner diameter of 0.5 to 4 µm, depending on the area of the tooth. The average number of dentinal tubules per unit volume (density) in the middle part of the root dentin is significantly lower than in the middle part of the crown dentin. The density of tubules in the dentin located closer to the outer part of the tooth also differs significantly from the density located near the occlusal fissure. It has been noted that with a low density of dentinal tubules, they have a more branched structure. The size of the branches of the dentinal tubules differs depending on the location: the branches of the dentinal tubules located along the periphery have a diameter of 0.5–1 µm [22, 23].



(a)

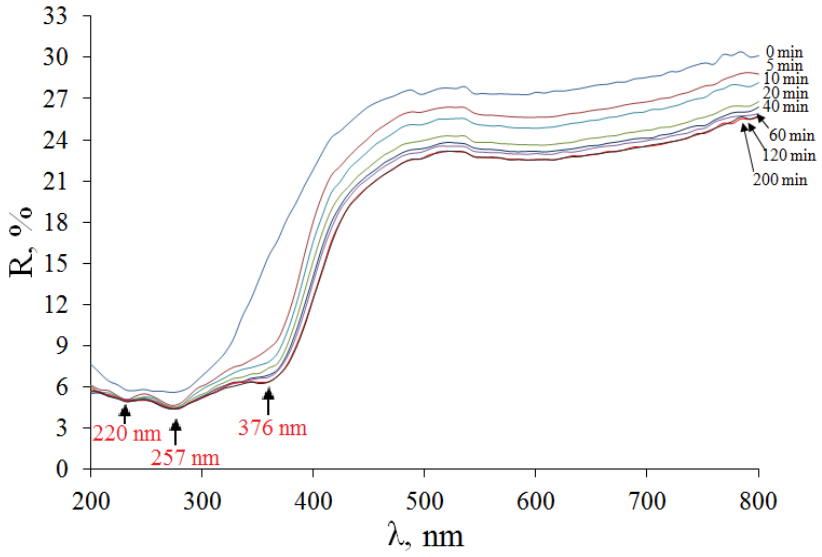


(b)

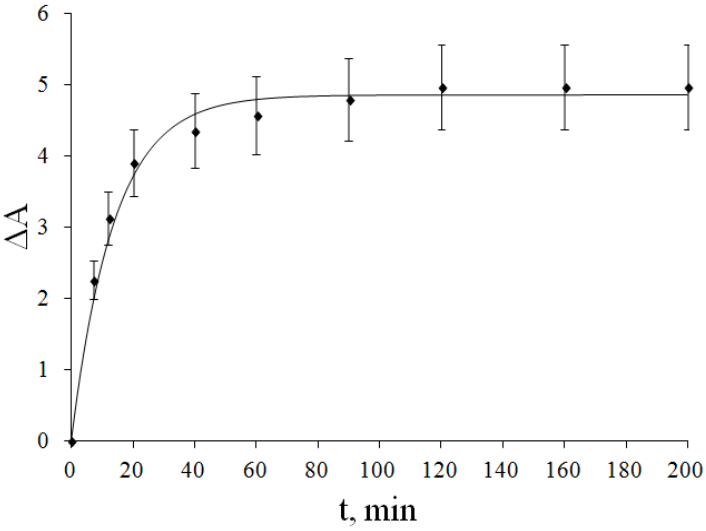
Fig. 5 Electronic micrographs (SEM) of a longitudinal cut (sample) of a human tooth: dentin-enamel junction (magnification 1k) (a); part of the saw cut of the crown (middle) (magnification 10k) (b).

4.2 Results of Spectrophotometric Analysis

DRS in the initial time has a characteristic appearance for dentin. By penetrating into dentin, ASTH changes the shape of the reflection spectra of dentin samples, which manifests itself in the form of characteristic absorption bands of tetracycline on the diffuse reflectance spectrum of dentin (Fig. 6(a)).



(a)



(b)

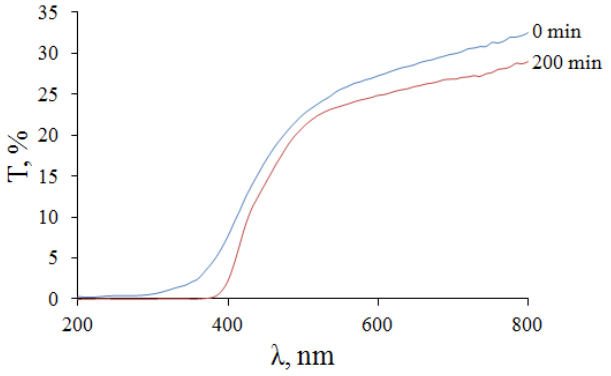
Fig. 6 Measured DRS of the dentin sample during its impregnation with the ASTH (a); kinetics of differential effective optical attenuation at λ = 376 nm calculated from experimental spectra using equations (1) and (2).

As the dentin saturated with ASTH, the diffuse reflectance decreases over the entire studied range, but most significantly from 320 to 800 nm, with a dip at 376 nm, which corresponds to one of the peaks of tetracycline hydrochloride. For the dentinal sample, the DRS of which is shown in Fig. 6(a), saturation occurred after 120 min of ASTH application, while the peaks did not shift and remained at their characteristic wavelengths. Fig. 6(b) shows a typical kinetic curve for the change in ΔA at 376 nm of the dentin sample during its impregnation with ASTH.

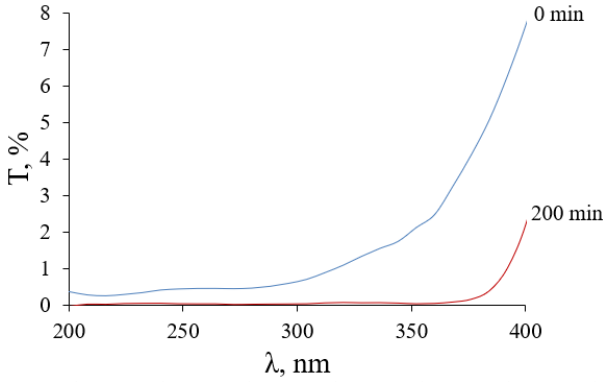
Diffusion coefficient of tetracycline hydrochloride was calculated using Eq. (1) and the least squares method. Calculations for each dentin sample were performed for five wavelengths in the spectral region of 360–400 nm, corresponding to the maximum absorption peak of tetracycline hydrochloride, and the obtained values were averaged. On average, the diffusion coefficient for the tetracycline hydrochloride is $D = (0.99 \pm 0.23)\cdot10^{-6}$ cm^2/s. The diffusion coefficient of an antiseptic solution of acridine dye (Rivanol) was measured as $(2.27 \pm 0.32)\cdot10^{-6}$ cm^2/s [24]. Also, the data obtained are consistent with the diffusion coefficient of methylene blue in the dentin of a human tooth, which turned out to be $(5.29 \pm 1.33)\cdot10^{-6}$ cm^2/s [25].

The permeability coefficient for 10% H_2O_2 in dentin was obtained as $7.2\cdot10^{-6}$ cm/s [26]. Using the relationship $P = D / l$ [21] and thickness of the studied dentinal samples $l = 0.5$, we get $D = 3.6\cdot10^{-7}$ cm^2/s. The diffusion coefficient of 40% glucose solution in dentin was found as $(5.4 \pm 0.8)\cdot10^{-6}$ cm^2/s [27]. The value of the diffusion coefficient is consistent with the data presented in the

work [28], where the diffusion coefficient in dentin was $0.27 \cdot 10^{-6}$ cm^2/s for water and $1.20 \cdot 10^{-6}$ cm^2/s for 40%-aqueous solution of glycerol. The scatter in the values of diffusion coefficients can be caused by a difference from sample to sample in the number density of dentinal tubules, surrounded by peritubular dentin, which is made from denser material, than the intertubular dentin, located between the tubules. In mature teeth, on transverse sections of dentinal tubules, peritubular dentin can be traced from the predentin to the dentin–enamel junction and occupies up to 60% of the area near the predentin–dentin junction, and about 2.5% at the dentin–enamel junction [29]. The number of dentinal tubules counted using SEM images in the studied cuts spreads from 6790 to 35076 per unit area 1/mm^2 with an average diameter from 1.98 ± 0.34 to 3.86 ± 1.02 μm [24].



(a)



(b)

Fig. 7 Full transmission spectra of human dentin samples during diffusion of an aqueous solution of tetracycline in the wavelength range from 200 to 800 nm (a), from 200 to 400 nm (b).

The obtained variability of diffusion coefficients in the range 10^{-6}–10^{-7} cm^2/s is well fit to variability of dentinal structures, this range is also typical for diffusion of studied molecules in other biological materials [30].

The total diffusion time τ of the tetracycline hydrochloride through entire dentin of thickness $l = 0.21 \pm 0.04$ cm (see Fig. 1b) can be calculated from experimental data for the diffusion coefficient $D = (0.99 \pm 0.23) \cdot 10^{-6}$ cm^2/s using equation valid for the one-side diffusion [31] as:

$$\tau = \left(4 / \pi^2\right)\left(l^2 / D\right) = (4.97 \pm 0.42) \text{ h}. \qquad (3)$$

The full transmission spectra of human dentin samples at the initial time and during vapor liquid diffusion are shown in Fig. 7 (a, b).

It can be seen that they correlate with the diffuse reflectance spectra over the entire wavelength range, since determined mainly by scattering on hydroxyapatite and collagen fibers. After the complete diffusion of the antibiotic in the dentin of the human tooth, the shape of the total transmission spectra of the dentin changes, the total transmittance does not significantly, but decreases over the entire wavelength range, which indicates an increase in the absorption of the sample (optically turbid medium – dentin).



(a)



(b)

Fig. 8 Clinical cases of discoloration of teeth "tetracycline teeth" as result of the use of tetracycline antibiotics at an early age: man, 59 years old – oral tetracycline up to the age of 12 years, several courses (a); women, 28 years old – use of oral doxycycline at the age of 15 years, several courses.

4.3 Clinical Example of Tetracycline Teeth

"Tetracycline teeth" are found in people who have taken tetracycline antibiotics. The discoloration may affect the entire tooth, it may be gray, or there may be spots in the

form of horizontal stripes (e.g., streaks) that range from light yellow/gray to dark brown (Fig. 8 (a, b)).

These teeth photos show that tetracycline reaches dentin through pulp and strongly stains the tooth with regular use.

5 Conclusions

Our study is devoted to determination of the rate of diffusion of tetracycline from blood plasma through pulp to dentin. Diffuse reflectance spectroscopy using an integrating sphere was used to determine the diffusion coefficient of an aqueous solution of an antibiotic, tetracycline, into the dentin of a human tooth. The studies were carried out in the wavelength range from 200 to 800 nm. When calculating this kinetic parameter, the model of free diffusion was used. The study revealed that after complete saturation of the sample with an antibiotic, the total transmission coefficient of dentin decreases over the entire studied wavelength range. According to the well-known tetracycline pharmacokinetics after oral administration, tetracycline enters the tooth pulp after 2–3 hours. We determined that for about 4.97 ± 0.42 hours the entire dentin will be stained. The data obtained must be taken into account for the preparation of clinical protocols.

Disclosures

The authors declare that they have no conflict of interest.

Acknowledgments

The research was carried out with financial support of the Russian Science Foundation grant No. 22-23-00420, https://rscf.ru/project/22-23-00420/.

References

1. R. A. Harvery, P. C. Champe (eds.), Lippincott's Illustrated Reviews: Pharmacology, 4th ed., Lippincott, Williams & Wilkins (2009). ISBN: 978-0-781-77155-9.
2. "Tetracycline". The American Society of Health-System Pharmacists. Archived from the original on 28 December 2016 (accessed 12.04.2022). [https://www.ashp.org/Search#q=Tetracycline&firstQueryCause=searchFromLink].
3. J. Enabulele, N. M. Chukwumah, and O. Enabulele, "Tetracycline use in children and knowledge of its oral implications among nursing mothers," Pediatric Dental Journal 30(3), 224–230 (2020).
4. V. Madhu, R. Rajesh, K. K. R. Ealla, S. R. Velidandla, and S. Santoshi, "Tetracycline-Induced Discoloration of Deciduous Teeth: Case Series," Journal of International Oral Health 6(3), 115–119 (2014).
5. I. S. Wallman, H. B. Hilton, "Teeth pigmented by tetracycline," Lancet 279(7234), 827–829 (1962).
6. A. Kadam, M. Ganachari, K. B. Mahendra, and S. Gurunath, "Drug Induced Tooth Discolouration," The Internet Journal of Dental Science 7(2), 10979 (2008).
7. A. R. Sanchez, R. S. Rogers, and P. J. Sheridan, "Tetracycline and other tetracycline-derivative staining of the teeth and oral cavity," International Journal of Dermatology 43, 709–715 (2004).
8. H. U. Luder, L. Antonini, "Discoloration of teeth from tetracyclines - Even today?" Schweizer Monatsschrift für Zahnmedizin SMfZ 121(5), 414–431 (2011).
9. Z. Zhu, Q. Yu, G. Qi, J. Yang, Y. Ni, W. Ruan, and L. Fang, "Tigecycline-Induced Tooth Discoloration in Children Younger than Eight Years, " Antimicrob Agents Chemother 65(9), e0085421 (2021).
10. M. L. Good, D. L. Hussey, "Minocycline: stained devil?" British Journal of Dermatology 149(2), 237–239 (2003).
11. E. Bouderlique, L. Nollet, E. Letavernier, and O. M. Vanakker, "Minocycline Counteracts Ectopic Calcification in a Murine Model of Pseudoxanthoma Elasticum: A Proof-of-Concept Study," International Journal of Molecular Sciences 23(3), 1838–1843 (2022).
12. W. Qin, Q-Q. Wan, Y-X Ma, and C-Y Wang, "Manifestation and Mechanisms of Abnormal Mineralization in Teeth," ACS Biomaterials Science and Engineering (2021).
13. M. S. Thomas, C. Denny, "Medication-Related Tooth Discoloration: A Review," Clinical Dentistry 41(5), 440–445 (2014).
14. S. Tsubura, "Clinical evaluation of three months' nightguard vital bleaching on tetracycline-stained teeth using Polanight 10% carbamide gel: 2-year follow-up study," Odontology 98(2), 134–138 (2010).
15. A. Faheem, "Tetracycline: Classification, Structure Activity Relationship and Mechanism of Action as a Theranostic Agent for Infectious Lesions-A Mini Review," Biomedical Journal of Scientific & Technical Research 7(2), 001475 (2018).
16. Y. He, Y.-Y. Huang, L. Xi, J. A. Gelfand, and M. R. Hamblin, "Tetracyclines function as dual-action light-activated antibiotics, " PLoS ONE 13(5), e0196485 (2018).
17. A. V. Belikov, S. N. Smirnov, and A. D. Tavalinskaya, "Laser Delivery and Spectral Study of a Chlorine-Containing Drug for the Treatment of Onychomycosis at Sequential Laser (lambda=2810 nm) and Photodynamic (lambda=656 +/- 10 nm) Impact, " Optics and Spectroscopy 129(7), 754–762 (2021).
18. K. N. Agwuh, A. MacGowan, "Pharmacokinetics and pharmacodynamics of the tetracyclines including glycylcyclines," Journal of Antimicrobial Chemotherapy 58(2), 256–265 (2006).

19. A. Schuster, H. Shwachman, "The tetracyclines: applied pharmacology," Pediatric Clinics of North America 3(2), 295–303 (1956).
20. E. A. Genina, A. N. Bashkatov, E. E. Chikina, A. B. Knyazev, O. V. Mareev, and V. V. Tuchin, "Methylene Blue mediated laser therapy of maxillary sinusitis," Laser Physics 16(7), 1128–1133 (2006).
21. V. V. Tuchin (Ed.), Handbook of Optical Biomedical Diagnostics, Vol. 1: Light-Tissue Interaction, 2nd ed., SPIE Press, Bellingham, WA (2016). ISBN: 978-1-628-41909-2.
22. A. V. Belikov, F. I. Feldchtein, and G. B. Altshuler, "Laser Ablation of Hard Tissues," in Handbook of Biophotonics. Vol. 2: Photonics for Health Care, 1st ed., J. Popp, V. V. Tuchin, A. Chiou, and S. Heinemann (Eds.), Wiley-VCH Verlag GmbH, 1095–1110 (2012). ISBN: 978-3-527-41048-4.
23. A. V. Belikov, G. B. Altshuler, K. V. Shatilova, V. V. Tuchin, A. V. Skrypnik, F. I. Feldchtein, A. E. Pushkareva, and I. Cernavin, "Peroxide dental bleaching via laser microchannels and tooth color measurements," Journal of Biomedical Optics 21(12), 125001 (2016).
24. A. A. Selifonov, V. V. Tuchin, "Optical clearing and molecular diffusivity of hard and soft oral tissues," Chapter 36 in Handbook of Tissue Optical Clearing: New Prospects in Optical Imaging, V. V. Tuchin, Z. Dan, and E. A. Genina (Eds.), Boca Raton, CRC Press, 629–646 (2022). ISBN 978-0-367-89509-9.
25. A. A. Selifonov, O. G. Shapoval, A. N. Mikerov, and V. V. Tuchin, "Determination of the diffusion coefficient of methylene blue solutions in dentin of a human tooth using reflectance spectroscopy and their antibacterial activity during laser exposure," Optics and Spectroscopy 126, 758–768 (2019).
26. C. T. Hanks, J. C. Fat, J. C. Wataha, and J. F. Corcoran, "Cytotoxicity and Dentin Permeability of Carbamide Peroxide and Hydrogen Peroxide Vital Bleaching Materials, in vitro, " Journal of Dental Research 72(5), 931–938 (1993).
27. A. A. Selifonov, V. V. Tuchin, "Optical properties of human dentin when it is immersed in glucose in vitro and the kinetics of this process," Journal of Optical Technology 87(3) 168–174 (2020).
28. N. A. Trunina, V. V. Lychagov, and V. V. Tuchin, "OCT monitoring of diffusion of water and glycerol through tooth dentine in different geometry of wetting, " Proceedings of SPIE 7563, 75630U (2010).
29. V. V. Tuchin, G. B. Altshuler, "Dental and oral tissue optics," Chapter 9 in Fundamentals and Applications of Biophotonics in Dentistry, Series on Biomaterials and Bioengineering, Imperial College Press, UK, 245–300 (2007).
30. A. Kotyk, K. Janacek, Cell Membrane Transport: An Interdisciplinary Approach, Plenum Press, New York (1977).
31. V. V . Tuchin, Tissue Optics: Light Scattering Methods and Instruments for Medical Diagnostics, 3rd ed., SPIE Press, Bellingham, WA (2015). ISBN: 978-1-628-41517-9.

Mapping Large Strains in Phase-Sensitive OCT: Key Role of Supra-Pixel Displacement Tracking in Incremental Strain Evaluation

Alexander A. Sovetsky, Alexander L. Matveyev, Lev A. Matveev, Grigory V. Gelikonov, and Vladimir Y. Zaitsev

Institute of Applied Physics Russian Academy of Sciences, 46 Ulyanova str., Nizhny Novgorod 603950, Russia

*** e-mail:** alex.sovetsky@mail.ru

Abstract. Displacement tracking is an important step in realization of compression optical coherence elastography (C-OCE), especially in the context of obtaining nonlinear stress-strain dependences and subsequent evaluation of the tissue Young's modulus. The rapidly progressing phase-sensitive C-OCE, however, enables direct measurements of only rather small interframe strains (below 1%), for which displacements are also small. Obtaining stress-strain curves for larger strains (~10% and greater) in phase-sensitive C-OCE can be made via cumulation of interframe strains and particle displacements. The resultant values of the so-found cumulative displacements may significantly exceed the pixel size, whereas measurements of the phase variations in C-OCE are usually performed by comparing the signals from the same pixel in a series of compared scans. When displacements of particles in a series of acquired scans reach supra-pixel values, simple pixel-to-pixel estimation of interframe phase variations may lead to significant errors in evaluating linear and nonlinear elastic properties of tissues. Thus, for large strains, adequate accounting for the resultant supra-pixel displacements of order of several pixels and greater is of key importance for undistorted mapping of elastic properties of heterogeneous materials, as well as for correct tracking of boundaries separating tissue regions with different elastic properties. In this paper we discuss the elastographic procedures of correct tracking of supra-pixel displacements in phase-sensitive C-OCE and give real examples demonstrating the importance of such displacement tracking for undistorted reconstruction of two-dimensional maps of linear and nonlinear elastic properties of real biological tissues.
© 2022 Journal of Biomedical Photonics & Engineering.

Keywords: Optical coherence elastography; compression elastography; OCE; strain mapping; elasticity mapping.

Paper #3508 received 14 Jul 2022; revised manuscript received 15 Aug 2022; accepted for publication 21 Aug 2022; published online 22 Sep 2022. doi: 10.18287/JBPE22.08.030304.

1 Introduction

Visualization of deformations in optical coherence tomography has been attracting much attention since the seminal paper by J. Schmitt [1], in which of the idea of compression elastography [2] initially proposed in medical ultrasound was transferred to optical coherence elastography. As a result of intense effort of various groups working in Optical Coherence Elastography (OCE), a breakthrough in the development of OCT-based methods for mapping genuine local strains occurred in the recent ~5 years, so that practically operable realizations of OCT-based strain visualization, as well as stiffness mapping using the compression OCE principle were demonstrated [3–8]. Of key importance in realization of these methods was the development of the

phase-resolved approach to mapping axial strains. In particular, in Ref. [3] the least-square fitting for finding axial gradients of interframe phase variations was proposed with the additional amplitude weighting, due to which noisy contributions of small-amplitude pixels can be appreciably suppressed. Works [5, 6] proposed advanced variants of determining such gradients based on the vector approach (in which the complex-valued amplitudes are processed as vectors in the complex plane). The vector method also realizes amplitude weighting, obviates the necessity of conventionally required phase unwrapping for supra-wavelength displacements of scatterers and is especially tolerant to various measurement errors (including both the noises of the receiving array and deformation-induced decorrelation of the compared OCT scans). It should also be mentioned that in parallel with the above-mentioned approach to OCE realization, in which mapping local strains is of key importance, there is another approach, dynamic OCE methods which utilize measurements of elastic-wave velocities either for shear waves or surface waves (see, e.g. reviews [9, 10]). However, wave-induced perturbations usually have fairly small amplitude with essentially sub-pixel displacements and, furthermore, estimation of local strains is not required for their tracking. In view of this, the problem of mapping large strains and supra-pixel (of the order of several pixels and greater) displacements does not arise in dynamic OCE methods, but is important for compression OCE, in which, besides small-amplitude perturbations, nonlinearity of stress-strain dependences can be studied and the tissue strains may reach tens of percent [11]. It may also be noted that although the use of phase-sensitive OCT for mapping strains was proposed over 15 years ago [12, 13] in this study for estimating strains and presenting the corresponding experimental demonstrations we will use the vector method in form [6] for analyzing phase-sensitive OCT signals.

Like for other applications of phase variations (e.g. in the estimation of the Doppler phase shift) in what follows the discussion will be focused on the estimation of axial displacements u and axial strains $s = \partial u / \partial z$ related to the interframe variation Φ of the OCT signal as follows:

$$s = \frac{\lambda_0}{4\pi n} \frac{\partial \Phi}{\partial z}, \qquad (1)$$

where λ_0 is the central optical wavelength in vacuum and n is the refractive index.

For the straightforward comparison of phases in sequentially acquired phase-sensitive OCT scans, the maximal magnitudes of estimated strains and displacements are limited by decorrelation effects caused by both relative interframe displacements of scatterers and their displacements from one pixel of the reference OCT scan to a neighboring pixel in the other scan. For such supra-pixel interframe displacements direct pixel-to-pixel comparison of the current and initial phases leads to serious errors because for such strong displacements, the initial and current signal in the considered pixel is formed by essentially different scatterers that were initially located in neighboring pixels [4, 5]. However, if the interframe phase variation in the strained tissue does not yet experience phase wrapping within the vertical size of individual pixels, to a certain degree the decorrelation caused by vertical displacements of scatterers between the neighboring pixels can be compensated. This can be made by comparing phases of pixels with neighboring numbers in the compared scans instead of straightforward pixel-to-pixel comparison [4, 5]. In practice such compensation is fairly efficient for displacements about one pixel, but does not help much to improve the quality of phase-variation estimates if the interframe displacements are greater than one pixel. For "typical" OCT systems, the maximal interframe strains that can be directly estimated via pair-wise comparison of OCT scans roughly amount to ~1% [5].

However, larger strains that cause essentially supra-pixel displacements are also of great interest for various applications (e.g., for studying thermo-mechanical deformations, drying, osmotic deformations [14–19]), as well as for studying stress-strain dependences beyond the linear Hooke's law. The latter, for many tissues, may be essentially violated for strains on the order of several tens of percent [8, 20–22].

In such situations, even if estimation of fairly large deformations via direct pair-wise comparison of OCT scans is impossible, incremental approach can be applied by performing cumulation of smaller directly measurable strains for a sequence of OCT scans [23, 24]. This incremental approach makes it possible to quantify much larger deformations resulting in strains up to several tens of percent and multiple-pixel displacements.

Unlike small strains under such conditions even the notion of "correct" cumulative strain becomes dependent on the particular application of the estimated large deformations, so that different definitions of cumulative strain may be required for various tasks, for which procedures of estimating large cumulative strains also may require modifications. Indeed, different methods that are (nearly) equivalent for finding small strains may give strongly differing results for large cumulative strains and in some cases the inappropriately chosen method of finding cumulative strains may result in strongly erroneous conclusions.

In what follows we analyze the notion of cumulative strains and displacements, demonstrate situations in which one or another definition should be chosen, and formulate algorithms that give physically meaningful cumulative results depending on the particular task. In particular, we discuss correct finding of supra-pixel displacements including tracking of boundaries that are not contrasted in structural OCT scans, quantification of large strains, as well as quantification and visualization of elastic properties of elastically-nonlinear tissues, for which their stiffness pronouncedly depends of strain and stress, correct visualization of tissue nonlinearity and related issues. For experimental illustrations we will use OCT scans obtained with OCT systems operating at a

wavelength of 1300 nm (and spectral width 90–100 nm) similar to those used in previous works [22, 25, 26].

2 When displacement tracking is important for finding cumulative strains

The purpose of this section is to demonstrate that even if one is not interested in the displacements of the scattering particles themselves, but wants to estimate fairly large strains of the tissue, correct finding of these strains in most cases cannot be made without auxiliary estimation of displacements experienced by the scatterers. This is a fairly general statement except for a special case of spatially uniform strain distribution. Such a simple situation occurs when mechanically homogeneous tissue experiences spatially uniform uniaxial stress. In such a case the resultant strain is also spatially uniform. In practice uniaxial stress can be created in the vicinity of an output window of the OCT probe that compresses the tissue. It is assumed that the tissue is not confined in the lateral directions and can fairly freely expand laterally (this also implies that there is no appreciable stiction at the interface between the OCT probe and the tissue, which may be enabled by putting a lubricating liquid onto the tissue surface).

A corresponding real example is shown in Fig. 1 that demonstrates compression of a layer of homogeneous silicone compressed by the output OCT probe window under the control of an automated moving support enabling a constant compression rate. Fig. 1a shows a structural image in which the two rectangles 1 and 2 are located at different depths and show the initial positions of two processing windows over which the axial phase gradients $\partial\Phi/\partial z$ are estimated (and, therefore, strains can be found using Eq. (1)). Fig. 1b shows an example of the spatial distribution of the compression-produced interframe strain which, as expected, looks fairly uniform. The two rectangles 1’ and 2’ show slightly displaced positions of the scatterers initially located within windows 1 and 2. For the deeper rectangles 2 and 2’ the displacements are somewhat greater than for rectangles 1 and 1’. However, for small interframe displacements in Fig. 1b, it makes no sense to distinguish window 1 from 1’ and even the stronger displaced windows 2 from 2’. Fig. 1c shows the distribution of cumulative strain found via straightforward summation of interframe strains (for ~150 frames). The total variation in the silicone-layer thickness is over 30%, so that during the compression, the scatterers are gradually displaced outside the initial locations of the processing windows and are substituted by other scatterers. The position of particles initially located within window 1 by the end of compression shifts to position 1’ (so that still window 1 and 1’ are significantly overlapped), whereas window 2 shifts to the strongly displaced position labeled as 2’, so that window 2 and 2’ do not overlap at all and contain different portions of particles. However, since the “instantaneous” interframe strain is spatially uniform, for estimating strains, it makes no sense to track the actual positions of the same physical particles, so that processing windows with fixed coordinates enable correct estimation of strains. This statement is illustrated by the strain dependences shown in Fig. 1d obtained for the processing window 1, as well as for window 2 with the fixed position and gradually displaced window 2’. The procedure of tracking the gradual displacements of the particles is explained below in detail, however, Fig. 1 shows that, for the uniform silicone, such tracking does not affect the estimated cumulative strain. The cumulative strain in Fig. 1d for all three curves is found using straightforward summation of incremental interframe strains. In Section 3 another form of cumulative strain is discussed, but for illustration of the absence of changes in the result with/without window tracking in Fig. 1 the used straightforward summation is enough.

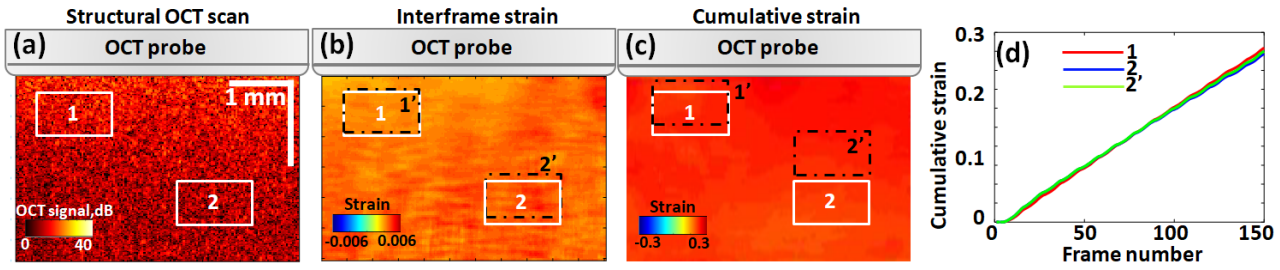


Fig. 1 Elucidation that in a homogeneous material correct strain can be found even without any displacement tracking. Panel (a) is a structural OCT scan of the compressed homogeneous silicone layer in which windows 1 and 2 with different vertical (lateral) coordinates are shown in the beginning of compression. Panel (b) shows the spatial distribution of interframe strain which is rather uniform over the entire visualized region (for the small interframe strains, the difference between initial posisions 1 and 2 and displaced positions 1’ and 2’ is insignificant). Panel (c) shows the much larger cumulative strain found by straightforward summation of interframe strains (notice than the deeper window 2 in the displaced position 2’ does not overlap with the initial position). Panel (d) shows the cumulative strain as a function of frame number found using the processing windows 1, 2 (without tracking) and 2’ with gradual tracking; all three curves are nearly indistinguishable even if for window 2’ the initial particles were substituted by new portions of the material.

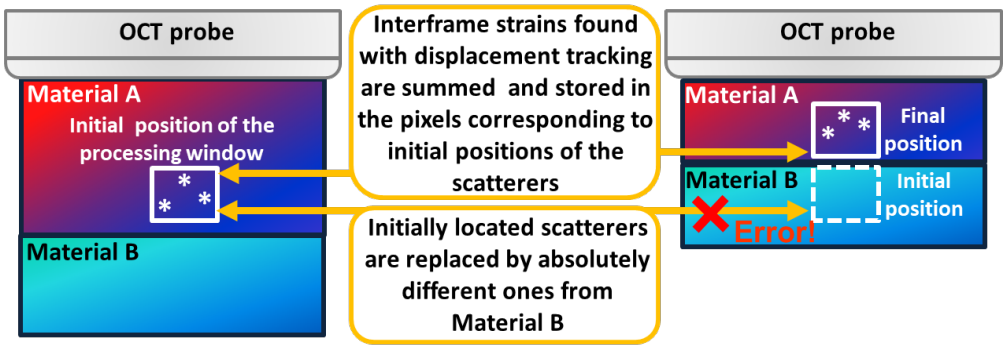


Fig. 2 The scheme explaining the importance of displacement tracking and the fallacy of finding local material strain in initial position of the processing window during the significant compression. It is clear that in the beginning of compression the window shown by the solid line contains a portion of Material A and by the end of compression it already contains only particles of Material B with a larger Young's modulus. Therefore, to correctly estimate strain for the portion of Material A (shown by asterisks) during the compression, one has to track the changed positions of this material portion and correspondingly shift the position of the window, over which the strain is found.

In contrast to the homogeneous sample shown in Fig. 1, usually real tissues are mechanically inhomogeneous. Consequently, during the material deformation, the same position of the processing window may correspond to different portions of the inhomogeneous material with potentially significantly different elastic properties and different deformability. It is known that deformability (stiffness) of different portions of inhomogeneous tissues may differ quite strongly (several times and greater, e.g. for cancerous and normal tissues [25–28]). Consequently, for a fixed coordinate, during deformation of heterogeneous tissues one tissue component can be substituted by the tissue portions with strongly different elastic properties. In view of this, to find the resultant (cumulative) strain for a particular portion of the tissue, the processing window should be gradually shifted to follow the displacement of a particular tissue portion. The necessity to track the displacement of the particles and correspondingly move the processing window for mechanically inhomogeneous samples, as well as the reason of possible errors when the particle tracking is not used, are schematically elucidated in Fig. 2.

The discussed displacement tracking is equivalent to continuous estimation of the thickness of the material layer separating the OCT window surface and the current position of the tissue portion that we aim to keep within the processing window. This tracking method should be operable for any point of the material even in the absence of any visible markers associated with the initial particular position of the window. Furthermore, for a mechanically inhomogeneous material, within the layer separating the OCT probe and the current position of the processing window, the strain distribution may be essentially non-uniform in space. To correctly estimate local strains for every tissue portion that gradually moves, one should synchronously move the processing window. In other words, one should know the current distance of each material portion from the OCT probe surface. In turn, in the absence of any trackable markers, to calculate the current distance for every tissue portion, one has to correctly estimate strain of each portion of the tissue within the layer separating the OCT probe surface and the processing window. Therefore, the tracking of the processing window position should be performed in a self-consistent manner: correct estimation of strains requires knowing of the current position (cumulative displacement) of each moving tissue portion, whereas tracking of the position of each tissue portion in the absence of trackable markers requires correct estimation of cumulative strains for all over-laying layers of the material.

It should be pointed out that small interframe (incremental) strains are unambiguously related by Eq. (1) with the axial gradient of interframe phase variations. We refer the readers to papers [3, 5, 6], where the estimation of this gradient was discussed in ample detail. Finding total (cumulative) strains and total strain-induced displacement of the scatterers was used in some earlier papers, e.g. [14, 16, 23]. However, those papers discussed fairly homogeneous tissues and moderately large strains (usually essentially below 10%), for which tracking of a particular tissue portion was not very critical in contrast to strongly heterogeneous tissues (such as cancerous ones discussed in Ref. [22]), for which the procedures of correct particle tracking deserve a special detailed discussion.

We emphasize once again that only in special simplified cases (fairly uniform materials like in Fig. 1) large strains may be correctly evaluated independently of displacements. However, for most real mechanically inhomogeneous tissues, strain estimation performed without simultaneous tracking of displaced tissue portions with different elastic properties leads to strong errors. This in turn may significantly distort the diagnostic conclusions based on the OCT-elastography data.

Next, it can be pointed out that, unlike straightforward estimation of small strains via Eq. (1), the larger cumulative strain can be defined in different forms depending on the particular problem.

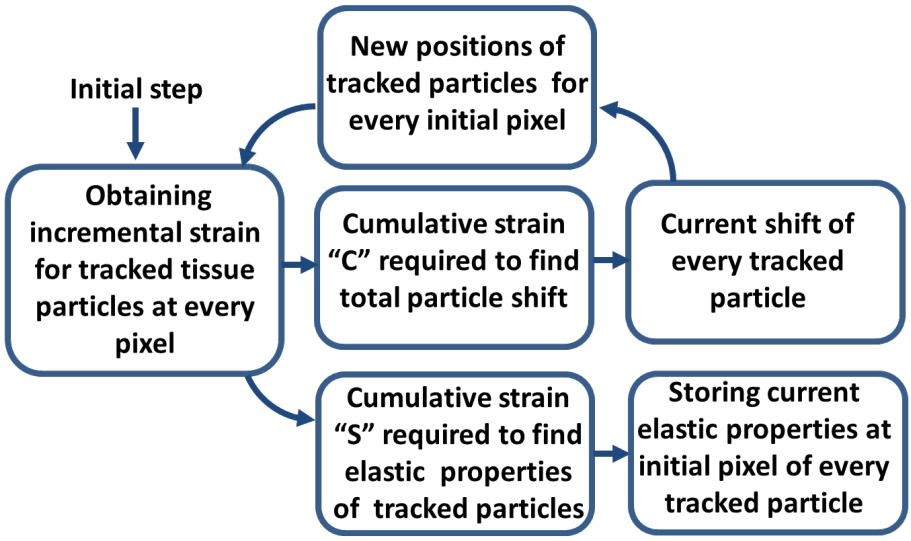


Fig. 3 Schematic of the self-consistent procedures of displacement tracking for correct evaluation of fairly large strains and accompanying variations in the elastic properties of the tissue. Namely, knowing the current distance between the OCT probe surface and every portions of the tissue is required to correctly evaluate strain of every tissue portion. In turn, knowing the current cumulative strains of all tissue portions is required to find the current position of every tissue particle (and to enable the corresponding shift of the processing window containing this tissue portion).

These definitions almost coincide for sufficiently small (say, ~ several %) strains, but significantly deviate for larger strains of the order of tens of percent. It can be shown that the "cumulative strain" destined for correct tracking of particle displacements the absence of evident markers (we denote this strain as "C") and cumulative strain intended for obtaining local "stress-strain" relationships and Young's modulus estimation (we denote it as "S") require different definitions.

In terms of notations "C" and "S" for the two definitions of cumulative strains the self-consistent procedures of strain estimation and displacement tracking are schematically depicted in Fig. 3.

In the following sections we explicitly give the definitions of cumulative strains "C" and "S", explain their inter-relations and present experimental examples to illustrate the importance of the self-consistent tracking of cumulative displacements and local strains of the displaced tissue particles.

3 How to relate interframe strains to cumulative strain that defines thickness variation

For non-infinitesimal deformation of inhomogeneous material, correct estimation of local strains requires that the processing window, over which the local strain is estimated, should contain the same portion of the material. To enable tracking of the same material portion, one has to estimate the current thickness of the material layer separating the OCT probe surface and the initial position of the processing window. Sufficiently small incremental displacements can be found via pixel-to-pixel comparison of the phase for a pair of sequential complex-valued OCT scans. Then the axial strain S defined by Eq. (1) can be found by estimating the axial gradient of this interframe phase variation (e.g., using the least-square approach [3] or vector method [6]). Let us consider a sufficiently thin (and therefore mechanically homogeneous) layer, for which the current thickness is h_{i-1} by the $(i-1)$ acquired frame. Then a small incremental strain s_i between i^{th} and $(i-1)^{\text{th}}$ frames causes the following small change in the layer thickness $h_i = h_{i-1}(1+s_i)$, so that the resultant thickness after a series of n incremental strains is

$$h_n = h_0 \prod_{i=1}^{n} (1+s_i), \tag{2}$$

where h_0 is the initial thickness. Assuming for simplicity that incremental strains are identical, $s_i = s$ one obtains

$$h_n = h_0(1+s)^n = h_0\left(1+ns+\frac{n(n-1)}{2!}s^2+ \right. \\ \left. +\frac{n(n-1)(n-2)}{3!}s^3+\ldots+s^n\right) \tag{3}$$

For sufficiently small term $ns \ll 1$ (in practice, on the order of a few percent), Eq. (3) reduces to

$$h_n \approx h_0(1+S), \tag{4}$$

where we denote $S = ns$. In the general case, when incremental strains s_i are not necessarily identical, the definition of cumulative strain S found via

straightforward summation of incremental strains can be generalized as

$$S = \sum_i s_i. \tag{5}$$

However, if the condition $S \ll 1$ is not satisfied, Eq. (4) for the current thickness gives an appreciable error. For the exact estimation of the thickness variation, another definition of cumulative strain may be formulated (we denote this quantity as C)

$$h = h_0(1+C), \text{ or } \Delta h \equiv h - h_0 = h_0 C. \tag{6}$$

From comparison of Eq. (6) and Eq. (3) it is clear that in the case of identical incremental strains s,

$$C_n = ns + \frac{n(n-1)}{2!}s^2 + \\ + \frac{n(n-1)(n-2)}{3!}s^3 + \ldots + s^n. \tag{7}$$

In more general situations, when incremental interframe strains s_i are not necessarily identical, a convenient recurrent definition of C_n can be formulated:

$$C_{n+1} = C_n + (C_n + 1)s_n. \tag{8}$$

It should be recalled that for a mechanically inhomogeneous sample, to find the variation in the thickness of the entire layer separating the OCT-probe window and the tracked portion of the material, one should take into account the inhomogeneity of overlaying material. Schematically this is shown in Fig. 4 for a 3-layer case. In the general case the inhomogeneity is *a priori* unknown, so that the cumulative strain should be found for every pixel above the considered pixel J, such that the variation $\Delta H_n(J)$ in the total thickens of the overlaying material after n incremental steps of straining is given by

$$\Delta H_n(J) = H_{px} \sum_{i=1}^{J} C_n(J), \tag{9}$$

where H_{px} is the vertical pixel size. The depth of each processing window centered around a given pixel should be shifted by one pixel every time when the so-found additional displacement ΔH of the tracked portion of the material increases by H_{px} as shown in Fig. 4.

In the conclusion of this section we note that one can obtain another useful relationship between the cumulative strain C defined via the non-infinitesimal change in the thickness of a considered material layer (Eqs. (6) and (8)) and strains S found via straightforward summation of incremental strains s_i (see Eq. (5)). Using Eq. (5) and recalling that an arbitrary S can be represented as a sum of a large number p of infinitesimal identical incremental strains ($S = p \cdot s$, $s \ll 1$), Eq. (3) can be rewritten as

$$h = h_0 \lim_{p\to\infty}(1+s)^p = \\ = h_0 \lim_{p\to\infty}\left(1+\frac{S}{p}\right)^p = h_0 \exp(S). \tag{10}$$

Comparison of Eq. (10) and Eq. (6) indicates that the cumulative strains C and S are related as

$$C = \exp(S) - 1 \text{ and } S = \ln(1+C). \tag{11}$$

For sufficiently small deformations (in practice, below ~10%) both definitions of cumulative strains are almost indistinguishable, $S \approx C$, whereas for several tens of percent, cumulative strains S and C differ rather

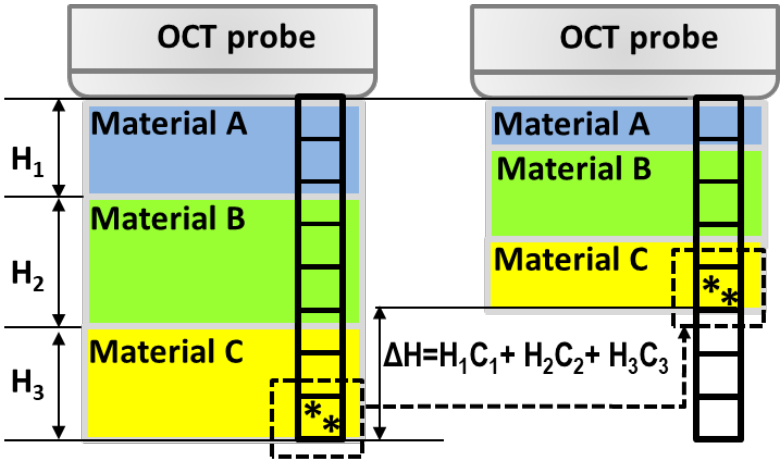


Fig. 4 Schematic of updating the processing window depth by estimating the deformation-produced displacement of tracked material portions.

significantly. Generally speaking, both strains S or C may be either positive or negative, their sign determines which one is greater in the absolute value. For compression (when S and C both are negative), $|C|<|S|$ and for expansion (when S and both are positive), $C > S$. As shown in what follows, the nonlinear relationship at Eq. (11) between S and C may be responsible for somewhat different conclusions about the material nonlinearity.

4 Usage of cumulative strains for obtaining nonlinear stress-strain relationships

In the optical coherence elastography based on the compression principle [1, 2] it was proposed to use the difference in strains of compressed layers for evaluation of differences in their Young's moduli. In the framework of the linear paradigm, for uniaxial stress σ created in the vicinity of the OCT probe that compresses the two layers of materials with the Young's moduli $E_{1,2}$, the resultant strains $s_{1,2} << 1$ produced by the same uniaxial strain σ are related via the linear Hooke's law:

$$\sigma = E_1 s_1 = E_2 s_2. \qquad (12)$$

For soft biological tissues, the linear approximation usually well holds for strains below 10^{-2}. In this case even if the applied stress is unknown, the relative value of the elastic moduli at different depths corresponds to the inverse ratio of the strains, $E_1 / E_2 = s_2 / s_1$. Thus, if for one layer its Young's modulus is known, the modulus for the second layer can readily be quantified. In practice, a layer of transparent or weakly scattering soft silicone with pre-calibrated Young's modulus can be placed over the examined tissue to enable quantification of its stiffness [7, 8] using the proportion (12).

The situation, however, is not that trivial if the created strains are not infinitesimal and, especially, if the constitutive equations $\sigma(s)$ relating strains in the material and the applied stress are nonlinear. In what follows we discuss how this nonlinearity can be characterized in a wide range of strains up to several tens of percent, for which the definition of what is "correct" strain is less evident.

For an optically transparent silicone layer (like used in Ref. [7]), it looks natural to define its finite axial strain s_{finit} via the variation of the layer thickness:

$$s_{finit} = (h - h_0) / h_0 = \Delta h / h_0. \qquad (13)$$

Such a definition indeed was used in the compression OCE variant described in paper [7], where the strain in the bulk of the transparent reference layer was not measurable and only the total layer thickness could be estimated by tracking its boundaries. In terms of the above-introduced cumulative strains C and strain S, it is clear from Eq. (13) that in Ref. [7] the strain of the reference silicone layer was actually understood as strain C defined by Eq. (6).

As was mentioned in the discussion of Eq. (11), for strains on the order of several percent there is almost no difference between the cumulative strain C describing the variations in material thickness and strain S defined as straightforward summation of incremental small strains. However, in quite realistic situations strains in either reference layer or the examined tissue may reach significantly larger values, on the order of several tens of percent. In such cases the following questions arise: (i) whether the reference silicone can still be considered as an elastically linear material for strains >20–30% and (ii) if a material behaves as linear-elastic one, which of the two types of cumulative strains C or S should be linearly proportional to the applied stress?

The above formulated questions can readily be verified experimentally since, for strains >20–30%, the quantities C and S should differ rather pronouncedly according to their nonlinear inter-relationship (12). If one assumes that the stress-strain relationship (12) should hold for the strain defined via Eq. (6) (i.e., via the layer-thickness variation as in paper [7]), then the following relationship should be expected

$$\sigma = EC = E \cdot (\Delta h / h_0), \qquad (14)$$

which can be verified experimentally.

Another understanding of the material linearity implies that the linear proportionality (12) holds for small increments in stress and strain, $\Delta\sigma = E\Delta s$ with invariable proportionality coefficient E in a fairly broad total strain range. Then it should be expected that the same proportionality holds for cumulative strain S defined via Eq. (5):

$$\sigma = ES. \qquad (15)$$

Which of Eqs. (14) or (15) is closer to reality can be verified experimentally. Furthermore, this verification can be performed even without the necessity of independent measurement of stresses/forces by auxiliary force cells. Such a "self-calibration" test requires measurements of only local strains. Namely, one may perform compression of a sandwich structure made of two silicone layers with sufficiently strongly (say 5–10 times) differing elastic moduli as illustrated in Fig. 5a. For such silicones that are strongly-contrasted in stiffness, the strains under compression are also strongly different, so that for the softer silicone, its strain may reach values of several tens of percent, whereas for the stiffer silicone, the strain may remain sufficiently small $S, C << 1$ (say within a few percent). For such small strains, the two definitions of cumulative strains practically do not differ, $S \approx C$, and one should expect the small strain developed in the stiffer are proportional to the applied stress with a high accuracy (although the proportionality coefficient may remain unknown). This value proportional to stress can be plotted against the

larger strains, either C or S, of the softer silicone layer. In such a way it is possible to verify which of the assumed forms of the Hooke's law (Eq. (14) for C or Eq. (15) for S) is closer to a linear dependence in a wide range of strains.

The results of such experimental verification are shown in Fig. 5b for two pair of silicones with the approximate proportions of the elastic moduli 550 kPa / 40 kPa and 550 kPa / 100 kPa. We emphasize, that precise values of the Young's moduli are not required for the verification of linearity. Fig. 5 demonstrates that the appreciable difference between the cumulative strains C or S become noticeable for strains > 0.2. The main conclusion is that it is strain S found via straightforward summation of incremental interframe strains, for which the proportionality between the small strain in the stiffer silicone (vertical axis) and larger strain S of the softer silicone (horizontal axis) remains nearly perfectly linear up to strains ~0.4–0.5. In contrast, for cumulative strains C the dependence is pronouncedly nonlinear starting from values ~0.2.

It is also interesting to mention that the stress-strain data presented in paper [7] demonstrate pronounced nonlinearity of the relationship between independently measured stress and strain C defined via variations in the silicone-layer thickness (see Eq. (14)). However, using the relation (11) between C and S, one can easily replot these data from [7] in the form $\sigma = \sigma(S)$. The two curves in the replotted form and original one from [7] are shown in Fig. 5c. It is clear that in the replotted form $\sigma = \sigma(S)$ data [7] look as a fairly linear dependence up to strains $S \sim 0.4 - 0.5$ similarly to the nearly-linear dependences shown in Fig. 5b for the same strain range.

For even larger strains, the additional stiffening of silicones becomes noticeable. It is likely, however, that this stiffening is mostly caused by adhesion/stiction effects. Indeed, the elastic response of a material is determined by the Young's modulus only for true uniaxial loading when the material is not confined in the lateral direction and can freely expand laterally. Stiction to either OCT probe glass or to the rigid bottom surface (or both) may significantly impede the lateral expansion, such that the material begins to experience some contribution of volumetric ("all-round") compression, the reaction to which is determined by the bulk modulus K rather than the Young's modulus $E<<K$. For biological tissues and similar materials (like soft silicones), this difference may reach 5–6 orders of magnitude, such that even incomplete stiction may cause noticeable coupling with the bulk compression, which may result in quite a significant difference between the true Young's modulus and its apparent higher value distorted by insufficiently free lateral expansion of the material due to stiction to the contacting rigid surfaces. Very clearly this influence of stiction on the apparent increase in the Young's modulus can be seen using weakly scattering silicone layers, in which the local depth-resolved strains can be readily visualized in the silicone bulk (experimental examples of such apparent stiffening due to stiction at the silicone-glass interface are shown in Ref. [8]). In practical measurements, putting lubrication (e.g. physiological saline solution) can be sufficient to significantly reduce the distorting role of stiction.

The above-presented considerations indicate that it makes no sense to state that one of cumulative strains C or S is "correct", because they reflect essentially different properties of the deformation process and both may be useful for different purposes.

For instance, for fairly large strains, when different material portions experience significant supra-pixel displacements, the varying positions of the tissue particles should be tracked as depicted in Fig. 3, which requires calculation of cumulative strains C to estimate the current thickness of the tissue layer separating every material particle and the OCT-probe surface.

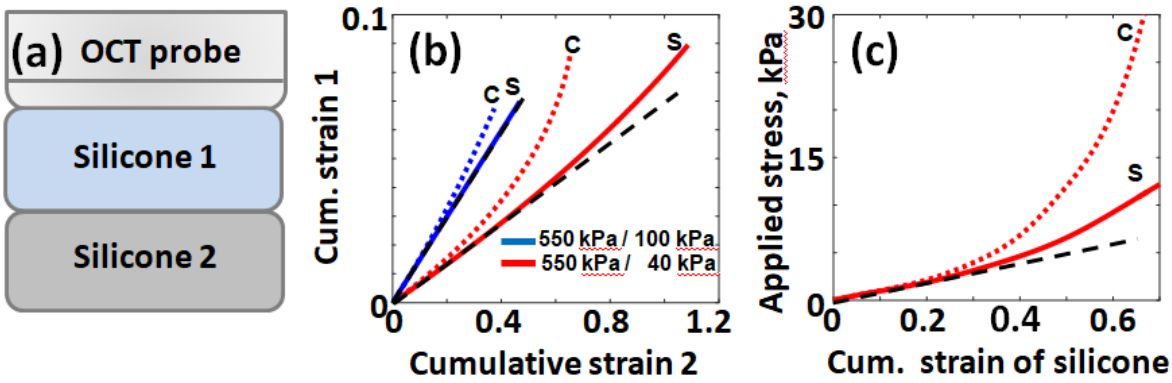


Fig. 5 Verification of linearity of stress-strain dependences for silicones. (a) is the scheme of the "self-calibration test" based on compression of two layers with strongly contrasting stiffness, so that sufficiently small strain ($S \approx C < 0.1$) in the stiffer silicone is linearly proportional to stress with a good accuracy. In plot (b) the vertical axis is for the smaller strain $S \approx C < 0.1$ of the stiffer silicone (proportional to stress with a good accuracy) and the horizontal axis corresponds to either C or S in the softer silicone. It is clear that for large strain $S \sim 0.4 - 0.5$, the dependences are nearly perfectly linear. For comparison, (c) shows the independent data from paper [7] for stress measured with a force cell and plotted as a function of cumulative strain C, as well as the same data recalculated as a function of strain S.

Next, if the goal is to verify linearity/nonlinearity of the elastic response for the tracked tissue portions, then cumulative strains S should be calculated for each tissue particle characterized by its initial depth and lateral coordinate. Thus, for characterization of nonlinear elastic response of tissues, it follows from the discussion of Fig. 5 that it is reasonable to plot the cumulative strain S in the reference silicone against strain S in the examined material with unknown elastic behavior. Due to the verified linearity, strain S in the pre-calibrated silicone readily allows one to quantify local axial stress for every lateral coordinate. For an elastically linear examined material (like another silicone), such a S -versus- S plot should be linear in the strain range up to 30–50%, although for further increase in strain, it is likely that adhesion/stiction influence may cause the deviation from the linear dependence even for a pair of ideally linear materials. For working with real biological tissues, such a strain range limited to 30–50% looks more than sufficient, because even for easily deformable tissues, usually strains should not exceed 10–20% to prevent irreversible mechanical damage. Furthermore, many tissues demonstrate pronounced elastic nonlinearity even for strains of the order of a few percent [8].

It should be emphasized that the sought nonlinear stress-strain dependences of real heterogeneous tissues should refer to every physical portion of the tissue rather that to every position in a fixed coordinate system. For strains on the order of several tens of percent, material particles may experience significant supra-pixel displacements, so that their tracking is critically important for obtaining the correct (undistorted) form the stress-strain curves for different components of real inhomogeneous tissues. The corresponding experimental examples demonstrating how these curves may be distorted without duly performed tracking are given in what follows.

5 How to visualize current elastic properties of the strongly deformed tissue

In the course of non-infinitesimal deformations, the tissue may pronouncedly change its form in the obtained series of images. Thus, tissue particles are characterized by different coordinates in different frames in the acquired series of images. In view of this, to enable comparison of the tissue properties for different stages of deformation, it is reasonable to ascribe the information about gradually-varying elastic properties of the tracked tissue particles by storing the current estimated elastic properties in the pixels corresponding to the initial coordinates of the particles. For the so-performed elastographic visualization, it is possible to clearly see how the elastic properties of every tissue portion are evolved, because in such a representation corresponding to the initial form of the tissue the geometrical form of tissue regions will remain invariable.

Before turning directly to the corresponding experimental examples, another important note should be made about visualization of the current (tangent) Young modulus. It is equal to the slope of the stress-strain curve $\Delta\sigma/\Delta S$, so that for tissues with nonlinear stress-strain dependences $\sigma(S)$ (like breast cancer sample discussed in Ref. [8]), the tangent Young's modulus strongly depends on the current stress (pressure). This pressure, however, in real conditions is usually rather non-uniform in the lateral direction over an OCT scan. The numerous reasons of this non-uniformity are incontrollable in practice [29]. In particular, the thickness of the reference silicone layer may fluctuate over the scan so that one region may already get in contact with the compressing OCT probe, whereas the other may be yet non-contacted; similarly the tissue surface often is pronouncedly non-planar; the tissue structure may be mechanically inhomogeneous laterally, so that the resultant strains for different coordinates may strongly differ even for the same stress value.

It is clear that in such situations utilization of force cells enabling the estimation of the average stress over the OCT probe surface does not help much, because the stress over the visualized region may unpredictably differ up to several times. In configurations similar to that shown in Fig. 6a, high linearity of silicones described by Eq. (15) makes it possible to use the silicone layer as a distributed fully-optical stress sensor [29]. When non-infinitesimal strains are of interest as discussed above, a series of OCT images are acquired and cumulative strains S and C are calculated using the above-described procedures with parallel displacement tracking. The current stress and strains of various tissue portions are attributed to their initial coordinates. Examples of such laterally inhomogeneous strain maps for various degrees of compression are shown in Fig. 6b. Having a series of such cumulative-strain maps, for every lateral coordinate (i.e., every A-scan) it is possible to find the frame number corresponding to a chosen stress value determined by the strain S in the pre-calibrated reference silicone (see Eq. (15)). Then the so-found A-scans with the desired stress level from strain maps with different numbers can be reassembled in a synthetic strain map, for which the stress is equal to the same pre-chosen value at every lateral coordinate. Such reassembled strain maps with the "standardized" stress over the entire scan are shown in the right part of Fig. 6b. This standardization allows one to estimate the current Young's modulus as the slope of the chord connecting the points with the pre-chosen stresses and corresponding strains as shown in Fig. 6b. In such a way maps of the Young's modulus for chosen standardized stresses can be readily plotted (see details in Ref. [29]). This procedure leads to the repeatability of the results, the possibility of comparing the stiffness both along one scan and among different scans and samples.

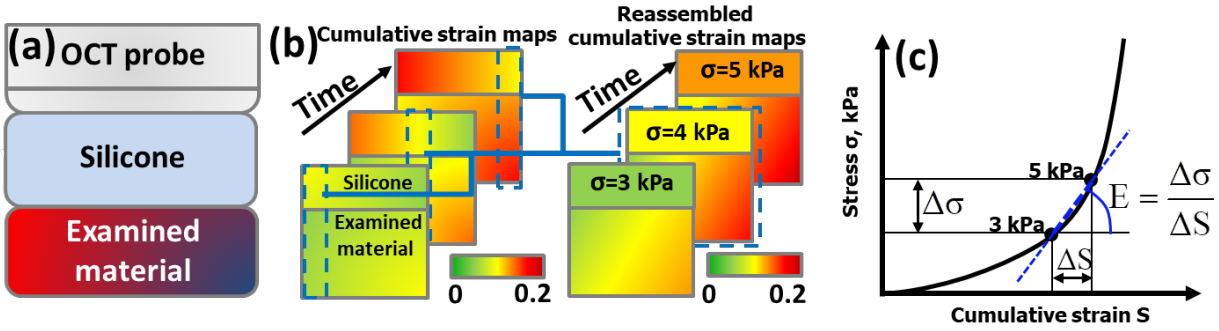


Fig. 6 Schematic of the OCE realization with silicone layers serving as optical stress sensors (a). A series of OCT scans obtains during compression of the tissue trough a silicone layer, in which its spatially-resolve cumulative strain S is linearly proportional to stress that may be laterally pronouncedly inhomogeneous as shown in the left part of panel (b). The right part of (b) shown a series of OCT scans with the same "standardized" pressure obtained by reassembling A-scans from the initially acquired OCT scans. Panel (c) shows an example of nonlinear stress-strain curve that can be obtained by plotting strain S in silicone proportional to stress according to Eq. (15) as a function of strain S in the studied tissue. After obtaining such spatially-resolved nonlinear curves, the Young's modulus of the tissue can be estimated for a chosen stress level.

Examples of application of these procedures to particular biomedical problems can be found in Refs. [22, 25] (morphological segmentation of human breast-cancer samples) and Ref. [26] (monitoring of morphological changes of animal-model tumors).

Using the experimental scheme depicted in Fig. 6, in the next section we discuss experimental examples demonstrating the key role of displacement tracking based on finding cumulative strain C, accompanied by finding cumulative strain S required for correct characterization of elastic properties of biological tissues.

6 Experimental examples demonstrating importance of self-consistent displacement and strain tracking for characterization of linear and nonlinear elastic properties of materials

The first example demonstrates strong influence of displacement tracking on the form of reconstructed stress-strain curves and the corresponding dependences of the tangent Young's modulus represented as a function of either current stress or strain of the tissue. For real nonlinear tissues, the latter dependences may differ quite significantly. Fig. 7 shows an example obtained for an excised rat cornea subjected to compression between two layers of soft reference silicone (with the Young's modulus $E = 50$ kPa). The experimental configuration is shown in Fig. 7a, where additionally a heating beam of IR laser is shown (because the experiments were made in the context of studies of new technologies of laser-assisted modification of microstructure and shape of collagenous tissues, which are in more detail discussed in Refs. [16, 30, 31]). The inhomogeneity of elastic properties of the corneal sample is related to the preliminary performed spatially-inhomogeneous moderate heating.

The structural images in the very beginning and at the end of the corneal sample compression are shown in Figs. 7b and 7c (notice that before compression the lower layer of silicone is not yet visible within the visualized depth). The initial position of the processing window is shown in Fig. 7b and its new position by the end of compression (tracked according to scheme shown in Fig. 2) is shown in Fig. 7c. In Fig. 7e the solid line shows the stress-strain curve found with correct tracking and the dashed line is obtained without tracking, i.e., for a processing window fixed in its initial position. It is clear that by the end of compression, the corneal layer inside the initial position of the processing window is completely substituted by the underlying silicone layer, so that the dashed curve is strongly distorted. Figs. 7f and 7g show the current slopes of the stress-strain curves (Young's modulus) found for the curves shown in Fig. 7e as functions of strain of the corneal tissue (for the tissue portion corresponding to the initial position of the processing window) and the stress applied to the tissue, respectively. Fig. 7f and 7g additionally clearly demonstrate that physically meaningful results with displacement tracking are strongly distorted when displacement tracking is not performed. Also, there is a clear difference between the dependences of the Young's modulus on either strain or stress. This fact is due to pronounced nonlinearity of the stress-strain relationship for the corneal tissue.

Figs. 7d and 7h show the 2D maps of the so-found Young's modulus distribution found for the stress 2 kPa standardized over the scan area (i.e., in the beginning of compression) and for much higher stress 30 kPa by the end of compression, respectively. Details of stress standardization can be found in Ref. [29]. Very strong stiffening of the corneal tissue is clearly seen in Fig. 7h in comparison with Fig. 7d, which is in contrast with invariable Young's modulus of the silicone layer in the upper parts of Figs. 7d and 7h.

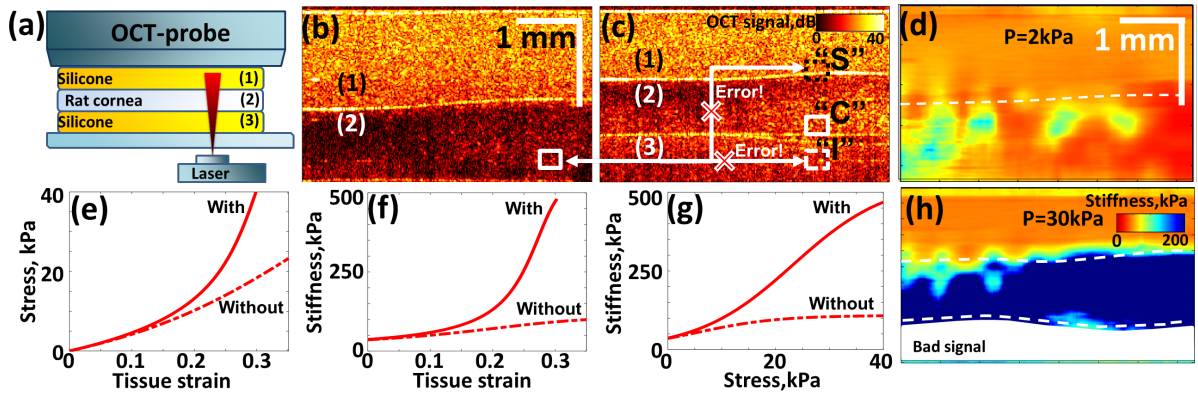


Fig. 7 Experimental demonstration of importance of displacements tracking for OCE examination of a strongly elastically nonlinear sample of rat cornea. Panel (a) illustrates experimental scheme of pore formation research based on stiffness changes of the rat cornea after laser exposure. Structural OCT images (b) and (c) corresponding to the beginning and end of compression clearly illustrate significant displacement of the scatterers. 2D plots (d) and (h) demonstrate changes in the shape, position and stiffness (with standardization of pressure by 2 kPa and 30 kPa) of the cornea in the beginning and by the end of compression. Panels (e), (f), and (g), for corneal particles in the irradiated zone, show stress-strain, stiffness-strain and stiffness-stress dependences in the correct and distorted forms found with and without displacement tracking, respectively. Index "I" in panel (c) denoted the initial position of the processing window (the same as in (b)) containing the tracked particles; index "C" shows the new position of the processing window containing the same tissue particles correctly found by calculating cumulative strain C, and index "S" shows erroneously found new position found using strain S instead of C. The dashed lines in (d) and (h) show the boundary between silicone and corneal tissue.

It can also be emphasized that the geometrical shape of the tissue in the OCT images may vary not only due to the mechanically created deformations, but may additionally be distorted by procedures of obtaining synthesized scans to enable stress standardization. Indeed, the physical stress distribution may be pronouncedly inhomogeneous, so that desired "standardized" stress at different lateral coordinates may be attained for scans with different numbers. Consequently, in the "standardized" scans, assembled using A-scans taken from initial scans with different numbers, the geometrical shape of the tissue in the resultant pressure-standardized images may differ from real geometrical shapes of the examined tissue. This gives an additional argument that, to better represent how strongly different tissue portions change their elastic properties for a certain applied stress, it is reasonable first to track gradually varying positions for every pixel, but then to place the estimated current elastic parameters for every tracked particle into the pixels corresponding to the initial positions of those particles rather than to their current positions.

Fig. 8 based on real measurements of deformed corneal sample (the same as in Fig. 7) demonstrates in another form the difference between cumulative strains S and C, as well as the influence of their usage on the resultant stiffness maps. We recall once again that it is strain C, which correctly characterizes the change in the thickness of the tissue layer according to Eqs. (6). For compressive strains, according to Eq. (11) $|C|<|S|$. The difference between S and C may be significant as is clearly seen from comparison of the displacement maps in Fig. 8, where panel (a) corresponds to cumulative strain C that gives correct estimates of particle displacements, whereas Fig. 8b shows for every tracked pixel cumulative strain S using which one may overestimate displacements by the end of compression. The structural image corresponding to the initial state of the corneal sample was shown in Fig. 7b, where the layer of linear silicone with $E = 40$ kPa is clearly seen above the nonlinear corneal tissue. Next, Fig. 8c shows the spatial distribution of the estimated Young's modulus by the end of compression (for the maximal stress 40 kPa). The estimated Young's modulus for every particle is stored in the pixels corresponding to the initial sample configuration. The back-shift in Fig. 8c in correctly made based on the estimated strain C shown in Fig. 8a. Since Fig. 8c is obtained using correct back-shift to the initial pixels, the so-obtained elasticity map clearly shows that the thickness of the uniform layer of silicone well corresponds to its thickness in the structural image in Fig. 7b. In contrast, in Fig. 8d the back-shift to initial positions was made incorrectly, using strain S shown in Fig. 7b. Cumulative strain S strongly overestimated displacements, such that because of the over-estimated back-shift, the uniform layer of silicone looks much thicker. Correspondingly, the overall stiffness distribution is strongly distorted. For the considered example with a clear boundary between the tissue and silicone (see structural scan in Fig. 7b), this inconsistency with Fig. 8d can be rather easily noticed. However, usually inside real tissues are no such high-contrast boundaries, so that it is not so simple to compare structural and derived elastographic images.

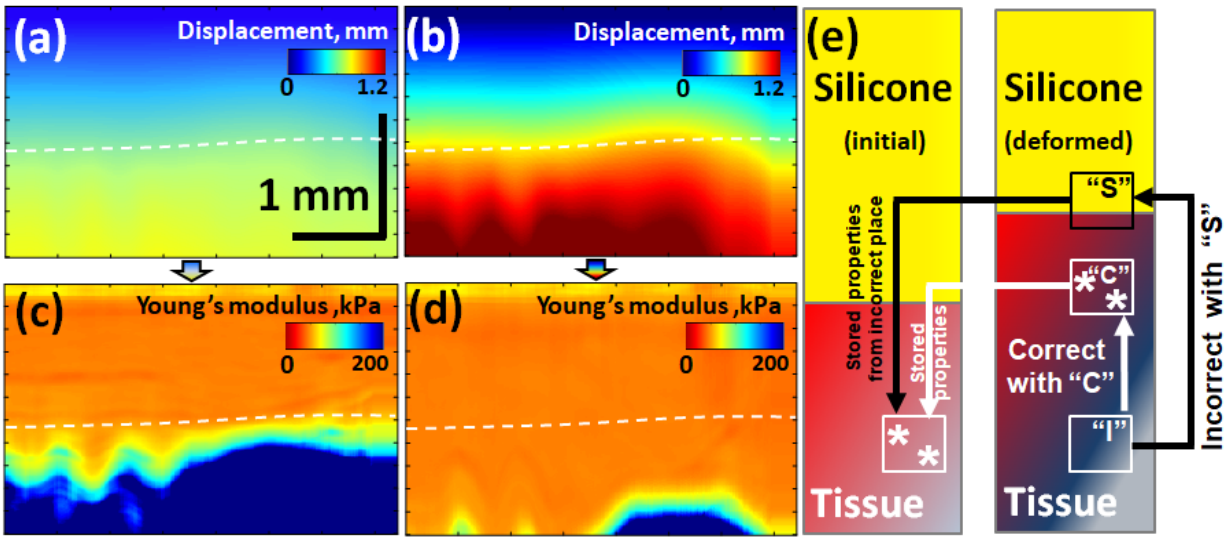


Fig. 8 Illustration of correct and incorrect displacement tracking (accumulated during gradual stress increase up to 40 kPa). Panel (a) is the correctly reconstructed displacement field based on the cumulative strain *C*; (b) is a similar incorrectly reconstructed displacement map based on utilization of cumulative strain *S*. (c) is the Young's modulus distribution obtained by correctly (d) is the Young's modulus map based on incorrectly back-shifted current position of every particle corresponding to panel (b) in which the displacement are over-estimated. Panel (e) schematically elucidates the reason of obtaining incorrectly back-shifted maps of elastic properties when the displacements are erroneously estimated using cumulative strain *S* instead of *C*. The dashed lines in panels (a)–(d) show the position of boundary between silicon and tissue as shown in the structural image in Fig. 6b.

Consequently, erroneously performed displacement tracking and back-shift of the current positions of particles may lead to strong distortions which are not easily detectable. Schematically the origin of the discussed errors in another form is elucidated in Fig. 8e, where correct (based on strain *C*) and overestimated (based on strain *S*) displacements and back-shifts are shown.

Fig. 8e demonstrates that when the displacement is significantly overestimated, one may erroneously place the current positions of tissue particles inside the layer of silicone and, consequently, to make too strong back-shift of the current positions of the tissue particles. Thus, the Young's modulus values actually found inside silicone can be erroneously ascribed to the tissue. When samples are mechanically depth-dependent and there are no evident layers/boundaries, the tracking of displacements can be based only on incremental estimations of strains, so that the proper method of finding cumulative strains is of key importance for correct displacement tracking.

Finally, it can be pointed out that the term "elastic properties" is not reduced to evaluation of the Young's modulus. Indeed, the described OCE method based on utilization of linear reference silicone layers enables obtaining nonlinear stress-strain dependences for examined tissues, from which not only the Young's modulus can be estimated (as elucidated in Fig 6c), but also dependences of the Young's modulus on either strain or applied stress can be derived as demonstrated in Figs. 7f and 7g. From the nonlinear stress-strain dependences and the derived pressure dependences of the Young's modulus one can estimate parameters of elastic nonlinearity of examined tissues. For example, one may use the following power-law expansion of the reconstructed stress-strain curves around a pre-selected stress σ_0:

$$\sigma = \sigma_0 + E(\sigma_0)\cdot(\varepsilon + \beta\varepsilon^2 + ...), \qquad (16)$$

where σ is the current stress, ε is strain, and σ_0 is the chosen initial stress around which the nonlinear stress-strain dependence is expanded; $E(\sigma_0)$ is the current (tangent) Young's modulus for $\sigma = \sigma_0$, and quantity β is the dimensionless nonlinearity parameter characterizing quadratic-in-strain nonlinearity.

By definition, the current Young's modulus corresponds to the slope of the stress-strain dependence (as illustrated in Fig. 6c), so that for the chosen pre-compression σ_0 one can write:

$$E(\sigma_0) = d\sigma / d\varepsilon\,|_{\sigma=\sigma_0}\,. \qquad (17)$$

As follows from Eq. (16), in the vicinity of point σ_0 the current Young's modulus can be represented as:

$$E(\sigma) = E(\sigma_0)\cdot(1 + 2\beta\varepsilon), \qquad (18)$$

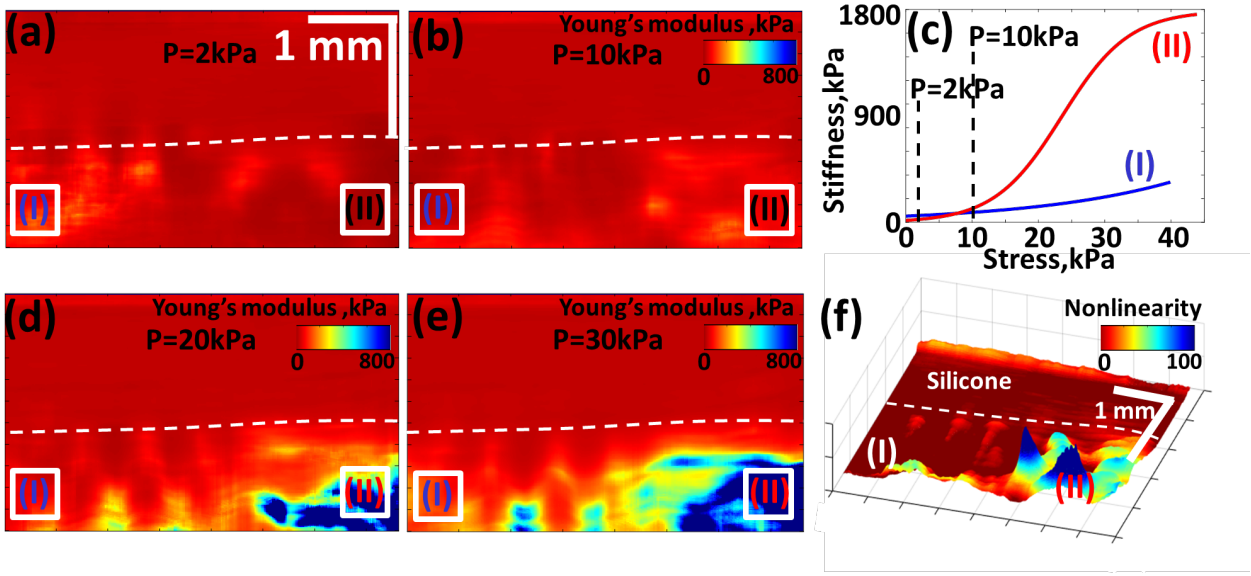


Fig. 9 Examples of the evolution of the Young's modulus maps with increasing stress and utilization of these maps for finding the nonlinearity parameter distribution. (a)–(e) Young's modulus maps for stresses 2 kPa, 15 kPa, 20 kPa, and 30 kPa, respectively. Panel (c) shows the stress-strain dependences for the regions (I) and (II) shown in panels (a)–(e). Panel (f) is the nonlinearity parameter distribution obtained by subtraction of the Young's modulus maps for 2 kPa and 10 kPa shown in panels (d) and (e).

so that the quadratic nonlinearity parameter β near the stress point σ_0 can be found as

$$\beta|_{\sigma=\sigma_0} = \frac{1}{2}\frac{dE}{E(\sigma_0)d\varepsilon} = \frac{1}{2}\frac{dE}{d\sigma}|_{\sigma=\sigma_0}. \qquad (19)$$

The initial stress $\sigma = \sigma_0$ can be chosen zero (corresponding to the very beginning of tissue compression) or some non-zero value may be chosen. Preliminary studies demonstrated that various tissue components (for example, morphological component of breast cancer) can exhibit very similar values of the Young's modulus, but at the same time the very same components may demonstrate clearly differing values of the nonlinear parameter β [22]. This fact opens the possibility to differentiate various tissue types using in combination the characteristic values of both the Young's modulus and the nonlinearity parameter.

In what follows for the same corneal sample that was used in Figs. 7 and 8, we demonstrate how the above described approach to mapping the current elastic properties of the tissue with the back-shift to the initial positions of the tissue particles can be used for convenient obtaining of the nonlinearity parameter. Indeed, it is clear that differential for of Eq. (19) can readily be represented in the difference form:

$$\beta|_{\sigma=\sigma_0} == \frac{1}{2}\frac{E(\sigma_0+\Delta\sigma)-E(\sigma_0)}{\Delta\sigma}|_{\sigma=\sigma_0}. \qquad (20)$$

Eq. (20) indicates that if one has the Young's modulus maps as in Fig. 8c obtained for fairly close stress levels σ_0 and $\sigma_0+\Delta\sigma$ with correct back-shift of the estimated local Young's moduli $E(\sigma_0)$ and $E(\sigma_0+\Delta\sigma)$ of the tracked tissue particles to the same initial pixels of the particles, then the pixel-to-pixel difference of such two maps $E(\sigma_0+\Delta\sigma)$–$E(\sigma_0)$ readily yields the map of the quantity $(1/2)\cdot\Delta\sigma\cdot\beta|_{\sigma=\sigma_0}$ proportional to the nonlinearity parameter.

Fig. 9 demonstrates the maps of the Young's modulus (similar to Fig. 8c) for four different levels of applied stress (2, 10, 20, and 30 kPa). The spatial inhomogeneity of the Young's modulus in the corneal sample is caused by spatially-inhomogeneous irradiation with the heating laser beam (see the scheme in Fig. 7a) prior to the elasticity measurements. The heating produces changes in the entire stress-strain curves, examples of which are shown in Fig. 9c for the regions labeled as (I) and (II). Finally, Fig. 9f shows the map of the nonlinearity parameter obtained by subtraction of the Young's modulus maps for 2 kPa and 10 kPa (Figs. 9a and 9b). Fig. 9f is represented in the pseudo-3D-form to clearer show the spatial inhomogeneity of the nonlinearity parameter. It is clear from Fig. 9c that in the stress range 2–10 kPa the Young's modulus values are fairly similar in regions (I) and (II), but the nonlinearity parameters are pronouncedly different as is clearly seen from Fig. 9f. Thus, combined consideration of both Young's modulus and nonlinearity parameter can be much more efficient for differentiation among various tissue types as demonstrated in Ref. [22] for breast cancer tissues.

We also emphasize that even if particles in the deformed material are gradually shifted with increasing pressure, the correctly-performed back-shift to the initial positions allows one to place the estimated elastic parameters to the invariable initial pixels of the particles. Due to this, for visualizing the nonlinearity-parameter

distribution, straightforward subtraction of the Young's modulus maps is sufficient.

7 Conclusions

In this paper we discuss the problem of correct tracking of particle displacement in compression optical coherence elastography. In the above consideration we focused on the axial displacements, although due to Poisson's effect axial compression also causes lateral strains and displacements. However, there are several factors due to which the effect of lateral displacements is of secondary importance compared with axial ones. Some of these factors relate to the OCT system and some other to the studied material and character of its deformation. First, from the viewpoint is signal analysis, the analyzed OCT signal phase is much stronger sensitive to axial scatterer displacements in comparison with lateral ones. Next, comparing displacements of tissue particles to neighboring pixels, it should be pointed out that the lateral size of pixels (in fact the diameter of a single axial A-scan) in conventional point-scanning OCT systems with weakly focused beams is several times greater than the vertical pixel size (the typical difference is 3–5 times). Another feature of scanning is that usually the A-scans are noticeably overlapped in the lateral direction (the typical overlap corresponds to another factor of 3–4 times). Thus, the neighboring A-scans visualize almost the same portion of the examined tissue. Comparing axial and lateral strains, it can be mentioned that for soft tissues with Poisson's ratio close to 0.5, lateral strains are twice smaller than the axial ones. Furthermore, for ideally plane-layered structures, in contrast to the depth dependence, the tissue properties do not depend on lateral positions at all, whereas the structure of many real biological tissues is close to plane-layered. Due to all these features, the elastographic images are at least an order of magnitude more tolerant to lateral motions.

By the above-mentioned reasons we focused on the problem of axial tracking in the context of estimation of larger strains and supra-pixel displacements, which has not specifically discussed in previous publications, although the interest to OCT-based phase-sensitive strain mapping and compression OCT-based elastography rapidly grows in the recent years in various research groups [7, 20, 32–34] (see also review [11] and Refs. therein). Obtaining of nonlinear stress-strain curves using compression OCT elastography opens previously unavailable prospects for high-selectivity differentiation of cancerous tissues [22]. For obtaining nonlinear stress-strain curves of real heterogeneous tissues in sufficiently broad strain ranges (say, for strains >10–20% that are still biologically non-destructive), the above-discussed tracking is of key importance. Without correctly performed displacement tracking one may obtain essentially erroneous maps of the reconstructed elastic parameters and, consequently, derive strongly incorrect diagnostic conclusions.

We demonstrated that even if direct measurements of such fairly strong interframe strains are prevented by strong decorrelation effects, correctly designed incremental procedures can be efficiently used to evaluate and map both linear and nonlinear elastic properties of examined tissues. For the discussed strain ranges up to several tens of percent, we considered various definitions of the notion of cumulative strain and elucidated which particular definition should be used for various applications/purposes. It was shown that incorrect choice of the definition may lead to essentially erroneous conclusions about the spatial distribution of the elastic properties and their nonlinearity. Although it this study we used a particular vector approach for phase-sensitive strain estimation, but generally speaking the procedures of self-consistent simultaneous tracking of large strains and displacements presented in Fig. 3 remain valid for other methods of incremental strain estimation (e.g., the least square phase-sensitive approach [3] or even amplitude-based correlational approaches if their accuracy can be made sufficient [35]).

The presented results construct the basis for rapidly developing biomedical diagnostic methods that are based on the utilization of differences in both linear and nonlinear elastic parameters of biological tissues, which is especially important for oncologic applications [22, 25–28].

Disclosures

The authors declare that they have no conflict of interest.

Acknowledgments

The study was supported by the Russian Science Foundation (Grant No. 22-12-00295).

References

1. J. Schmitt, "OCT elastography: imaging microscopic deformation and strain of tissue," Optics Express 3(6), 199–211 (1998).
2. J. Ophir, I. Cespedes, H. Ponnekanti, Y. Yazdi, and X. Li, "Elastography: A quantitative method for imaging the elasticity of biological tissues," Ultrasonic Imaging 13(2), 111–134 (1991).
3. B. F. Kennedy, S. H. Koh, R. A. McLaughlin, K. M. Kennedy, P. R. T. Munro, and D. D. Sampson, "Strain estimation in phase-sensitive optical coherence elastography," Biomedical Optics Express 3(8), 1865–79 (2012).

4. V. Y. Zaitsev, A. L. Matveyev, L. A. Matveev, G. V. Gelikonov, E. V. Gubarkova, N. D. Gladkova, and A. Vitkin, "Hybrid method of strain estimation in optical coherence elastography using combined sub-wavelength phase measurements and supra-pixel displacement tracking," Journal of Biophotonics 9(5), 499–509 (2016).
5. V. Y. Zaitsev, A. L. Matveyev, L. A. Matveev, G. V. Gelikonov, A. A. Sovetsky, and A. Vitkin, "Optimized phase gradient measurements and phase-amplitude interplay in optical coherence elastography," Journal of Biomedical Optics 21(11), 116005 (2016).
6. A. L. Matveyev, L. A. Matveev, A. A. Sovetsky, G. V. Gelikonov, A. A. Moiseev, and V. Y. Zaitsev, "Vector method for strain estimation in phase-sensitive optical coherence elastography," Laser Physics Letters 15(6), 065603 (2018).
7. K. M. Kennedy, L. Chin , R. A. McLaughlin, B. Latham, C. M. Saunders, D. D. Sampson, and B. F. Kennedy, "Quantitative micro-elastography: Imaging of tissue elasticity using compression optical coherence elastography," Scientific Reports 5, 15538 (2015).
8. V. Y. Zaitsev, A. L. Matveyev, L. A. Matveev, E. V. Gubarkova, A. A. Sovetsky, M. A. Sirotkina, G. V. Gelikonov, E. V. Zagaynova, N. D. Gladkova, and A. Vitkin, "Practical obstacles and their mitigation strategies in compressional optical coherence elastography of biological tissues," Journal of Innovative Optical Health Sciences 10(6), 1742006 (2017).
9. K. V. Larin, D. D. Sampson, "Optical coherence elastography–OCT at work in tissue biomechanics," Biomedical Optics Express 8(2), 1172–1202 (2017).
10. M. A.Kirby, I. Pelivanov, S. Song, Ł. Ambrozinski, S. J. Yoon, L. Gao, D. Li, T. T. Shen, R. K. Wang, and M. O'Donnell, "Optical coherence elastography in ophthalmology," Journal of Biomedical Optics 22(12), 121720 (2017).
11. V. Y. Zaitsev, A. L. Matveyev, L. A. Matveev, A. A. Sovetsky, M. S. Hepburn, A. Mowla, and B. F. Kennedy, "Strain and elasticity imaging in compression optical coherence elastography: The two-decade perspective and recent advances," Journal of Biophotonics 14(2), e202000257 (2021).
12. R. K. Wang, Z. Ma, and S. J. Kirkpatrick, "Tissue Doppler optical coherence elastography for real time strain rate and strain mapping of soft tissue," Applied Physics Letters 89(14), 144103 (2006).
13. R. K. Wang, S. J. Kirkpatrick, and M. T. Hinds, "Phase-sensitive optical coherence elastography for mapping tissue microstrains in real time," Applied Physics Letters 90(16), 164105 (2007).
14. V. Y. Zaitsev, A. L. Matveyev, L. A. Matveev, G. V. Gelikonov, A. I. Omelchenko, D. V. Shabanov, O. I. Baum, V. M. Svistushkin, and E. N. Sobol, "Optical coherence tomography for visualizing transient strains and measuring large deformations in laser-induced tissue reshaping," Laser Physics Letters 13(11), 115603 (2016).
15. H. Müller, L. Ptaszynski, K. Schlott, C. Debbeler, M. Bever, S. Koinzer, R. Birngruber, R. Brinkmann, and G. Hüttmann, "Imaging thermal expansion and retinal tissue changes during photocoagulation by high speed OCT," Biomedical Optics Express 3(5), 1025 (2012).
16. O. I. Baum, V. Y. Zaitsev, A. V. Yuzhakov, A. P. Sviridov, M. L. Novikova, A. L. Matveyev, L. A. Matveev, A. A. Sovetsky, and E. N. Sobol, "Interplay of temperature, thermal-stresses and strains in laser-assisted modification of collagenous tissues: speckle- contrast and OCT-based studies," Journal of Biophotonics 13(1), e201900199 (2019).
17. P. A. Shilyagin, L. A. Matveev, E. B. Kiseleva, A. A. Moiseev, V. Y. Zaitsev, A. A. Sovietsky, D. V. Shabanov, V. M. Gelikonov, K. S. Yashin, K. A. Achkasova, N. D. Gladkova, and G. V. Gelikonov, "Stabilization of the Scanning Pattern for Three-Dimensional Phase-Sensitive OCT Modalities: Angiography, Relaxography, and Monitoring of Slow Processes," Sovremennye Tehnologii v Medicine 11(2), 25 (2019).
18. S. Lawman, P. W. Madden, V. Romano, Y. Dong, S. Mason, B. M. Williams, S. B. Kaye, C. E. Willoughby, S. P. Harding, Y.-C. Shen, and Y. Zheng, "Deformation velocity imaging using optical coherence tomography and its applications to the cornea," Biomedical Optics Express 8(12), 5579–5593 (2017).
19. Y. Alexandrovskaya, O. Baum, A. Sovetsky, A. Matveyev, L. Matveev, E. Sobol, and V. Zaitsev, "Optical Coherence Elastography as a Tool for Studying Deformations in Biomaterials : Spatially-Resolved Osmotic Strain Dynamics in Cartilaginous Samples," Materials 15, 904 (2022).
20. T. A. Krouskop, T. M. Wheeler, F. Kallel, B. S. Garra, and T. Hall, "Elastic moduli of breast and prostate tissues under compression," Ultrasonic Imaging 20(4), 260–274 (1998).
21. Y. Qiu, F. R. Zaki, N. Chandra, S. A. Chester, and X. Liu, "Nonlinear characterization of elasticity using quantitative optical coherence elastography," Biomedical Optics Express 7(11), 4702 (2016).
22. E. V. Gubarkova, A. A. Sovetsky, L. A. Matveev, A. L. Matveyev, D. A. Vorontsov, A. A. Plekhanov, S. S. Kuznetsov, S. V. Gamayunov, A. Y. Vorontsov, M. A. Sirotkina, N. D. Gladkova, and V. Y. Zaitsev, "Nonlinear Elasticity Assessment with Optical Coherence Elastography for High-Selectivity Differentiation of Breast Cancer Tissues," Materials 15(9), 3308 (2022).
23. A. A. Sovetsky, A. L. Matveyev, L. A. Matveev, D. V. Shabanov, and V. Y. Zaitsev, "Manually-operated compressional optical coherence elastography with effective aperiodic averaging: Demonstrations for corneal and cartilaginous tissues," Laser Physics Letters 15(8), 085602 (2018).
24. Y. Bai, S. Cai, S. Xie, and B. Dong, "Adaptive incremental method for strain estimation in phase-sensitive optical coherence elastography," Optics Express 29(16), 25327–25336 (2021).

25. E. V. Gubarkova, A. A. Sovetsky, V. Y. Zaitsev, A. L. Matveyev, D. A. Vorontsov, M. A. Sirotkina, L. A. Matveev, A. A. Plekhanov, N. P. Pavlova, S. S. Kuznetsov, A. Y. Vorontsov, E. V. Zagaynova, and N. D. Gladkova, "OCT-elastography-based optical biopsy for breast cancer delineation and express assessment of morphological/molecular subtypes," Biomedical Optics Express 10(5), 2244 (2019).
26. A. A. Plekhanov, M. A. Sirotkina, A. A. Sovetsky, E. V. Gubarkova,S. S. Kuznetsov, A. L. Matveyev, L. A. Matveev, E. V. Zagaynova, N. D. Gladkova, and V. Y. Zaitsev, "Method for in vivo assessment of cancer tissue inhomogeneity and accurate histology-like morphological segmentation based on Optical Coherence Elastography", Scientific Reports 10(5), 2244–2263 (2019).
27. W. M. Allen, L. Chin, P. Wijesinghe, R. W. Kirk, B. Latham, D. D. Sampson, C. M. Saunders, and B. F. Kennedy, "Wide-field optical coherence micro-elastography for intraoperative assessment of human breast cancer margins," Biomedical Optics Express 7(10), 4139–4152 (2016).
28. L. Chin, B. Latham, C. M. Saunders, D. D. Sampson, and B. F. Kennedy, "Simplifying the assessment of human breast cancer by mapping a micro-scale heterogeneity index in optical coherence elastography," Journal of Biophotonics 10(5), 690–700 (2016).
29. A. A. Sovetsky, A. L. Matveyev, L. A. Matveev, E. V. Gubarkova, A. A. Plekhanov, M. A. Sirotkina, N. D. Gladkova, and V. Y. Zaitsev, "Full-optical method of local stress standardization to exclude nonlinearity-related ambiguity of elasticity estimation in compressional optical coherence elastography," Laser Physics Letters, 17(6), 065601 (2020).
30. V. Y. Zaitsev, A. L. Matveyev, L. A. Matveev, G. V. Gelikonov, O. I. Baum, A. I. Omelchenko, D. V. Shabanov, A. A. Sovetsky, A. V. Yuzhakov, A. A. Fedorov, V. I. Siplivy, A. V. Bolshunov, and E. N. Sobol, "Revealing structural modifications in thermomechanical reshaping of collagenous tissues using optical coherence elastography," Journal of Biophotonics 12(3), e201800250 (2019).
31. O. I. Baum, A. Yuzhakov, A. V. Bolshunov, V. I. Siplivyi, O. V. Khomchik, G. I. Zheltov, and E. Sobol, "New laser technologies in ophthalmology for normalisation of intraocular pressure and correction of refraction," Quantum Electronics 47(9), 860–866 (2017).
32. S. Kling, "Optical coherence elastography by ambient pressure modulation for high-resolution strain mapping applied to patterned cross-linking," Journal of the Royal Society, Interface 17(162), 20190786 (2020).
33. S. Kling, H. Khodadadi, and O. Goksel, "Optical Coherence Elastography-Based Corneal Strain Imaging During Low-Amplitude Intraocular Pressure Modulation," Frontiers in Bioengineering and Biotechnology 7, 453 (2020).
34. M. Singh, A. Nair, S. Aglyamov, and K. Larin, "Compression optical coherence micro-elastography of the cornea," Investigative Ophthalmology & Visual Science 62(8), 2033–2033 (2021).
35. V. Y. Zaitsev, A. L. Matveyev, L. A. Matveev, G. V. Gelikonov, V. M. Gelikonov, and A. Vitkin, "Deformation-induced speckle-pattern evolution and feasibility of correlational speckle tracking in optical coherence elastography," Journal of Biomedical Optics 20(7), 075006 (2015).

Novel UV-Releaser of Arachidonic Acid Based on Nitrophenyl-type Photoremovable Protecting Group

Darya N. Litunenko, Tatyana Yu. Karogodina, Alexey Yu. Vorob'ev, and Alexander E. Moskalensky*

Nososibirsk State University, 2 Pirogova str., Novosibirsk 630090, Russia

* **e-mail:** a.mosk@nsu.ru

Abstract. Arachidonic acid (AA) is one of the most important polyunsaturated fatty acids. It is the precursor to a wide range of eicosanoids, which are involved in many signaling cascades in the body. The conversion of arachidonic acid to eicosanoids starts with its liberation from membrane phospholipids by a dedicated enzyme. Here we present photolabile "caged" analog of AA, capable of liberation of the free acid under ultraviolet (UV) light with ~340–365 nm wavelength. This can be used in cell culture studies to mimic the first step in the biosynthesis of eicosanoids. We directly confirm the production of AA using high-performance liquid chromatography (HPLC). Furthermore, we found that novel compound yields 4-times more AA in comparison with previously published alternative. Our results demonstrate that the use of the caged compounds can be used to control the release of AA with UV light. The described caged analogs of AA are likely to be anchored in the membrane and enable light-triggered liberation of the free acid to the cytoplasm. This would be superior to the usual approach using the external addition of AA to cells, which suffers from poor solubility of the acid in culture medium and uncontrolled passage through membrane. © 2022 Journal of Biomedical Photonics & Engineering.

Keywords: arachidonic acid; photoremovable protecting group; caged compounds.

Paper #3498 received 13 Jun 2022; revised manuscript received 05 Sept 2022; accepted for publication 05 Sept 2022; published online 24 Sep 2022. doi: 10.18287/JBPE22.08.030305.

1 Introduction

Arachidonic acid (AA) is one of the most important polyunsaturated fatty acid with many physiological roles [1]. It is a component of the phospholipids which make up cellular membranes. AA is the precursor to a wide range of eicosanoids, including prostaglandins, thromboxanes, and leukotrienes [2]. Eicosanoids are small membrane-permeable lipid messengers, which have a lot of biological functions, including the regulation of inflammation and platelet activation. In particular, arachidonic cascade plays the main role in the developing of hyperinflammatory state during COVID-19 infection [3]. The key feature of lipid signaling is free diffusion through membranes. Thus, lipid messengers cannot be stored in vesicles and are biosynthesized locally. They usually have short lifetime, which ensures their local action. The study of lipid messengers biosynthesis and their spatial distribution is interesting both from fundamental point of view and for drug development.

The conversion of arachidonic acid to eicosanoids occurs in the cytoplasm and starts with its liberation from membrane phospholipids by phospholipase A2. The study of biosynthesis of eicosanoids *in vitro*, using the external addition of AA to cells, suffers from poor solubility of the acid in culture medium and uncontrolled passage through membrane. This problem can be solved by the use of photolabile "caged" analogs of arachidonic acid conjugated with photoremovable protecting groups (PPGs). Application of PPGs to control the activity of biological molecules has been widely used and extensively studied [4]. It allows one to use light to "uncage" the molecule and rapidly induce the desired effect. Importantly, the "uncaging" can be done independently of other processes associated with mixing, diffusion, and interaction with membranes, after equilibration of these processes [5]. Another important

feature is that light can be focused to induce local effect. The process can be triggered both outside cells and in the cytoplasm because cells are transparent to light.

Photolabile "caged" derivatives of AA were reported previously [6], including that with water-soluble protective group [7]. In this paper, we present and study two photolabile "caged" derivatives of AA, one previously described bearing 4,5-dimethoxy-2-nitrobenzyl protecting group (DMNB) [8] and novel bearing 1-(2-nitro-4,5-dimethoxyphenyl)ethyl protecting group (DMNPE). The goal of this paper is to compare their ability to release AA under UV light in terms of speed and total yield. To achieve this goal, we measure the dynamics of AA release during illumination using the HPLC technique.

2 Materials and Methods

2.1 Synthesis of the Compounds

The first compound, **Caged AA1 (**DMNB-caged AA, Fig. 1b**)** was synthesized as described in our previous paper [8]. A solution of 39.5 mg (0.13 mmol) of arachidonic acid in 2 ml of CH_2Cl_2 was added to 26.3 mg (0.12 mmol) of (4,5-dimethoxy-2-nitrophenyl)methanol. Then solutions of 1.5 mg 4-*N,N*-dimethylaminopyridine in 0.5 ml of CH_2Cl_2 and 30.0 mg (0.14 mmol) of DCC in 2 ml of CH_2Cl_2 were added with stirring. Resulted mixture was stirred for 2 hours, during this time white solid precipitate was formed. Solid was filtered off and filtrate was evaporated *in vacuo*. Oilish residue was chromatographed on SiO_2 with EtOAc-hexane (1:1) mixture as eluent. Fraction with $R_f \sim 0.35$ was collected. After removal of eluent yellowish oil was obtained, 39.0 mg (65%).

^{1}H NMR ($CDCl_3$, 400 MHz, J Hz): 0.83 (m, 3H); 1.18–1.33 (m, 6H); 1.63–1.76 (m, 3H); 1.84–1.94 (m, 1H); 2.05–2.13 (m, 2H); 2.36–2.42 (m, 2H); 2.72–2.81 (m, 6H); 3.91 (s, 3H); 3.93 (s, 3H); 5.24–5.39 (m, 8H); 5.46 (s, 2H); 6.96 (s, 1H); 7.67 (s, 1H).

HRMS (m/z): 499.2936 (exp), 499.2934 (calc).

Caged AA2 (DMNPE-caged AA, Fig. 1c**)** was synthesized analogously using 1-(4,5-dimethoxy-2-nitrophenyl)ethan-1-ol instead of (4,5-dimethoxy-2-nitrophenyl)methanol.

^{1}H NMR ($CDCl_3$, 400 MHz, J Hz): 0.86 (m, 3H); 1.18-1.36 (m, 6H); 1.58 (d, 3H, J = 6.5 Hz); 1.63-1.76 (m, 3H); 1.86-1.94 (m, 1H); 1.99-2.13 (m, 2H); 2.28-2. 36 (m, 2H); 2.72-2.81 (m, 6H); 3.91 (s, 3H); 3.93 (s, 3H); 5.24-5.41 (m, 8H); 6.45 (q, 1H, J = 6.5 Hz); 6.97 (s, 1H); 7.55 (s, 1H).

HRMS (m/z): 513.6659 (exp), 513.6655 (calc).

Photolysis mechanism of compounds conjugated with nitrobenzyl-based protecting groups has been described [9, 10]. Although it may depend on the solvent and pH, generally two products are formed: the "uncaged" compound and the "byproduct", or protecting group residual. The byproduct then degrades and form many different products (Fig. 1d).

2.2 Absorption Spectra and Photolysis

UV-VIS absorption spectra were measured in quartz cuvette with 10 mm light path using Shimadzu UV-1900 spectrophotometer. The photolysis ("uncaging") experiments were carried out in the same cuvette as follows. Compounds were dissolved in 3 mL of DMSO to the final concentration of 100 μM. We prepared a setup consisting of two UV LEDs with 365 nm central wavelength and 480 mW optical power. A microcontroller was used to set the illumination time. After each session of illumination, we measured UV-VIS absorption spectrum.

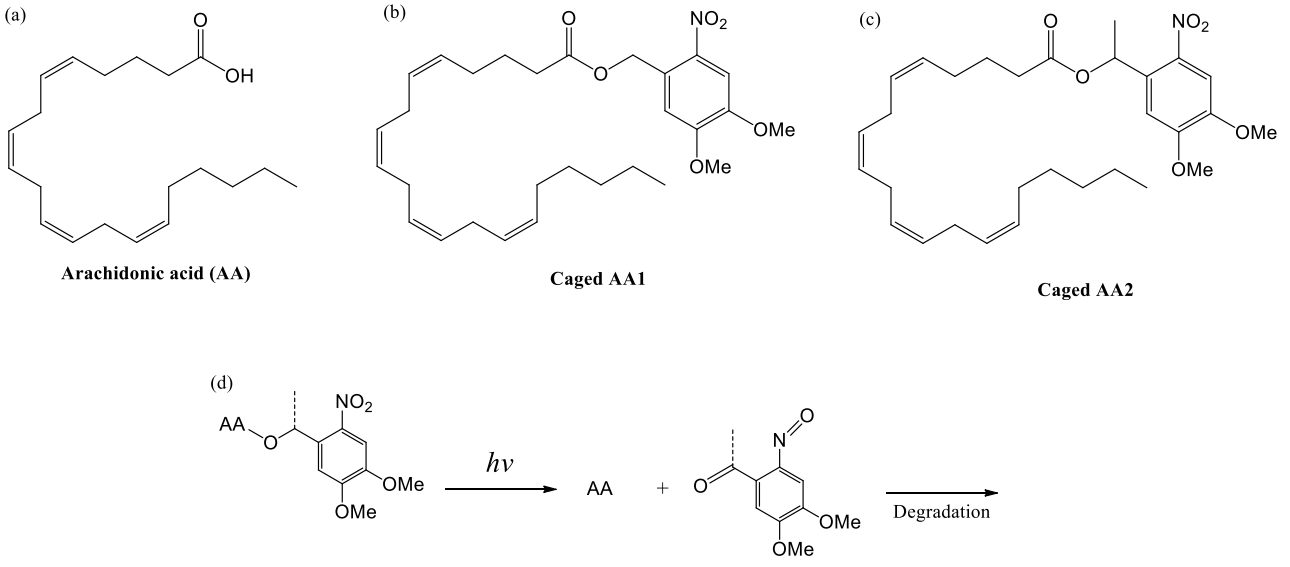


Fig. 1 (a) Arachidonic acid (AA); (b, c) two different analogs of AA conjugated with dimethoxynitrophenyl-type photoremovable protective groups; (d) the scheme of photolysis (photodecomposition).

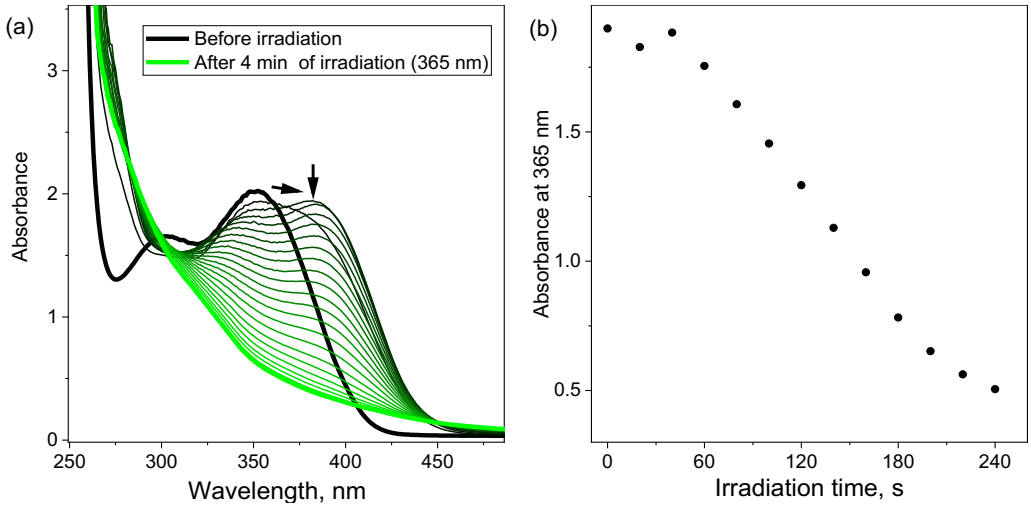


Fig. 2 (a) Absorption spectrum of **Caged AA2** during photolysis (irradiation by 365 nm LED); (b) the decrease of absorbance at 365 nm.

2.2 HPLC Experiments

HPLC experiments were done with Agilent 1260 Infinity II device equipped with Poroshell column (120 EC-C18, 3×150mm, 2.7µm) and diode-array detector. The separation conditions were as follows: 98% water / 2% ACN from 0 to 3 min; linear gradient to 100% ACN from 3 to 10 min; 100% ACN from 10 to 20 min. With these conditions, the retention time of AA was 14.3 min.

3 Results and Discussion

3.1 Absorption Spectra

While the unmodified AA does not absorb above 220 nm, the absorption spectra of both caged compounds have strong absorption band at 350 nm. The absorption spectrum for **Caged AA2** is shown in the Fig. 2a (black line). We measured extinction coefficients and obtained the following values: 7.9×10^4 $M^{-1}cm^{-1}$ for **Caged AA1** and 3.5×10^4 $M^{-1}cm^{-1}$ for **Caged AA2**.

Next, we performed the photolysis experiments as described in Section 0. The experimental results for **Caged AA2** are shown in the Fig. 2, and we published similar data for **Caged AA1** earlier [8]. The main absorption band first shifts to longer wavelength, indicating the formation of primary photoproduct of the PPG, and decays during further photolysis. Same shift to longer wavelength was observed in Ref. [11], and it was shown to be due the absorption of 2-nitrosobenzaldehyde. In our case, the primary photoproducts are 4,5-dimethoxy-2-nitrosobenzaldehyde and 1-(4,5-dimethoxy-2-nitrosophenyl)ethenone for **Caged AA1** and **Caged AA2**, respectively. Further decay in the absorption spectra is related to the formation of many different products from PPG residuals, which are hard to identify. The changes in absorption spectra indicate the conversion of compounds, but do not directly prove the release of AA. Therefore, we performed another set of experiments using HPLC approach.

3.2 Photorelease of Arachidonic Acid

To directly evaluate the photorelease of AA, we used the HPLC as described in the Section 0. First, we performed a calibration for pure AA dissolved in DMSO. Fig. 3 shows the increase of HPLC peak at 14.3 min. with the increasing concertation of AA (inset) and the linear calibration curve. This calibration curve was used in further experiments to determine the concentration of "uncaged" AA.

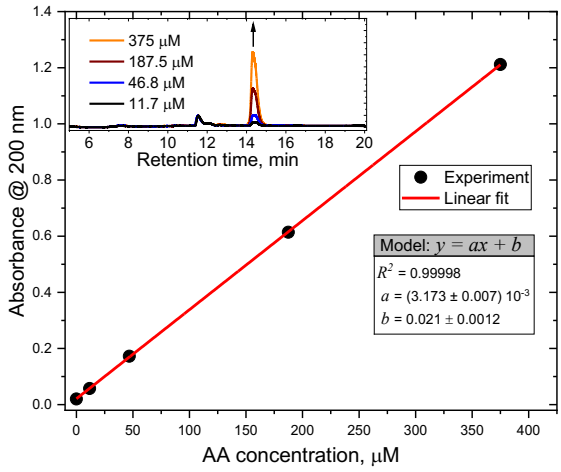


Fig. 3 Calibration curve (the height of HPLC peak at 14.3 min *versus* the concentration of AA in the sample). Inset shows the HPLC results.

The sample containing 250 µM of **Caged AA1** in 0.5 mL of DMSO was prepared in a transparent chromatographic vial. After recording the initial HPLC profile, we illuminated the sample using two UV LEDs with 340 nm central wavelength for 2 min and run the analysis again. This step was repeated several times until the release

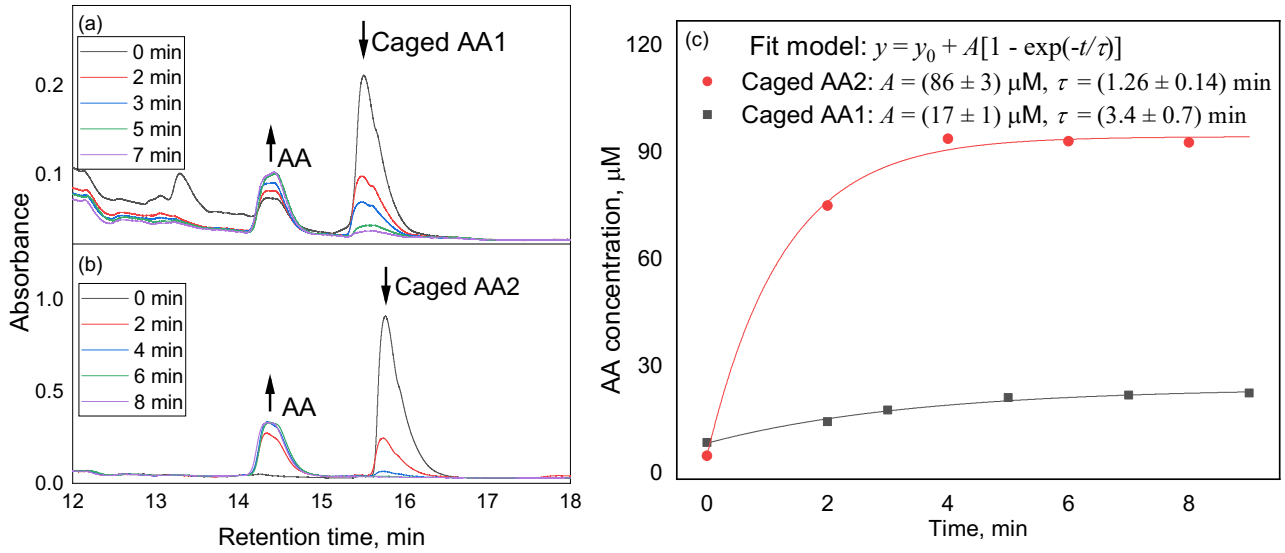


Fig. 4 (a) HPLC profiles during the illumination of **Caged AA1** by UV light; (b) the same for **Caged AA2**; (c) Production of the free AA in the course of illumination.

of AA stopped. Fig. 4a shows the obtained results. The same experiment was performed for the sample of **Caged AA2** with the concertation of 300 μM (Fig. 4b). HPLC peaks corresponding to caged analogs of AA decreased with illumination, in agreement with the photolysis experiments described in the previous section. However, the experiments cannot be compared directly because different LEDs were used and glass vials were used instead of quartz cuvettes. In contrast, the peak at 14.3 min retention time monotonically increased with illumination, indicating the photorelease of AA. According to the obtained kinetics, the photorelease of AA is faster for **Caged AA2** ($\tau = 1.26$ min *versus* 3.4 min). The total yield of AA is also much higher for **Caged AA2** despite lower extinction coefficient. Using the calibration curve, we determined the final concentration of AA, which was 17 μM for **Caged AA1** and 86 μM for **Caged AA2** (Fig. 4c), corresponding to 6.8% and 28.8% of the parent compound, respectively.

The obtained total yield is within the previously reported range for DMNB group [12]. The efficiency of the uncaging reaction varies greatly, depending on the functional group that has been caged and on the caging group itself. It is known that substitution at the benzylic site affects the photorelease quantum yields [13]. Methyl group in this site typically increases the efficiency, as it was first shown in Ref. [14], where the quantum yield increased from 13% to 64% in solution. Stronger electron-withdrawing group, such as CF_3, work even better, but they are not widely used because the synthesis is more difficult [15]. The study of the effect of substituents at the benzylic site for 4,5-dimethoxy nitrobenzene derivatives was performed in Ref. [16]. Previously there were no comparison between different groups for uncaging of AA, which is special carboxylic acid in terms of polyunsaturation. The fact that DMNPE counterpart provides more efficient uncaging of AA (in comparison with DMNB group) is in line with known data, but the total efficiency of 29% is quite high. For instance, DMNPE-caged ATP has the photorelease quantum yield of 7%.

Similar approach using HPLC technique was described recently [17] for AA derivatives based on coumarin-based photocaging group. The authors have not performed the calibration procedure and determination of total yield, but they estimated the time of total photolysis and obtained similar results as in the present papers (3–5 min). Coumarin-based groups have longer-wavelength absorption band (~380 nm) and the photorelease quantum yield in range of 4–22% [12]. Moreover, the groups were modified for specific subcellular localization, such as mitochondria, endoplasmic reticulum, lysosomes, and the plasma membrane. This enables photorelease of lipid messengers in distinct organelles, which is benefitial for biological studies because their action is usually highly localized. Further development of the present work would be also related with the modification of the caging group for specific subcellular localization, primarily the plasma membrane as it is the natural source of AA in cells.

Another promising direction in the development of "caged compounds" (not necessarily related to AA) is the use of visible-light PPGs. Visible (or near-infrared) light is capable of deep penetration into tissue, making it possible to accurately control the action of the drug in space and time [18]. This approach is promising for reducing the necessary dose of the drug and the accumulation of its active form in the environment [19, 20]. For *in vivo* applications, the PPGs operating in the single photon mode in the IR spectrum are required, and two major research directions exist in this area. The first is the use of BODIPY-based protecting groups [21, 22]. The second is the use of self-sensitizing molecules that generate singlet oxygen upon irradiation, which destroys the molecule itself and releases the active compound [23, 24]. However, this approach can be less compatible with AA because the unsaturated acid is easily oxidated by the reactive oxygen species.

4 Conclusion

In this paper, we present two photolabile "caged" analogs of AA, capable of liberation of the free acid under ultraviolet (UV) light with ~340–365 nm wavelength. We directly confirm the production of AA using HPLC method. Furthermore, we found that novel compound releases AA faster and has 4-times higher total yield in comparison with previously published alternative. Our results demonstrate that the use of the caged compounds can be used to control the release of AA with UV light. The described caged analogs of AA are likely to be anchored in the membrane and enable light-triggered liberation of the free acid to the cytoplasm. We anticipate that this approach will be used in cell culture studies to mimic the first step in the biosynthesis of eicosanoids.

Disclosures

The authors declare that they have no conflict of interest.

Acknowledgments

The study was supported by the Russian Science Foundation (grant #18-15-00049).

References

1. H. Tallima, R. El Ridi, "Arachidonic Acid: Physiological Roles and Potential Health Benefits – A Review," Journal of Advanced Research 11, 33–41 (2018).
2. J. J. Neitzel, "Fatty Acid Molecules: Fundamentals and Role in Signaling," Nature Education 3(9), 57 (2010). (accessed 30 May 2022) [https://www.nature.com/scitable/topicpage/fatty-acid-molecules-a-role-in-cell-14231940/].
3. M. A. R. Ripon, D. R. Bhowmik, M. T. Amin, and M. S. Hossain, "Role of Arachidonic Cascade in COVID-19 Infection: A Review," Prostaglandins Other Lipid Mediat 154, 106539 (2021).
4. M. Goeldner, R. Givens, Dynamic Studies in Biology: Phototriggers, Photoswitches and Caged Biomolecules, John Wiley & Sons (2006). ISBN 978-3-527-60554-5.
5. D. V. Spiryova, A. Y. Vorobev, A. Y. Vorobev, V. V. Klimontov, E. A. Koroleva, and A. E. Moskalensky, "Optical Uncaging of ADP Reveals the Early Calcium Dynamics in Single, Freely Moving Platelets," Biomedical Optics Express 11(6), 3319–3330 (2020).
6. A. Nadler, G. Reither, S. Feng, F. Stein, S. Reither, R. Müller, and C. Schultz, "The Fatty Acid Composition of Diacylglycerols Determines Local Signaling Patterns," Angewandte Chemie International Edition 52, 6330–6334 (2013).
7. X. Jie, H. Xupei, R. Sreekumar, and J. W. Walker, "Photolabile 'caged' fatty acids containing A 1-(2'-nitrophenyl)-1,2-ethanediol moiety," Bioorganic & Medicinal Chemistry Letters 7(10), 1243–1248 (1997).
8. A. Y. Vorob'ev, T. Y. Dranova, and A. E. Moskalensky, "Photolysis of Dimethoxynitrobenzyl-"caged" Acids Yields Fluorescent Products," Scientific Reports 9, 13421 (2019).
9. R. Givens, M. B. Kotala, and J.-I. Lee, "Mechanistic Overview of Phototriggers and Cage Release," in Dynamic Studies in Biology, M. Goeldner, R. S. Givens (Eds.), Wiley-VCH, Germany, 95–129 (2005). ISBN 978-3-527-60559-0.
10. C. D. Woodrell, P. D. Kehayova, and A. Jain, "Photochemically-Triggered Decarboxylation/Deamination of o-Nitrodimethoxyphenylglycine," Organic Letters 1(4), 619–622 (1999).
11. Y. V. Il'ichev, M. A. Schwörer, and J. Wirz, "Photochemical Reaction Mechanisms of 2-Nitrobenzyl Compounds: Methyl Ethers and Caged ATP," Journal of the American Chemical Society 126(14), 4581–4595 (2004).
12. G. C. R. Ellis-Davies, Basics of Photoactivation, Cold Spring Harb Protocols, New York, USA (2009).
13. P. Klán, T. Šolomek, C. G. Bochet, A. Blanc, R. Givens, M. Rubina, V. Popik, A. Kostikov, and J. Wirz, "Photoremovable Protecting Groups in Chemistry and Biology: Reaction Mechanisms and Efficacy," Chemical Reviews 113, 119–191 (2013).
14. E. Reichmanis, B. C. Smith, and R. Gooden, "O-Nitrobenzyl Photochemistry: Solution vs. Solid-State Behavior," Journal of Polymer Science: Polymer Chemistry Edition 23(1), 1–8 (1985).
15. A. Specht, M. Goeldner, "1-(o-Nitrophenyl)-2,2,2-Trifluoroethyl Ether Derivatives as Stable and Efficient Photoremovable Alcohol-Protecting Groups," Angewandte Chemie 116(15), 2042–2046 (2004).
16. I. Aujard, C. Benbrahim, M. Gouget, O. Ruel, J.-B. Baudin, P. Neveu, and L. Jullien, "O-Nitrobenzyl Photolabile Protecting Groups with Red-Shifted Absorption: Syntheses and Uncaging Cross-Sections for One- and Two-Photon Excitation," Chemistry – A European Journal 12(26), 6865–6879 (2006).
17. N. Wagner, M. Stephan, D. Höglinger, and A. A. Nadler, "Click Cage: Organelle-Specific Uncaging of Lipid Messengers," Angewandte Chemie International Edition 57(40), 13339–13343 (2018).
18. A. Yu. Vorobev, A. E. Moskalensky, "Long-Wavelength Photoremovable Protecting Groups: On the Way to in Vivo Application," Computational and Structural Biotechnology Journal 18, 27–34 (2020).
19. I. S. Shchelik, Novel Approaches to Antibacterial Delivery Systems and Light-Activated Antibiotics, Dissertation, University of Zurich (2021).

20. W. A. Velema, W. Szymanski, and B. L. Feringa, "Photopharmacology: Beyond Proof of Principle," Journal of the American Chemical Society 136(6), 2178–2191 (2014).
21. J. A. Peterson, C. Wijesooriya, E. J. Gehrmann, K. M. Mahoney, P. P. Goswami, T. R. Albright, A. Syed, A. S. Dutton, E. A. Smith, and A. H. Winter, "Family of BODIPY Photocages Cleaved by Single Photons of Visible/Near-Infrared Light," Journal of the American Chemical Society 140(23), 7343–7346 (2018).
22. K. Sitkowska, M. F. Hoes, M. M. Lerch, L. N. Lameijer, P. van der Meer, W. Szymański, and B. L. Feringa, "Red-Light-Sensitive BODIPY Photoprotecting Groups for Amines and Their Biological Application in Controlling Heart Rhythm," Chemical Communications 56(41), 5480–5483 (2020).
23. A. P. Gorka, M. J. Schnermann, "Harnessing Cyanine Photooxidation: From Slowing Photobleaching to near-IR Uncaging," Current Opinion in Chemical Biology 33, 117–125 (2016).
24. A. P. Gorka, R. R. Nani, J. Zhu, S. Mackem, and M. J. Schnermann, "A Near-IR Uncaging Strategy Based on Cyanine Photochemistry," Journal of the American Chemical Society 136(40), 14153–14159 (2014).

Justification of the Photoplethysmography Sensor Configuration by Monte Carlo Modeling of the Pulse Waveform

Denis G. Lapitan[1,*], Andrey P. Tarasov[1,2], and Dmitry A. Rogatkin[1]
[1] Moscow Regional Research and Clinical Institute ("MONIKI"), 61/2 Shchepkina str., Moscow 129110, Russia
[2] Federal Research Scientific Center "Crystallography and Photonics" of Russian Academy of Sciences, 59 Leninsky Avenue, Moscow 119333, Russia

*** e-mail:** lapitandenis@mail.ru

Abstract. Photoplethysmography (PPG) is an optical technique for detection of blood volume changes in the microvascular bed of a biological tissue. Many aspects of the PPG signal formation are still unclear. In particular, it is not known how the shape of a registered PPG signal depends on the geometry of tissue illumination. The aim of this study is to model the PPG waveform using the Monte Carlo (MC) method. For this, we developed a three-layer optical model of the skin in a reflectance geometry and verified it experimentally for different wavelengths (660, 810, and 940 nm) and source-detector distances (from 4 to 10 mm). The MC simulation results showed that the PPG waveform depends on the source-detector distance. The most pronounced diastolic wave is observed at the distance of 6 mm for the wavelength of 810 nm. The results obtained can be used for the development of reflectance PPG sensors. © 2022 Journal of Biomedical Photonics & Engineering.

Keywords: photoplethysmography; pulse waveform; model; Monte Carlo; simulation; source-detector distance.

Paper #3513 received 04 Aug 2022; accepted for publication 12 Sept 2022; published online 30 Sep 2022. doi: 10.18287/JBPE22.08.030306.

1 Introduction

Photoplethysmography (PPG) is a simple optical technique for detection of blood volume changes in the microvascular bed of a biological tissue [1]. The method is based on illumination of tissue with incoherent optical radiation in the visible and/or near-infrared range and recording a signal that has passed through or backscattered from the tissue [2]. The PPG signal registered consists of a variable component (AC), which is formed due to blood pulsations, and a slow varying component (DC) related to the average blood volume in a tissue [1]. Currently, PPG is actively used to assess parameters of the cardiovascular system. Clinical applications of PPG include monitoring of arterial oxygen saturation (pulse oximetry), pulse rate and its variability, cardiac output and respiration, assessment of microvascular blood flow and tissue viability, endothelial and vasomotor function, thermoregulation, etc. [1, 3]. However, morphological analysis of the pulse waveform (PW) extracted from the AC component of the PPG signal provides other important information about the state of blood vessels, for example, their stiffness, tone, compliance, etc. [4]. Therefore, it is very important to use a correct technique for recording and processing the pulse wave signal.

As known, the pulse wave consists of direct systolic and reflected diastolic waves, as well as a dicrotic notch, which characterizes the moment of aortic valve closure [4, 5]. Herewith, the PW registered in PPG depends on many factors such as the wavelength of light illuminating the tissue, the measurement site on the body, the elasticity of vessel walls, etc. [6–8]. Many aspects of a PPG signal formation cannot be studied experimentally *in vivo*, for example, how blood volume or the concentration of different chromophores affects the signal. Hence, many researchers use methods of theoretical modeling of light propagation in tissues. One of these most used methods is the Monte Carlo (MC) approach [9, 10].

S. Chatterjee et al. investigated the effect of blood volume and oxygen saturation on optical path of light by

MC modeling applied to the pulse oximetry technique [11]. They also explored the optical parameters to PPG (pathlength, penetration depth, absorbance, reflectance and transmittance) as the functions of multiple wavelengths and source-detector separations as well as the contributions of different tissue layers and sublayers in the formation of a PPG signal [12, 13]. For this, they developed a three-dimensional comprehensive MC model of finger-PPG. Andreia V. Moço et al. developed a multilayered MC model of the skin to simulate the separate contributions from skin layers containing pulsatile arterioles to the PPG signal in the 450–1000 nm range [14]. V. Dremin et al. explored the variations in diagnostic volume due to arterial blood pulsations [15]. However, the shape of the PPG signal has not been explored in models described above. As far as we know, there are no detailed studies on how the registered PW depends on the geometry of tissue illumination, for example, on the distance between a source and a detector. This is important at the development of PPG devices based on accurate reproduction and analysis of the pulse wave signal. So, the aim of this study is the MC modeling of the photoplethysmographic PW and experimental verification of simulation results.

2 Materials and Methods

2.1 Optical Model of the Tissue

We consider the illumination of biological tissue in a reflectance geometry in which a detector is located at a distance r from a light source. When developing an optical model of the skin, we used the classical volumetric approach to simulate the PPG signal [16]. It assumes that the intensity of the signal backscattered from the tissue is modulated by changes in the medium absorption, caused, in turn, by variations in the tissue blood volume. Thus, the key parameter of the model is the blood volume. Based on this, the skin was presented as a three-layer heterogeneous medium consisting of the epidermis, dermis and deeper subcutaneous fat (see Fig. 1). The epidermis is 0.2 mm thick, the dermis is 0.7 mm thick and the subcutaneous fat is semi-infinite [17]. The dermis and subcutaneous fat of the skin are characterized by a level of blood volume V_b, which can be considered as the relative total hemoglobin fraction (Hb and HbO_2) in the diagnostic volume of tissue [18].

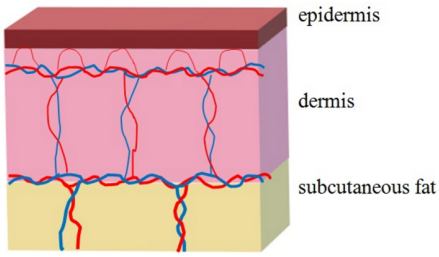


Fig. 1 Three-layer optical model of the skin.

The epidermis does not contain blood vessels and consists of connective tissue, melanin and water. Thus, we represent the absorption coefficient of the epidermal layer in the form [19]:

$$\mu_{a,epi}(\lambda) = V_{mel}\mu_{a,mel}(\lambda) + V_w\mu_{a,w}(\lambda) + \\ +\left[1-(V_{mel}+V_w)\right]\mu_{a,baseline}(\lambda), \quad (1)$$

where λ is the wavelength, V_{mel} and V_w are the volume fractions of melanin and water in the epidermis, respectively, $\mu_{a,mel}$ and $\mu_{a,w}$ are the absorption coefficients of melanin and water, $\mu_{a,baseline}$ is the baseline absorption coefficient, which characterizes the absorption of connective tissue in the absence of other chromophores. $\mu_{a,baseline}$ depends on the wavelength and can be expressed by the following equation [20, 21]:

$$\mu_{a,baseline}(\lambda) = 7.84\times10^{8}\times\lambda^{-3.255}[\mathrm{cm}^{-1}]. \quad (2)$$

The optical properties of the dermis are highly dependent on V_b. Since the dermis, in turn, consists of different layers, such as the papillary dermis, upper blood net dermis, reticular dermis and deep blood net dermis, the level of V_b in these layers varies. It is approximately 0.04 rel. units in the papillary dermis, 0.3 rel. units in the upper blood net dermis, 0.04 rel. units in the reticular dermis and 0.1 rel. units in the deep blood net dermis [22]. Thus, the average value of V_b of the entire dermis is approximately 0.1 rel. units. We write the absorption coefficient of the dermal layer as [13, 23]:

$$\mu_{a,derm}(\lambda) = V_{b,A}\mu_{a,A}(\lambda) + V_{b,V}\mu_{a,V}(\lambda) + V_w\mu_{a,w}(\lambda) + \\ +\left[1-(V_{b,A}+V_{b,V}+V_w)\right]\mu_{a,baseline}(\lambda), \quad (3)$$

where $V_{b,A}$ and $V_{b,V}$ are the volume fractions of arterial and venous blood in the dermis, respectively, $\mu_{a,A}$ and $\mu_{a,V}$ are the absorption coefficients of arterial and venous blood. $\mu_{a,A}$ and $\mu_{a,V}$, in turn, can be expressed in terms of arterial and venous oxygen saturation S_a^{oxy} and S_v^{oxy}, respectively, as [13, 24]:

$$\mu_{a,A}(\lambda) = S_a^{oxy}\mu_{a,HbO_2}(\lambda) + (1-S_a^{oxy})\mu_{a,Hb}(\lambda), \\ \mu_{a,V}(\lambda) = S_v^{oxy}\mu_{a,HbO_2}(\lambda) + (1-S_v^{oxy})\mu_{a,Hb}(\lambda), \quad (4)$$

where μ_{a,HbO_2} and $\mu_{a,Hb}$ are the absorption coefficients of oxygenated and deoxygenated hemoglobin.

Since the subcutaneous fat layer consists mainly of fat, we write the absorption coefficient of this layer as:

$$\mu_{a,subcut}(\lambda) = V_{b,A}\mu_{a,A}(\lambda) + V_{b,V}\mu_{a,V}(\lambda) + \\ +V_w\mu_{a,w}(\lambda) + \left[1-(V_{b,A}+V_{b,V}+V_w)\right]\mu_{a,fat}(\lambda), \quad (5)$$

where $\mu_{a,fat}$ is the absorption coefficient of fat.

2.2 Optical Properties of Skin Layers

In this study, we simulated the light propagation in the tissue by the MC approach using the developed three-layer model for the 3 wavelengths, namely: 660 nm, 810 nm and 940 nm. The absorption coefficients of melanin, oxyhemoglobin, deoxyhemoglobin, water, and fat were used from the literature [13, 19, 25–28]. When calculating the absorption coefficients of arterial and venous blood according to Eq. (4), S_a^{oxy} was set at 97% and S_v^{oxy} was set 30% lower, i.e. 67% [14]. The ratio of volume fractions of arterial and venous blood in the dermal and subcutaneous fat layers was 1:1 [13].

The scattering coefficient of each layer was determined as a combination of the Mie and Rayleigh theories in the form of an approximate dependence on the wavelength [29]:

$$\mu_s'(\lambda) = a' \left(\begin{array}{l} f_{Ray} \left(\dfrac{\lambda}{500(nm)} \right)^{-4} + \\ + \left(1 - f_{Ray}\right) \left(\dfrac{\lambda}{500(nm)} \right)^{-b_{Mie}} \end{array} \right), \quad (6)$$

where $\mu_s'(\lambda)$ is the reduced scattering coefficient, a' is the scaling factor, which is equal to μ_s' at the wavelength of 500 nm, f_{Ray} is the fraction of Rayleigh scattering, b_{Mie} is the power of Mie scattering. The coefficients a', f_{Ray} and b_{Mie} for all layers were adopted in accordance with the data of Salomatina et al. and used to calculate the scattering coefficient by Eq. (6) [29, 30]. The anisotropy factor and the refractive index were assumed to be 0.8 and 1.4 correspondingly for all skin layers [30].

Anatomical and optical parameters of skin layers are summarized in Tables 1 and 2, respectively.

2.3 Modeling of the Pulse Wave Signal

It is known that the AC component of the PPG signal is formed due to arterial blood pulsations [31]. Thus, we can represent the time change in arterial blood volume as a sum of harmonic oscillations:

$$V_{b,A}(t) = V_{b0,A} + \Delta V_{b,A}(t) = V_{b0,A} \left(1 + \sum_{k=1}^{n} m_k \sin(\Omega_k t) \right), \quad (7)$$

where $V_{b0,A}$ is a some average level of arterial blood volume, $\Delta V_{b,A}(t)$ is the variable component of arterial blood volume, n is the number of harmonics of $V_{b,A}$ changes, m_k is the relative amplitude of the k^{th} harmonic, Ω_k is the angular frequency of the k^{th} harmonic. m_k is defined as $A_k/V_{b0,A}$ (A_k is the absolute amplitude of the k^{th} harmonic). Variations in $V_{b,A}$ according to Eq. (7) lead to variations in the absorption coefficients of the dermal and subcutaneous fat layers in Eqs. (3) and (5), which, in turn, lead to amplitude modulation of the registered optical radiation in the PPG. Thus, the shape of the pulse wave can be unambiguously specified by setting the amplitudes m_k and frequencies Ω_k in Eq. (7).

Table 1 Anatomical properties of model layers.

Layer	Thickness, mm	V_{mel}, rel. units	V_w, rel. units	$V_{b,A}$, rel. units	$V_{b,V}$, rel. units
Epidermis	0.2	0.1	0.2	–	–
Dermis	0.7	–	0.6	0.05	0.05
Subcutaneous fat	∞	–	0.15	0.025	0.025

Table 2 Optical properties of tissue chromophores and model layers.

Optical parameter	Chromophore/ Layer	Wavelength, nm		
		660	810	940
μ_a, cm^{-1}	Melanin	269.4	136.2	83
	Water	0.0032	0.267	0.36
	Arterial blood (Hct = 45%)	1.95	4.02	6.43
	Venous blood (Hct = 45%)	6.42	4.17	5.77
	Fat	0.65	1.38	1.44
μ_s, cm^{-1}	Epidermis	227.4	183.9	161
	Dermis	139.5	111.1	97.4
	Subcutaneous fat	122.8	102.7	92

In this study, we used two harmonics to approximate the PW. The PW modeled in this way is shown in Fig. 2. The amplitudes of harmonics $m_1 = 0.069$ and $m_2 = m_1/1.5$ were adjusted so that the ratio of the variable component $\Delta V_{b,A}$ to the average level $V_{b0,A}$ was equal to 0.2 [32]. The frequencies of the first and second harmonics were set at 1 and 2 Hz, respectively.

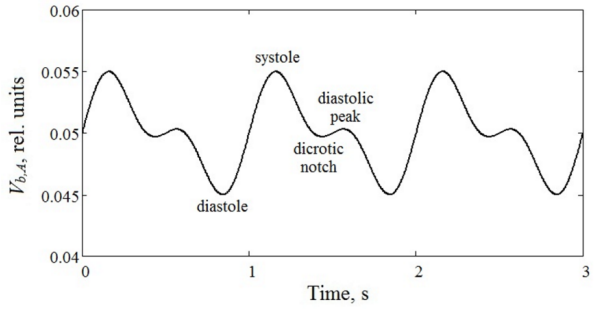


Fig. 2 Simulated time dependence of the arterial blood volume in the dermal layer, which is a pulse wave. $V_{b0,A} = 0.05$, $m_1 = 0.069$, $m_2 = m_1/1.5$, $\Omega_1 = 2\pi$ rad, $\Omega_2 = 2\times\Omega_1 = 4\pi$ rad.

The main blood pulsations occur in the dermis; however, recent studies have confirmed that they are also observed in the subcutaneous fat layer, in which larger arterioles and arteries are concentrated [14]. Herewith, the magnitude of $V_{b,A}$ oscillations in the subcutaneous fat is unknown from the literature, but it is known that it is less than in the dermis. The ratio of the $\Delta V_{b,A}$ to the $V_{b0,A}$ in the subcutaneous fat layer was assumed to be 8%.

2.4 Monte Carlo Simulation

In this study, we performed MC simulations to calculate the backscattered fluxes. The numerical model applied uses a photon weighting technique and is based on the well-known principles of MC simulation of photon transport in biological tissues [33, 34]. Disk-detector geometry was used to speed up the computation and to improve its accuracy [35]. In the simulation 6×10^7 photon packets were launched in the medium. A round source with a diameter of 1 mm and a 2×2 mm square detector were used. The registered flux was calculated relative to the incident flux illuminating the tissue (i.e. the relative backscattered flux) and then inverted relative to the flux at the diastole because the backscattered flux is inversely related to blood volume.

At the first stage, we calculated the backscattered fluxes at the moments of diastole and systole for all 3 wavelengths (660 nm, 810 nm and 940 nm) and for the following source-detector distances: 4, 6, 8, and 10 mm. Then, we calculated the AC/DC ratio of the PPG signal as:

$$\frac{AC}{DC} = \frac{Flux_{syst} - Flux_{diast}}{Flux_{diast}} \cdot 100\%, \qquad (8)$$

where $Flux_{syst}$ is the backscattered flux at the moment of systole, $Flux_{diast}$ is the backscattered flux at the moment of diastole.

At the second stage, we calculated the backscattered fluxes for 4 characteristic time points of the pulse wave (diastole, systole, dicrotic notch, and diastolic peak) at the wavelength of 810 nm and for source-detector distances from 2 mm to 10 mm with a step of 2 mm. Further, we calculated the pulse waveform index (PWI) as the flux difference between diastolic peak and dicrotic notch divided by the flux difference between systole and diastole:

$$PWI = \frac{Flux_{diast\_peak} - Flux_{dicr\_notch}}{Flux_{syst} - Flux_{diast}} \cdot 100\%, \qquad (9)$$

where $Flux_{diast\_peak}$ is the backscattered flux at the diastolic peak, $Flux_{dicr\_notch}$ is the backscattered flux at the dicrotic notch. This index characterizes the degree of expression of the diastolic peak.

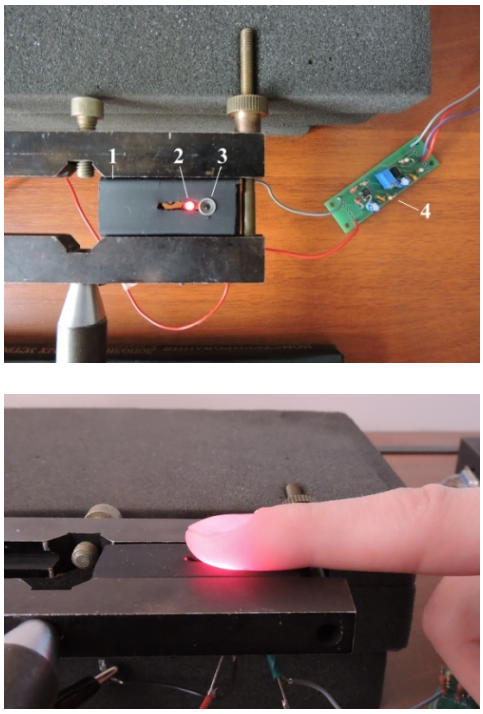


Fig. 3 Experimental setup for recording raw PPG signals from a subject's fingertip. 1 – rubber base, 2 – LED source, 3 – photodiode, 4 – signal amplification board.

2.5 Experimental Setup

To verify our model, we developed the experimental setup for recording raw PPG signals from a fingertip in a reflectance geometry (Fig. 3). The setup consists of a LED light source, a photodetector and a scheme of amplification and processing of the registered PPG signal. LED is controlled by the highly stable direct current source (QJ3003C III, Ningbo JiuYuan Electronic, China). The following LEDs were used as light sources: red LED (L-934SRC-C, Kingbright, China) with a peak emission wavelength of 660 nm and infrared (IR) LEDs

(IR-810-350C1, Power Light Systems, Germany; L-34F3C, Kingbright, China) with peak emission wavelengths of 810 and 940 nm, respectively. As a photodetector, a silicon photodiode (FD-10K, Russia) was used. Raw PPG signals from tissue were amplified by AD8033 amplifier (Analog Devices, USA), digitized by 16-bit analog-to-digital converter (ADS8320EB, Texas Instruments, USA) at a sampling frequency of 320 Hz and acquired in LabView (National Instruments, USA).

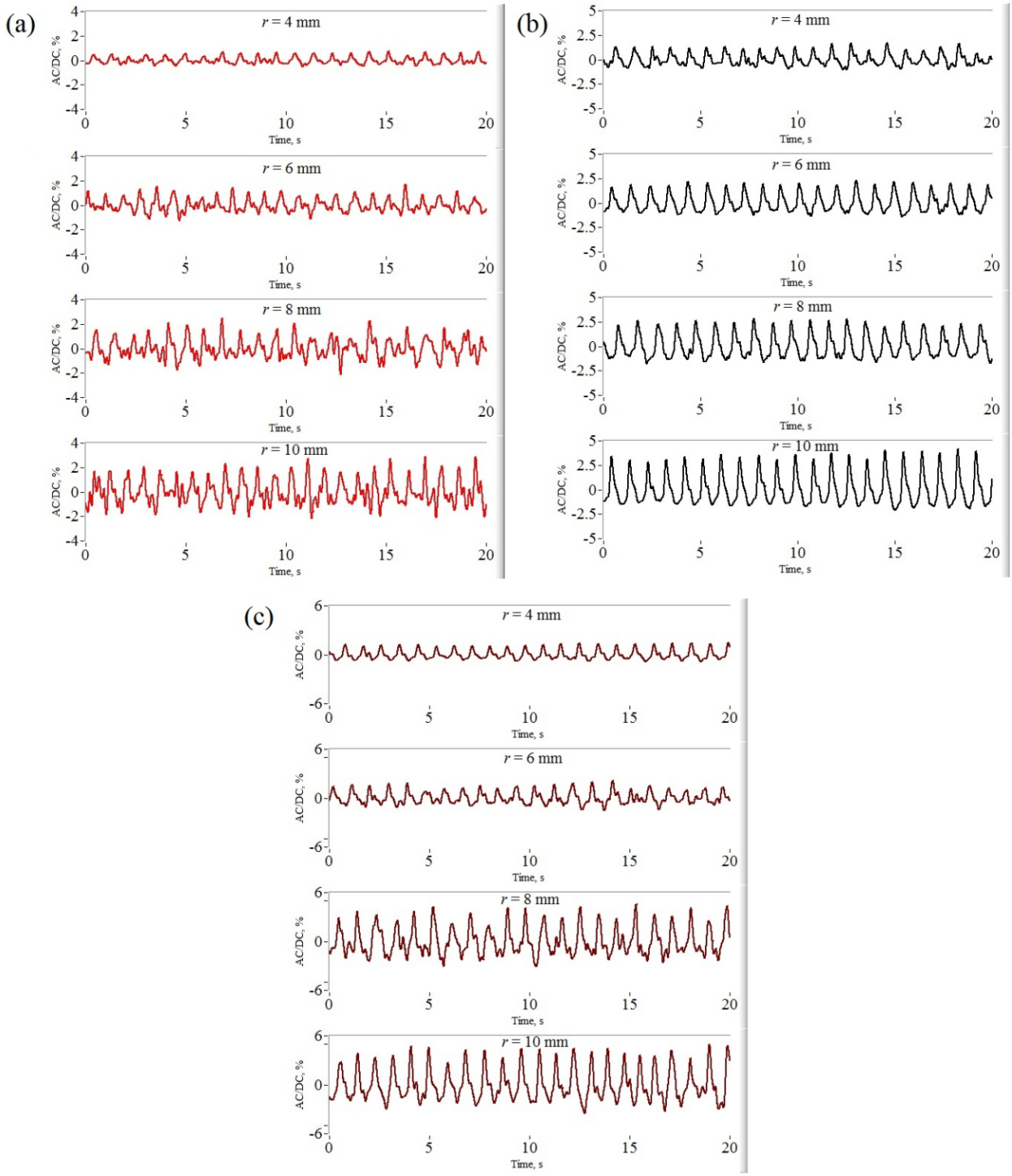


Fig. 4 An example of PPG signals, recorded from one subject for different source-detector distances (4, 6, 8, and 10 mm) at the wavelengths of 660 nm (a), 810 nm (b), and 940 nm (c).

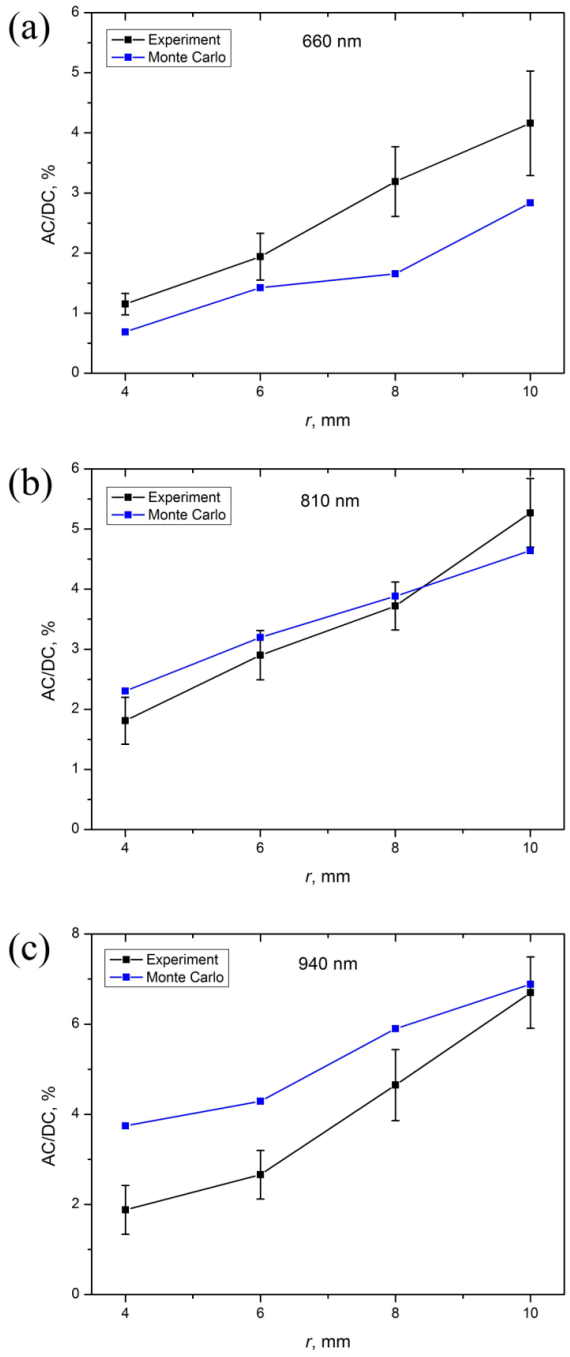


Fig. 5 The AC/DC ratio of the PPG signal for different source-detector distances obtained using MC method and from *in vivo* experiments for wavelengths of 660 nm (a), 810 nm (b), and 940 nm (c). The experimental AC/DC ratio is presented as mean ± standard deviation.

Raw PPG signals were recorded from the fingertips of 5 healthy subjects within one minute for each wavelength (660, 810, and 940 nm) and source-detector separation (4, 6, 8, and 10 mm). Further processing of the recorded signals was performed in LabView. The PPG signals were filtered with the 3rd order Butterworth filter in the frequency range from 0.5 to 5 Hz and normalized to the DC component. The AC/DC ratio was calculated for each pulse, averaged over all pulses in the one-minute recording and all subjects. The amplitude of the AC component was calculated as the difference between systolic and diastolic PPG signal levels.

Experimental procedures are consistent with ethical principles of the Declaration of Helsinki and were approved by the Independent Ethics Committee of Moscow Regional Research and Clinical Institute named after M. F. Vladimirsky (protocol No. 13). All persons gave their informed consent prior to their inclusion in the study.

3 Results and Discussion

Fig. 4 illustrates the PPG signals recorded on the experimental setup for different wavelengths and source-detector distances r from one subject. The signals are presented as the ratio of the AC component to the DC one. The AC/DC PPG signal increases with increasing source-detector separation. It should be noted that the AC and DC amplitudes of the PPG signal decrease with increasing source-detector distance, which was shown by Chatterjee S. et al. [13]. However, the DC component falls faster than the AC one, thus, the AC/DC ratio increases with increasing distance, which we obtained in the experiment. As can be seen, the PW is very variable, so it is very difficult to quantify it for different source-detector distances.

The AC/DC ratio of recorded PPG signals in comparison with the one obtained using MC simulations for different wavelengths and source-detector distances is shown in Fig. 5. Since the *in vivo* PPG signal is physiologically variable, the experimental AC/DC ratios are presented as mean and standard deviation, which was calculated over the entire record and averaged for all subjects. The difference between the experimental AC/DC ratio and the theoretical one did not exceed 2% for all wavelengths. The best fit was obtained for the wavelength of 810 nm. To note, the directly proportional dependence of the AC/DC ratio on source-detector distance is not a surprise. Such behavior can be also obtained using the modified Beer-Lambert law as was shown in our previous study [36]. In general, the theoretical and experimental values of AC/DC ratio for different wavelengths are consistent with the data of other researchers [14].

Thus, the results of MC simulation have a good agreement with the experimental data, which made it possible to proceed to the next stage − PW modeling. The PPG waveform was modeled for the isobestic wavelength of 810 nm to eliminate the influence of oxygen saturation on the results. The simulated PW in the form of time dependence of $V_{b,A}$ (see Eq. (7)) and the results for the registered flux at characteristic points of the pulse wave obtained through MC simulation for different source-detector distances are presented in Fig. 6. As can be seen, the values of the numerically calculated fluxes do not exactly follow the analytical PW. This indicates the dependence of the PW on the source-detector distance. The best match of MC fluxes to the simulated pulse wave signal was obtained for a distance of 6 mm.

The obtained dependence of the PWI on source-detector distance is presented in Fig. 7. As can be seen, the maximum of the PWI is observed at the distance of 6 mm. Thus, within our equipment configuration, this distance should be used to register the backscattered PPG signal with the most pronounced diastolic peak. It is important to note that the problem of identifying the diastolic peak from the PW is acute since many physiological indices are calculated using it, such as the reflection index, the stiffness index, the dicrotic index, etc. [5, 37]. Therefore, researchers are looking for new approaches to best distinguish the diastolic wave. In particular, Liang Y. et al. investigated various types of filters and showed that the Chebyshev II filter of 4th order can improve the PPG signal quality more effectively than other types of filters and can be used for PPG signal processing to make the systolic and diastolic waves more salient [38]. Our results show that the diastolic wave can be more clearly identified at the stage of recording the PPG signal before filtering, if one uses an optimal distance between a source and a detector. In this study, the optimal distance is 6 mm for the wavelength of 810 nm. But this distance can also depend on the parameters of used equipment, in particular, the geometry of the light source and photodetector and the light wavelength. Further studies are needed to explore the significance of each parameter.

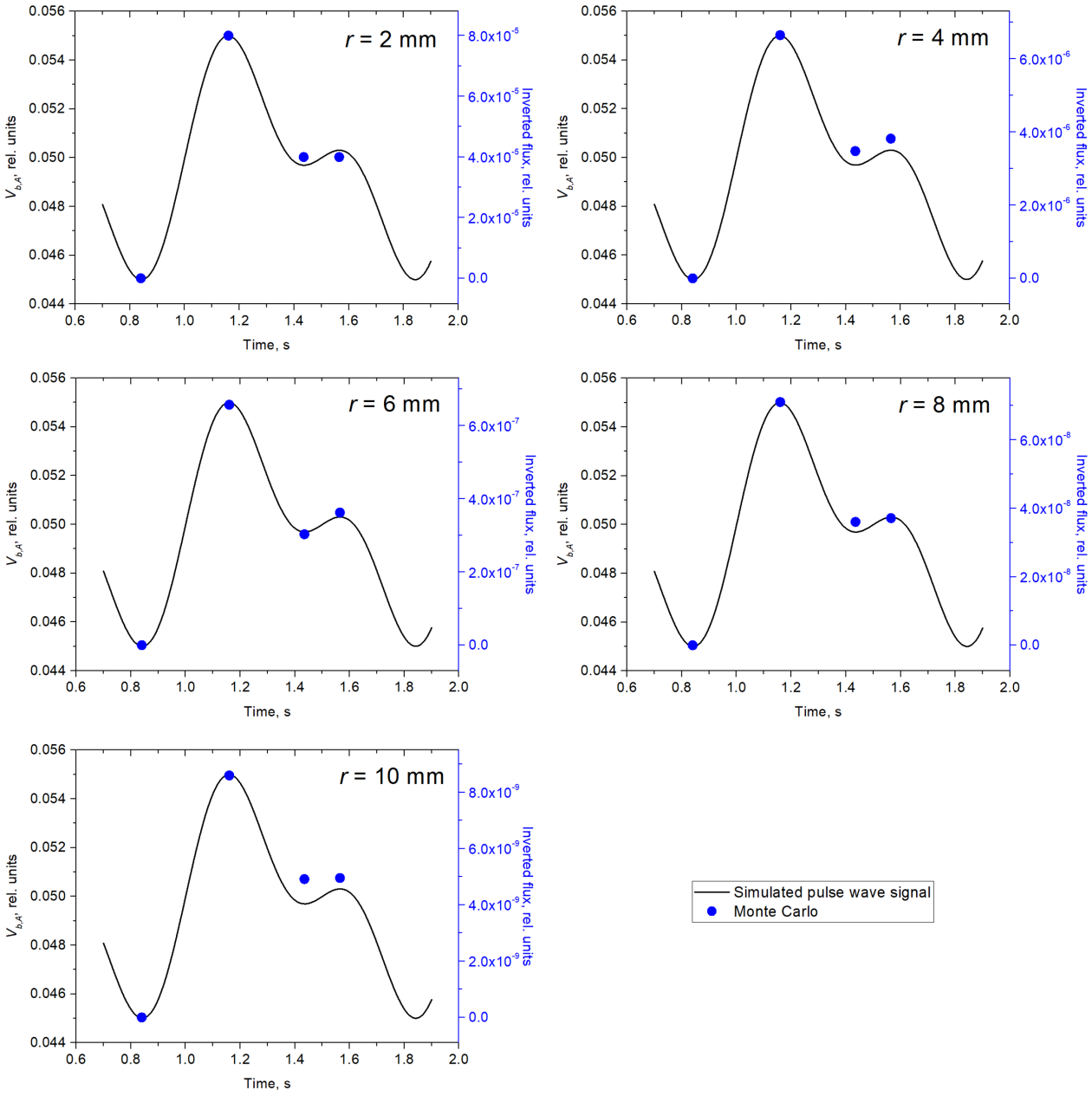


Fig. 6 The simulated PW (black line) and the fluxes at 4 time points of the pulse wave (blue dots) calculated by MC at the wavelength of 810 nm for different source-detector distances. The MC scale (right) was adjusted so that the amplitudes of the fluxes at the diastole and systole corresponded to the simulated signal.

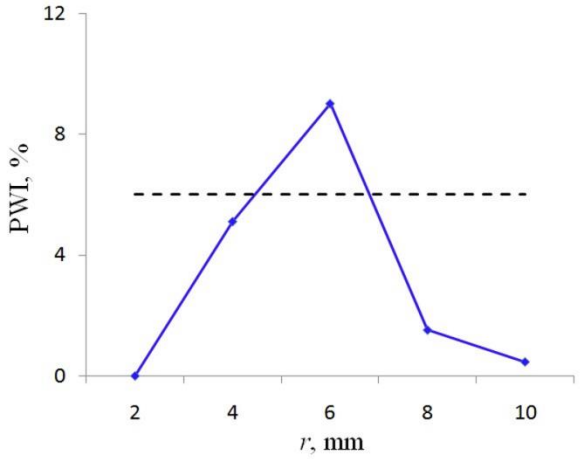


Fig. 7 The pulse waveform index (PWI) of the theoretical dependence of $V_{b,A}$ on time (black dotted line) and flux values by MC at the wavelength of 810 nm (blue line) for different source-detector distances.

4 Conclusions

In this study, we proposed a three-layer reflectance model of the skin for MC simulation of the photoplethysmographic PW. The model was verified in the experiment for different wavelengths and showed a good agreement with experimental data. Using MC simulation, the main characteristic points of the pulse wave (diastole, systole, dicrotic notch, and diastolic peak) were modeled. It was found that the PW depends on the source-detector distance. The most pronounced diastolic wave is observed at a distance of 6 mm for a wavelength of 810 nm. The results obtained can be used for a deeper understanding of the formation of a PPG signal at the development of reflectance PPG sensors.

Disclosures

The authors declare that they have no conflict of interest.

Acknowledgments

This work was supported by the Russian Science Foundation (project No. 21-75-00037). D. Lapitan also thanks V. Dremin (Orel State University, Russia) for his help in providing the optical properties of the tissue.

References

1. J. Allen, "Photoplethysmography and its application in clinical physiological measurement," Physiological Measurement 28(3), R1–R39 (2007).
2. A. A. R. Kamal, J. B. Harness, G. Irving, and A. J. Mearns, "Skin photoplethysmography–a review," Computer Methods and Programs in Biomedicine 28(4), 257–269 (1989).
3. J. L. Moraes, M. X. Rocha, G. G. Vasconcelos, J. E. Vasconcelos Filho, V. H. C. De Albuquerque, and A. R. Alexandria, "Advances in photopletysmography signal analysis for biomedical applications," Sensors 18(6), 1894 (2018).
4. M. Elgendi, "On the analysis of fingertip photoplethysmogram signals," Current Cardiology Reviews 8(1), 14–25 (2012).
5. S. C. Millasseau, J. M. Ritter, K. Takazawa, and P. J. Chowienczyk, "Contour analysis of the photoplethysmographic pulse measured at the finger," Journal of Hypertension 24(8), 1449–1456 (2006).
6. L. G. Lindberg, P. A. Oberg, "Photoplethysmography. Part 2. Influence of light source wavelength," Medical & Biological Engineering & Computing 29(1), 48–54 (1991).
7. J. Allen, A. Murray, "Age-related changes in the characteristics of the photoplethysmographic pulse shape at various body sites," Physiological Measurement 24(2), 297–307 (2003).
8. V. Hartmann, H. Liu, F. Chen, Q. Qiu, S. Hughes, and D. Zheng, "Quantitative comparison of photoplethysmographic waveform characteristics: effect of measurement site," Frontiers in Physiology 10, 198 (2019).
9. D. W. O. Rogers, "Fifty years of Monte Carlo simulations for medical physics," Physics in Medicine & Biology 51(13), R287 (2006);
10. V. V. Tuchin, Tissue optics, Society of Photo-Optical Instrumentation Engineers (SPIE), Bellingham, WA, USA (2015).
11. S. Chatterjee, J. P. Phillips, and P. A. Kyriacou, "Monte Carlo investigation of the effect of blood volume and oxygen saturation on optical path in reflectance pulse oximetry," Biomedical Physics & Engineering Express 2(6), 065018 (2016).
12. S. Chatterjee, P. A. Kyriacou, "Monte Carlo analysis of optical interactions in reflectance and transmittance finger photoplethysmography," Sensors 19(4), 789 (2019).
13. S. Chatterjee, K. Budidha, and P. A. Kyriacou, "Investigating the origin of photoplethysmography using a multiwavelength Monte Carlo model," Physiological Measurement 41(8), 084001 (2020).
14. A. V. Moço, S. Stuijk, and G. de Haan, "New insights into the origin of remote PPG signals in visible light and infrared," Scientific Reports 8(1), 8501 (2018).

15. V. Dremin, E. Zherebtsov, A. Bykov, A. Popov, A. Doronin, and I. Meglinski, "Influence of blood pulsation on diagnostic volume in pulse oximetry and photoplethysmography measurements," Applied Optics 58(34), 9398–9405 (2019).
16. A. Reisner, P. A. Shaltis, D. McCombie, H. H. Asada, D. S. Warner, and M. A. Warner, "Utility of the photoplethysmogram in circulatory monitoring," Anesthesiology 108(5), 950–958 (2008).
17. J. L. Reuss, "Multilayer modeling of reflectance pulse oximetry," IEEE Transactions on Biomedical Engineering 52(2), 153–159 (2005).
18. A. V. Dunaev, E. A. Zherebtsov, D. A. Rogatkin, N. A. Stewart, S. G. Sokolovski, and E. U. Rafailov, "Substantiation of medical and technical requirements for noninvasive spectrophotometric diagnostic devices," Journal of Biomedical Optics 18(10), 107009 (2013).
19. S. L. Jacques, "Skin optics summary," Oregon Medical Laser Center News, January 1998 (accessed 16 May 2022). [https://omlc.org/news/jan98/skinoptics.html].
20. I. S. Saidi, "Transcutaneous optical measurement of hyperbilirubinemia in neonates," PhD Thesis, Rice University, USA (1992).
21. S. L. Jacques, "Origins of tissue optical properties in the UVA, visible, and NIR regions," Advances in Optical Imaging and Photon Migration, Technical Digest Series, OPC364 (1996).
22. I. V. Meglinski, S. J. Matcher, "Quantitative assessment of skin layers absorption and skin reflectance spectra simulation in the visible and near-infrared spectral regions," Physiological Measurement 23(4), 741–753 (2002).
23. I. V. Meglinski, S. J. Matcher, "Computer simulation of the skin reflectance spectra," Computer Methods and Programs in Biomedicine 70(2), 179–186 (2003).
24. D. G. Lapitan, D. A. Rogatkin, "Variable hyperemia of biological tissue as a noise source in the input optical signal of a medical laser Doppler flowmeter," Journal of Optical Technology 83(1), 36–42 (2016).
25. N. Bosschaart, G. J. Edelman, M. C. Aalders, T. G. van Leeuwen, and D. J. Faber, "A literature review and novel theoretical approach on the optical properties of whole blood," Lasers in Medical Science 29(2), 453–479 (2014).
26. G. M. Hale, M. R. Querry, "Optical constants of water in the 200-nm to 200-m wavelength region," Applied Optics 12(3), 555–563 (1973).
27. C. R. Simpson, M. Kohl, M. Essenpreis, and M. Cope, "Near-infrared optical properties of ex vivo human skin and subcutaneous tissues measured using the Monte Carlo inversion technique," Physics in Medicine & Biology 43(9), 2465–2478 (1998).
28. A. N. Bashkatov, E. A. Genina, and V. V. Tuchin, "Optical properties of skin, subcutaneous, and muscle tissues: a review," Journal of Innovative Optical Health Sciences 4(1), 9–38 (2011).
29. S. L. Jacques, "Optical properties of biological tissues: a review," Physics in Medicine & Biology 58, R37–R61 (2013).
30. E. Salomatina, B. Jiang, J. Novak, and A. N. Yaroslavsky, "Optical properties of normal and cancerous human skin in the visible and near-infrared spectral range," Journal of Biomedical Optics 11(6), 064026 (2006).
31. J. Allen, C. P. Oates, T. A. Lees, and A. Murray, "Photoplethysmography detection of lower limb peripheral arterial occlusive disease: a comparison of pulse timing, amplitude and shape characteristics," Physiological Measurement 26(5), 811–821 (2005).
32. J. M. Schmitt, G. X. Zhou, E. C. Walker, and R. T. Wall, "Multilayer model of photon diffusion in skin," Journal of the Optical Society of America A 7(11), 2141–2153 (1990).
33. S. A. Prahl, M. Keijzer, S. L. Jacques, and A. J. Welch, "A Monte Carlo model of light propagation in tissue," SPIE Proceedings 10305, 1030509 (1989).
34. L. Wang, S. L. Jacques, and L. Zheng, "MCML–Monte Carlo modeling of light transport in multi-layered tissues," Computer Methods and Programs in Biomedicine 47(2), 131–146 (1995).
35. A. P. Tarasov, "Acceleration of Monte Carlo simulation of light transport in tissues using disk-detector geometry in the backscattering problem," in 2020 International Conference Laser Optics (ICLO), 2–6 November 2020, Saint Petersburg, Russia (2020).
36. D. G. Lapitan, A. P. Tarasov, "Analytical assessment of the modulation depth of photoplethysmographic signal based on the modified Beer-Lambert law," in 2019 IEEE 8th International Conference on Advanced Optoelectronics and Lasers (CAOL), 6–8 September 2019, Sozopol, Bulgaria, 103–106 (2019).
37. E. von Wowern, G. Östling, P. M. Nilsson, and P. Olofsson, "Digital photoplethysmography for assessment of arterial stiffness: repeatability and comparison with applanation tonometry," PloS ONE 10(8), e0135659 (2015).
38. Y. Liang, M. Elgendi, Z. Chen, and R. Ward, "An optimal filter for short photoplethysmogram signals," Scientific Data 5(1), 180076 (2018).

Examining the Validity of Input Lung CT Images Submitted to the AI-Based Computerized Diagnosis

Aleksandra A. Kosareva[1,2*], Dzmitry A. Paulenka[2], Eduard V. Snezhko[2], Ivan A. Bratchenko[3], and Vassili A. Kovalev[2]

[1] Belarusian State University of Informatics and Radioelectronics, 6 P. Brovki str., Minsk 220013, Belarus
[2] The United Institute of Informatics Problems of NAS of Belarus (UIIP NASB), Biomedical Image Analysis Department, 6 Surhanava str., Minsk 220012, Belarus
[3] Samara University, Department of Laser and Biotechnical Systems, 34 Moskovskoe shosse, Samara 443086, Russia

*** e-mail:** kosareva@bsuir.by

Abstract. A well-designed CAD tool should respond to input requests, user actions, and perform input checks. Thus, an important element of such a tool is the pre-processing of incoming data and screening out those data that cannot be processed by the application. In this paper, we consider non-trivial methods of chest computed tomography (CT) images verifications: modality and human chest checks. We review sources to develop training datasets, describe architectures of convolution neural networks (CNN), clarify pre-processing and augmentation processes of chest CT scans and show results of training. The developed application showed good results: 100% classification accuracy on the test dataset for modality check and 89% classification accuracy on the test dataset for checking of lungs presence. Analysis of wrong predictions showed that the model performs poorly on biopsy of lungs. In general, the developed input data validation model shows good results on the designed datasets for CT image modality check and for checking of lungs presence. © 2022 Journal of Biomedical Photonics & Engineering.

Keywords: image classification; medical imaging; convolutional neural network; deep learning; computer-aided diagnosis; computed tomography; input validation.

Paper #3500 received 23 Jun 2022; revised manuscript received 05 Sep 2022; accepted for publication 16 Sep 2022; published online 30 Sep 2022. doi: 10.18287/JBPE22.08.030307.

1 Introduction

Thanks to the advent of Artificial Intelligence and Deep Learning methods a large number of CAD (Computer-Aided Diagnosis) tools are becoming available. One of the challenges of using such tools in real practice is incorrect input data, including incorrect modalities and other anatomical organs that are mistakenly fed into the system but not intended to be processed by the specific software. In this case, the diagnostic results will lead to incorrect results from the CAD system. For example, in one trial among 7830 Chest XRay images received from various hospitals in 10 countries, there were 564 cases, containing flawed data of such kind [1]. The input data may contain errors, for example, upside down images, different file format, different modality, wrong organs, etc. [2–4].

In this paper, we consider the validity check of input chest CT images. This important phase of any software for medical image processing and analysis is rarely considered in detail during scientific research. If some data is not valid for a specific application (for example, the shape, modality, content or orientation of the image does not match the business logic of the application), it should be dropped out and given a clear descriptive message. For computed tomography (CT) scans of human lungs, there are three main verification processes:

1. Trivial checks to verify that the input image is indeed a 3D scan with the required parameters in its header (check the actual format of an image file, check image volume rank, check that the image contains non-zero data, etc.);

2. Modality check to verify that the input image is CT scan and not ultrasound, PET, MRI or binary mask image;
3. Human chest check to test that input CT scan contains lungs in necessary proportion to be processed by the application.

In this article we review different datasets and describe CNN architectures to perform non-trivial methods of chest CT images verification. Currently these non-trivial checks can only be solved using neural networks. The developed methods show good results on the designed datasets. We obtained 100% classification accuracy on the test dataset for modality check and 89% classification accuracy on the test dataset for checking lung presence. Analysis of wrong predictions showed that the model for checking lung presence performs poorly on biopsy of lungs.

2 Materials and methods

2.1 Materials

Dataset used for CT image modality check. The training dataset (acronym DS1) is divided into two classes (CT and non-CT) with 113 images in each class (total 226 3D images). The 3D image data classes of CT and "Non-CT" (ultrasound, PET, MRI, binary masks) used in this study originated from fifteen datasets [5]:

1. COVID-19 CT segmentation (14 CT scans, 7 3D masks [6]).
2. Lung CT Segmentation Challenge 2017 (14 CT scans [7]).
3. Lung Nodule Analysis 2016 (14 CT scans [8]).
4. Private CT dataset from UIIP NASB (15 CT scans).
5. Pancreas-CT (TCIA) (14 CT scans [9]).
6. DeepLesion (14 CT scans [10]).
7. Head-Neck-PET-CT (14 CT scans [11]).
8. ACRIN-NSCLC-FDG-PET (ACRIN 6668) (14 CT scans, 12 PET images [12]).
9. Anti-PD-1 Immunotherapy Lung (12 PET images [13]).
10. Ultrasound data of a variety of liver masses (B-mode-and-CEUS-Liver) (15 ultrasound images [14]).
11. Prostate MRI and Ultrasound with Pathology and Coordinates of Tracked Biopsy (Prostate-MRI-US-Biopsy) (10 ultrasound images, 7 MRI Images and 5 3D masks [15]).
12. OASIS (10 MRI images [16]).
13. BRAINS Imagebank (10 MRI images [17]).
14. Breast-MRI-NACT-Pilot (10 MRI images [18]).
15. MRI Dataset for Hippocampus Segmentation (10 MRI images, 5 3D masks [19]).

We also used an additional dataset to test the trained model, which contains 50 non CT series. Test dataset includes cases from the aforementioned datasets, as well as additional datasets of digital mammography and radiography:

1. The VICTRE Trial: Open-Source, In-Silico Clinical Trial for Evaluating Digital Breast Tomosynthesis (35 mammography images [20]).
2. CPTAC-PDA (15 XRay images [21]).

Dataset used for checking of lungs presence. The training dataset (acronym DS2) is divided into two classes (lungs and non-lungs) with 293 images in each class for training and 41 images for testing part (Fig. 1), total 668 3D images.

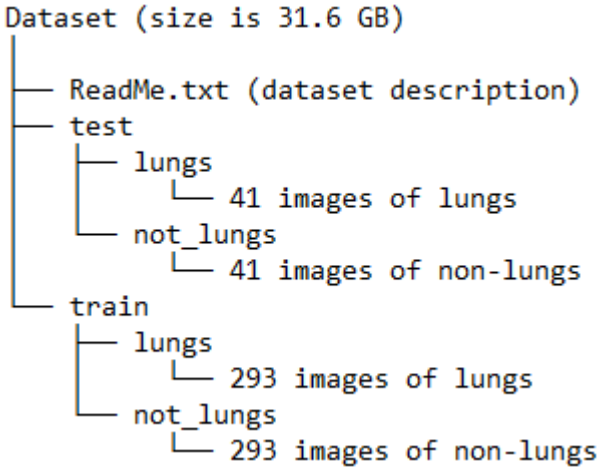


Fig. 1 Dataset DS2 directory structure which is used for checking of lungs presence.

The CT image data used in this study originated from the following twelve sources.

1. STOIC2021-COVID-19 AI Challenge (57 CT scans of lungs [22]).
2. Private dataset of Tuberculosis Portals (81 CT scans of lungs [1]).
3. ACRIN-NSCLC-FDG-PET (ACRIN 6668) (256 CT scans of different body parts [12]).
4. CT images with lung caverns from National Center of Tuberculosis and Lung Diseases, Georgia (13 CT scans of lungs and 11 3D lung masks).
5. MosMedData: Chest CT Scans with COVID-19 Related Findings COVID19_1110 1.0 (24 CT scans of lungs and 11 3D lung masks [23]).
6. RibFrac Dataset: A Benchmark for Rib Fracture Detection, Segmentation and Classification (23 CT scans of lungs [24]).
7. Coronacases Initiative and Radiopaedia (10 CT scans of lungs).
8. IH Pancreas-CT Dataset (43 CT scans of abdomen [9]).
9. Head-Neck-PET-CT (68 CT scans of the head and upper body [11]).
10. Private CT dataset from UIIP NASB (21 CT lung masks).
11. CQ500 Dataset (23 CT scans of the head and upper body [25]).
12. NODE21 dataset (27 CT images of box-shaped regions containing lung nodules [26]).

Some smaller part of dataset images was artificially created and added to the train and test datasets:

1. Artificial biopsy images and multiple lungs to classify them as non-lungs;
2. Doubled lungs to classify them as non-lungs;
3. Slightly cropped images at the top and bottom of lungs to classify them as lungs;
4. Significantly cropped images of lungs to classify them as non-lungs;
5. Images of chest with head to classify them as lungs.

2.2 The Method of CT Image Modality Check

After trivial checks which are not considered in this paper, the next step is to check if the modality of an input data is CT scan or not. Medical input data are often provided in DICOM format, when a modality attribute (0008,0060) is available, so the modality check is trivial in this case. However, for a general purpose only image data are available, thus the more sophisticated task of modality estimation by image content becomes the only way. In order to solve this problem, we use a Deep Learning technique based on convolutional neural networks. The CNN was trained on the DS1 image dataset (see above), which contains images of various modalities including CT, ultrasound, PET, and MRI. Examples are presented in Fig. 2.

CNN architecture is shown in Fig. 3 and consists of the following layers: Conv3D, MaxPool3D, Dropout, GlobalAveragePooling3D.

Neural network parameters were selected in practice during numerous training sessions. The study showed that the input layer with resolution 64×64×64 and convolutional layer with 25 output filters turned out to be acceptable for the modality check method. Training data were normalized and rotated by 90, 180, and 270 degrees, which eliminates inaccuracies associated with image rotation.

2.3 Method of Checking of Lungs Presence

To determine if a CT scan contains images of a person's lungs and not another part of the body, we used CNN to classify lungs and non-lungs, i.e. a binary classification task was implemented. The CNN was trained on the DS2 image dataset, which included chest CT scans with lungs and other body parts (non-lungs).

Obvious CT scans of non-lungs type are masks, head, abdomen, limbs, scout preliminary scans, empty scans, etc. However, the difference between lungs and non-lungs is not as obvious as it seems. We agreed that the following categories are "non-lungs" class:

– biopsy scans of lungs;
– double, triple and multiple lungs in one image;
– whole body scans including lungs, abdomen, head, limbs, etc.;

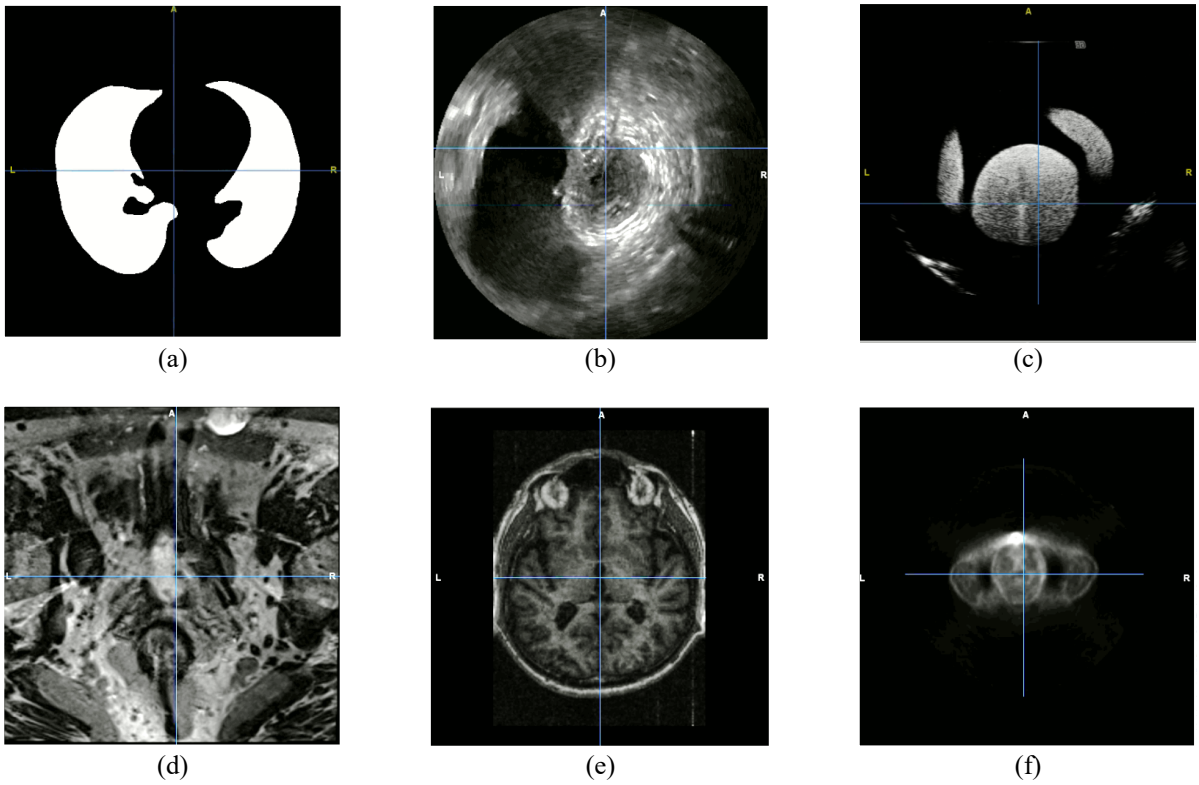


Fig. 2 Examples of 2D layers of 3D images of the "non-CT" class in the dataset DS1 for CT images modality check: (a) binary mask of lungs (512×512 pixels); (b) ultrasound images of prostate (452×452 pixels); (c) ultrasound images of baby phantom (532×416 pixels); (d) MRI images of prostate (256×256 pixels); (e) MRI images of brain (256×256 pixels); (f) PET image of body (128×128 pixels).

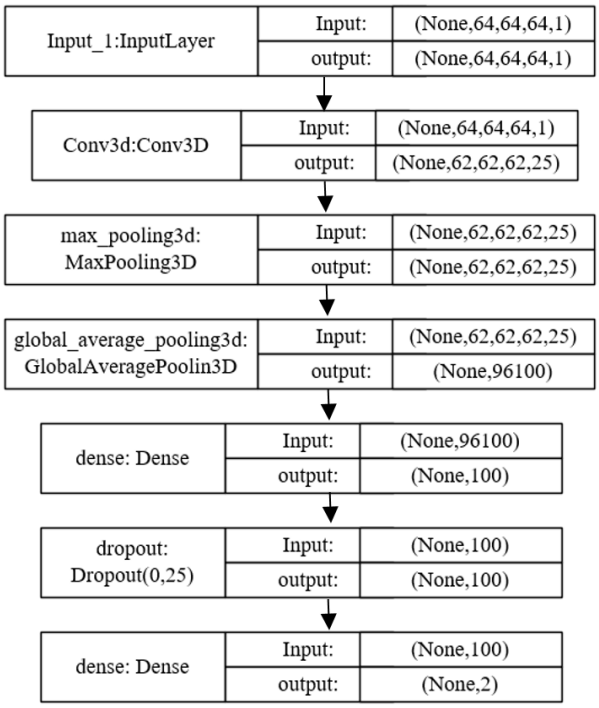
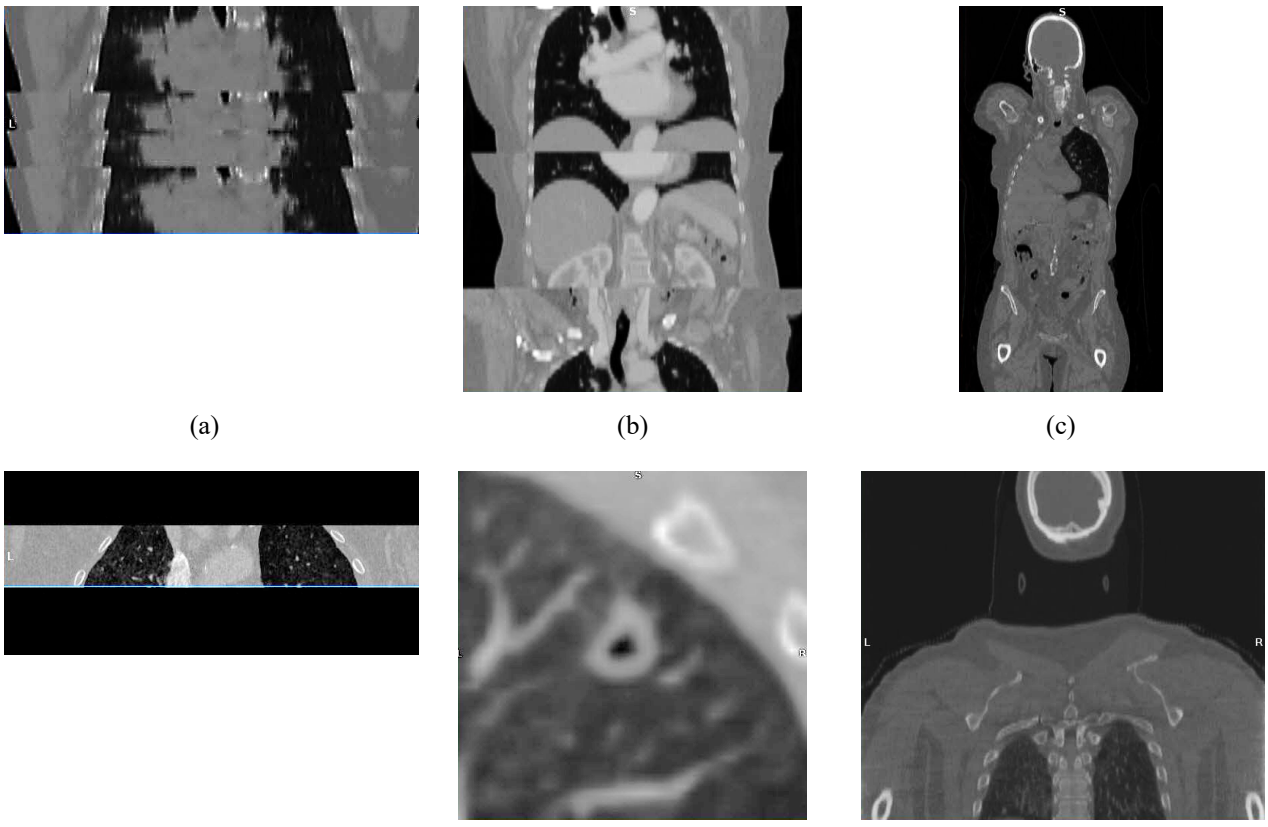


Fig. 3 Convolutional neural network architecture for CT images modality check.



(a) (b) (c)

(d) (e) (f)

Fig. 4 Examples of 2D layers of 3D images of the non-obvious cases of "non-lungs" class in the DS2 dataset for checking of lungs presence: (a) biopsy scan of lungs (512×43 pixels); (b) triple lungs in one image (512×87 pixels); (c) whole body scan including lungs, abdomen, head, limbs, etc. (512×287 pixels); (d) pancake-like (significantly cropped) scan of lungs (512×51 pixels); (e) 3D box-shaped region containing lung nodules (50×50 pixels); (f) lungs occupy less than 50% of the coronal axis (512×135 pixels).

– pancake-like (significantly cropped) scans of lungs;

– 3D box-shaped regions containing lung nodules;

– if the lungs occupy less than 50 % of the coronal axis.

– Examples of non-obvious types are shown in Fig. 4.

Binary classification of lungs from non-lungs is a relatively simple task, so a simple 4-block CNN was used (Fig. 5).

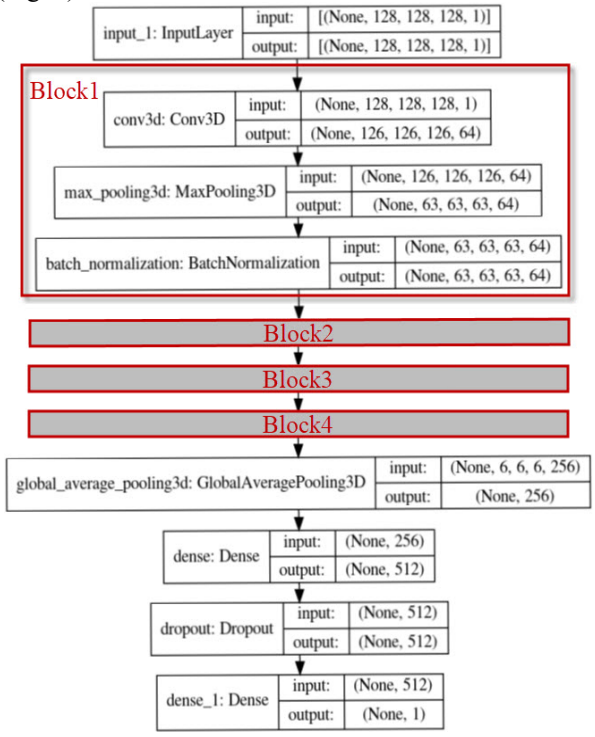


Fig. 5 Convolutional neural network architecture for checking of lungs presence.

Each block of the 4-block neural network consists of the same three layers: Conv3D, MaxPool3D, and BatchNormalization. After four blocks, the GlobalAveragePooling3D layer is added. Convolution layers and the penultimate dense layer have ReLU activation and the final dense layer has Sigmoid activation to perform binary classification.

Files are provided in NifTI format with the ".nii.gz" extension. To read the scans, we use the "nibabel" package. CT scans store raw voxel intensities in Hounsfield units (HU), which vary widely and may differ from dataset to dataset. Above 500 HU are bones with different radio intensity, so this is used as a higher bound. Air and subtle tissues usually associated with [–1500, 0] HU range. A threshold between –1500 and 500 is commonly used to normalize CT scans. To preprocess the data, we do the following [27]:

1. Apply threshold [–1500, 500] HU;
2. Scale the HU values down to the [–1, 1] range;
3. Resize width, height and depth to 128×128×128, the volume has to be cubic for the further augmentation;
4. Rotate the volumes by 90 degrees, so the orientation is fixed.

The last step with rotation by 90 degrees is not necessary, because of subsequent augmentation with random rotations. To increase preprocessing speed, we used a "multiprocessing" Python module so that all or part of the CPU cores can be used in a parallel mode.

Augmentation is used both for the training and validation sets. The reason to use augmentation for the validation set is that we have many augmented CT images in our testing set. Also note that a random transposition followed by a flip is equivalent to random rotation. Augmentation function:

1. Permutes randomly (transposes) three axes of a 3D CT image;
2. Flips randomly a volume out of eight different choices, including identity flip (or None), which does nothing (flips = [None, 0, 1, 2, (0,1), (0,2), (1,2), (0,1,2)]);
3. Finally makes sure that the volume stays between the [–1, 1] range.

Neural network architecture, augmentation and hyperparameters were modified several times. After each modification and training of the model it was used to the datasets mentioned above to find wrong predictions between lungs and non-lungs (false-positive and false-negative predictions). All images found with incorrect predictions were visually reviewed and added to our dataset.

3 Results and Discussions

3.1 CT Image Modality Check

The trained model for method of modality check achieved 100% classification accuracy on the test dataset, which was not involved in model training. All of the images were attributed to the desired class. Model accuracy and loss for train and validation sets are shown in Fig. 6.

Results of binary classification of CT from non-CT images are shown in Table 1.

Table 1 Results of binary classification of CT from non-CT images.

Dataset	Accuracy, %	Number of images	Number of wrong predictions
train	100	214	0
validation	100	12	0
test	100	280	0

The model was trained five times and each time it showed one hundred percent result on a test dataset. The train and validation datasets changed when learning every time. Therefore, the results of the model predictions do not depend on the data composition in the training set.

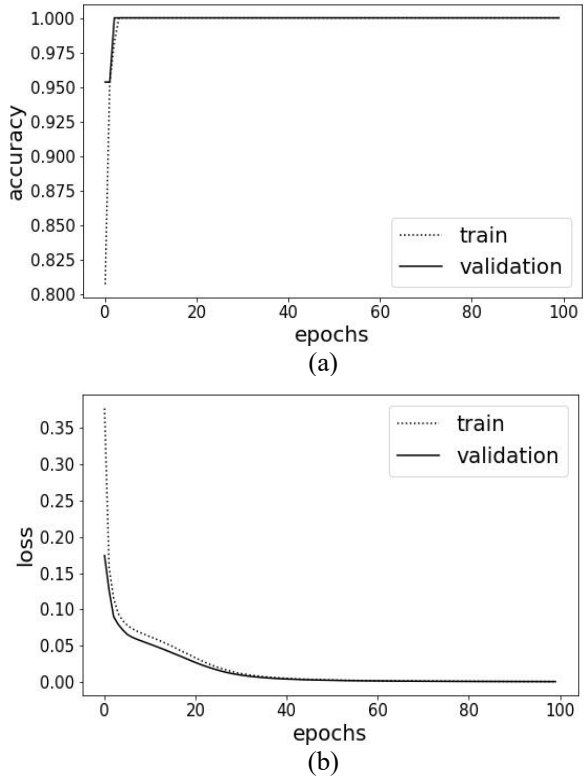


Fig. 6 Training diagram for model accuracy (a) and loss (b) for classification of CT from non-CT images in 100 epochs for dataset DS1.

Regarding 100% accuracy in modality verification, we did a similar study to verify the modality of X-ray images (similar to CT), and we are preparing a new article on this topic. During the experiments, it turned out that the same method showed less than 70% accuracy for X-ray images. So, we had to significantly increase the training samples up to 1000 images for each class and use more advanced architecture of EfficientNet CNN to achieve 99.8% accuracy. For this reason, we believe that CT images have significant differences from MRI, ultrasound, binary masks, histological images, etc.

Finally, based on our results we can conclude that the method can be used for CT images modality check. Despite the fact that the model showed a good result on the CT images, this approach needs to be explored to solve problems of determining other modalities. This is necessary for the development of medical (non-CT) imaging services.

3.2 Checking of Lungs Presence

Results for binary classification of lungs from non-lungs are not so unambiguous. Model training used a large patience for callback "keras.callbacks.EarlyStopping" equal to 50 epochs and stopped training automatically after 147 epochs. Model accuracy and loss for train and validation sets are shown in Fig. 7.

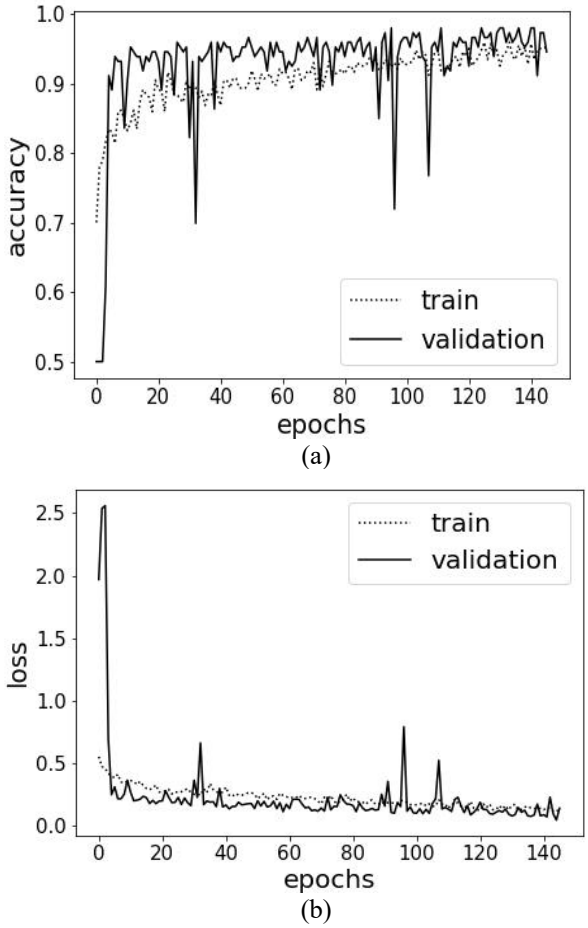


Fig. 7 Training diagram for model accuracy (a) and loss (b) for classification of lungs from non-lungs in 147 epochs for dataset DS2.

Results of checking of lungs presence are shown in Table 2.

Table 2 Results for classification of lungs from non-lungs.

Dataset	Accuracy, %	Number of images	Number of wrong predictions
train	98.64	440	6
validation	98.63	146	2
test	89.02	82	9

From the total 17 wrong predictions only one CT scan is from the STOIC2021 dataset. Other 16 CT images are from the ACRIN-NSCLC-FDG-PET (ACRIN 6668) dataset [12]: eleven are artificially created; three are biopsy scans; one real CT scan with chest and part of the head; one real pancake-like (significantly cropped) scan of lungs.



(a) (b) (c)

Fig. 8 Examples of biopsy CT images, coronal view (2D layer image sizes are 512×69 (a), 512×65 (b), and 512×43 pixels.

Eleven artificially created scans with wrong predictions are: four out of total six artificially made biopsy scans; three out of total eight artificially made doubled lungs; two out of total ten artificially made pancake-like (significantly cropped) scans of lungs; and two out of total fifteen artificially made CT scans of lungs with part of the head. A possible reason for the low classification accuracy for artificially created images is their small number, only about a dozen for each non-standard case in DS2. Perhaps we need to add more artificial images to improve the classification accuracy.

Analysis of wrong predictions showed that the model performs poorly on biopsy of lungs. Seven out of total nine (real and artificially created) biopsy CT scans were incorrectly classified as lungs. A possible reason why CT biopsies are incorrectly classified as "lungs" is that their axial view does not differ from normal lungs. However, coronal and sagittal views differ a lot from the lungs class (Fig. 8).

To improve the classification accuracy of biopsy CT scans, we have to add more real and artificial biopsy scans and try more complex standard neural network architectures.

4 Conclusions

The developed validation model shows good results on datasets DS1 and DS2: 100% for CT image modality check and 89.02% for checking of lungs presence. For example, we found nine chest CT scans of lungs which were mistakenly placed in the dataset of head CT scans "CQ500 Dataset" [25]. These scans of lungs were visually checked and added into the "lungs" folder to improve model accuracy. The task of verifying medical data requires further study. We are going to check 2D images for XRay of human lungs. It is necessary to develop a more general method capable of solving the evaluation problem simultaneously at different levels. In general, our trained models performed well and are already being used in our application called "AI-based software for computer-assisted diagnosis of lung diseases using chest X-Ray and CT images" (LungExpert) [1] for screening of incoming data.

Disclosures

The authors declare that they have no conflict of interest.

Acknowledgments

This work was carried out with the financial support of NIAID, NIH, USA, in the framework of the CRDF G-DAA9-20-67103-1 Project.

References

1. A. Rosenthal, A. Gabrielian, E. Engle, et al., "The TB Portals: an Open-Access, Web-Based Platform for Global Drug-Resistant-Tuberculosis Data Sharing and Analysis," Journal of Clinical Microbiology 55(11), 3267–3282 (2017).
2. S. Kaplan, D. Handelman, and A. Handelman, "Sensitivity of neural networks to corruption of image classification," AI Ethics 1, 425–434 (2021).
3. D. Guan, W. Yuan, Y.-K. Lee, and S. Lee, "Identifying mislabeled training data with the aid of unlabeled data," Applied Intelligence 35(3), 345–358 (2011).
4. A. P. Brady, "Error and discrepancy in radiology: inevitable or avoidable?" Insights Imaging 8(1), 171–182 (2017).
5. K. Clark, B. Vendt, K. Smith, J. Freymann, J. Kirby, P. Koppel, S. Moore, S. Phillips, D. Maffitt, M. Pringle, L. Tarbox, and F. Prior, "The Cancer Imaging Archive (TCIA): Maintaining and Operating a Public Information Repository," Journal of Digital Imaging 26(6), 1045–1057 (2013).
6. J. P. Cohen, P. Morrison, and L. Dao, "COVID-19 Image Data Collection," arXiv:2003.11597v1 (2020).

7. J. Yang, G. Sharp, H. Veeraraghavan, W. Van Elmpt, A. Dekker, T. Lustberg, and M. Gooding, "Data from Lung CT Segmentation Challenge," The Cancer Imaging Archive (2017).
8. S. G. Armato, G. McLennan, L. Bidaut, et al., "The Lung Image Database Consortium (LIDC) and Image Database Resource Initiative (IDRI): A Completed Reference Database of Lung Nodules on CT Scans: The LIDC/IDRI thoracic CT database of lung nodules," Medical Physics 38(2), 915–931 (2011).
9. H. Roth, A. Farag, E. B. Turkbey, L. Lu, J. Liu, and R. M. Summers, "Data From Pancreas-CT," The Cancer Imaging Archive (2016).
10. K. Yan, X. Wang, L. Lu, and R. M. Summers, "DeepLesion: automated mining of large-scale lesion annotations and universal lesion detection with deep learning," Journal of Medical Imaging 5(3), 036501 (2018).
11. M. Vallières, E. Kay-Rivest, L. Perrin, X. Liem, C. Furstoss, N. Khaouam, P. Nguyen-Tan, C.-S. Wang, and K. Sultanem, "Data from Head-Neck-PET-CT," The Cancer Imaging Archive (2017).
12. P. Kinahan, M. Muzi, B. Bialecki, B. Herman, and L. Coombs, "Data from the ACRIN 6668 Trial NSCLC-FDG-PET," The Cancer Imaging Archive (2019).
13. M. Patnana, S. Patel, and A. S. Tsao, "Data from Anti-PD-1 Immunotherapy Lung," The Cancer Imaging Archive (2019).
14. J. Eisenbrey, A. Lyshchik, and C. Wessner, "Ultrasound data of a variety of liver masses," The Cancer Imaging Archive (2021).
15. S. Natarajan, A. Priester, D. Margolis, J. Huang, and L. Marks, "Prostate MRI and Ultrasound With Pathology and Coordinates of Tracked Biopsy (Prostate-MRI-US-Biopsy)," The Cancer Imaging Archive (2020).
16. P. J. LaMontagne, T. LS. Benzinger, J. C. Morris, S. Keefe, R. Hornbeck, C. Xiong, E. Grant, J. Hassenstab, K. Moulder, A. G. Vlassenko, M. E. Raichle, C. Cruchaga, and D. Marcus, "OASIS-3: Longitudinal Neuroimaging, Clinical, and Cognitive Dataset for Normal Aging and Alzheimer Disease," medRxiv 2019.12.13.19014902 (2019).
17. D. E. Job, D. A. Dickie, D. Rodriguez, A. Robson, S. Danso, C. Pernet, M. E. Bastin, J. P. Boardman, A. D. Murray, T. Ahearn, G. D. Waiter, R. T. Staff, I. J. Deary, S. D. Shenkin, and J. M. Wardlaw, "A brain imaging repository of normal structural MRI across the life course: Brain Images of Normal Subjects (BRAINS)," NeuroImage 144, 299–304 (2017).
18. D. Newitt, N. Hylton, "Single site breast DCE-MRI data and segmentations from patients undergoing neoadjuvant chemotherapy," The Cancer Imaging Archive (2016).
19. K. Jafari-Khouzani, K. Elisevich, S. Patel, and H. Soltanian-Zadeh, "Dataset of magnetic resonance images of nonepileptic subjects and temporal lobe epilepsy patients for validation of hippocampal segmentation techniques," Neuroinformatics 9, 335–346 (2011).
20. National Cancer Institute Clinical Proteomic Tumor Analysis Consortium (CPTAC), "The Clinical Proteomic Tumor Analysis Consortium Pancreatic Ductal Adenocarcinoma Collection (CPTAC-PDA)," The Cancer Imaging Archive (2018).
21. A. Badano, C. G. Graff, A. Badal, D. Sharma, R. Zeng, F. W. Samuelson, S. Glick, and K. J. Myers, "Data from the VICTRE trial: open-source, in-silico clinical trial for evaluating digital breast tomosynthesis (VICTRE)," The Cancer Imaging Archive (2019).
22. M.-P. Revel, S. Boussouar, C. de Margerie-Mellon, I. Saab, T. Lapotre, D. Mompoint, G. Chassagnon, A. Milon, M. Lederlin, S. Bennani, S. Molière, M.-P. Debray, F. Bompard, S. Dangeard, C. Hani, M. Ohana, S. Bommart, C. Jalaber, M. El Hajjam, I. Petit, L. Fournier, A. Khalil, P.-Y. Brillet, M.-F. Bellin, A. Redheuil, L. Rocher, V. Bousson, P. Rousset, J. Grégory, J.-F. Deux, E. Dion, D. Valeyre, R. Porcher, L. Jilet, and H. Abdoul, "Study of Thoracic CT in COVID-19: The STOIC Project," Radiology 301(1), E361–E370 (2021).
23. S. P. Morozov, A. E. Andreychenko, N. A. Pavlov, A. V. Vladzymyrskyy, N. V. Ledikhova, V. A. Gombolevskiy, I. A. Blokhin, P. B. Gelezhe, A. V. Gonchar, and V. Yu. Chernina, "MosMedData: Chest CT Scans With COVID-19 Related Findings Dataset," arXiv:2005.06465v1 (2020).
24. L. Jin, J. Yang, K. Kuang, B. Ni, Y. Gao, Y. Sun, P. Gao, W. Ma, M. Tan, H. Kang, J. Chen, and M. Li, "Deep-learning-assisted detection and segmentation of rib fractures from CT scans: Development and validation of FracNet," eBioMedicine 62, 103106 (2020).
25. S. Chilamkurthy, R. Ghosh, S. Tanamala, M. Biviji, N. G. Campeau, V. K. Venugopal, V. Mahajan, P. Rao, and P. Warier, "Deep learning algorithms for detection of critical findings in head CT scans: a retrospective study," The Lancet 392(10162), 2388–2396 (2018).
26. E. Sogancioglu, K. Murphy, and B. Van Ginneken, "NODE21," Zenodo (2021).
27. H. Zunair, A. Rahman, N. Mohammed, and J. P. Cohen, "Uniformizing Techniques to Process CT Scans with 3D CNNs for Tuberculosis Prediction," in Predictive Intelligence in Medicine, I. Rekik, E. Adeli, S. H. Park, and M. del C. Valdés Hernández (Eds.), Springer International Publishing 12329, Cham, 156–168 (2020).